Fall 11-22-2010

MicroBioRobots for Single Cell Manipulation

Mahmut Selman Sakar
University of Pennsylvania, sakarmah@seas.upenn.edu

MicroBioRobots for Single Cell Manipulation

Abstract

One of the great challenges in nano and micro scale science and engineering is the independent manipulation of biological cells and small man-made objects with active sensing. For such biomedical applications as single cell manipulation, telemetry, and localized targeted delivery of chemicals, it is important to fabricate microstructures that can be powered and controlled without a tether in fluidic environments. These microstructures can be used to develop microrobots that have the potential to make existing therapeutic and diagnostic procedures less invasive.

Actuation can be realized using various different organic and inorganic methods. Previous studies explored different forms of actuation and control with microorganisms. Bacteria, in particular, offer several advantages as controllable micro actuators: they draw chemical energy directly from their environment, they are genetically modifiable, and they are scalable and configurable in the sense that any number of bacteria can be selectively patterned. Additionally, the study of bacteria inspires inorganic schemes of actuation and control. For these reasons, we chose to employ bacteria while controlling their motility using optical and electrical stimuli.

In the first part of the thesis, we demonstrate a bio-integrated approach by introducing MicroBioRobots (MBRs). MBRs are negative photosensitive epoxy (SU8) microfabricated structures with typical feature sizes ranging from 1-100 μm coated with a monolayer of the swarming Serratia marcescens. The adherent bacterial cells naturally coordinate to propel the microstructures in fluidic environments, which we call Self-Actuation. First, we demonstrate the control of MBRs using self-actuation, DC electric fields and ultra-violet radiation and develop an experimentally-validated mathematical model for the MBRs. This model allows us to to steer the MBR to any position and orientation in a planar micro channel using visual feedback and an inverted microscope. Examples of sub-micron scale transport and assembly as well as computer-based closed-loop control of MBRs are presented. We demonstrate experimentally that vision-based feedback control allows a four-electrode experimental device to steer MBRs along arbitrary paths with micrometer precision. At each time instant, the system identifies the current location of the robot, a control algorithm determines the power supply voltages that will move the charged robot from its current location toward its next desired position, and the necessary electric field is then created. Second, we develop biosensors for the MBRs. Microscopic devices with sensing capabilities could significantly improve single cell analysis, especially in high-resolution detection of patterns of chemicals released from cells in vitro. Two different types of sensing mechanisms are employed. The first method is based on harnessing bacterial power, and in the second method we use genetically engineered bacteria. The small size of the devices gives them access to individual cells, and their large numbers permit simultaneous monitoring of many cells.

In the second part, we describe the construction and operation of truly micron-sized, biocompatible ferromagnetic micro transporters driven by external magnetic fields capable of exerting forces at the pico Newton scale. We develop micro transporters using a simple, single step micro fabrication technique that allows us to produce large numbers in the same step. We also fabricate microgels to deliver drugs. We demonstrate that the micro transporters can be navigated to separate single cells with micron-size precision and localize microgels without disturbing the local environment.

Degree Type
Dissertation

Degree Name
Doctor of Philosophy (PhD)

Graduate Group
Electrical & Systems Engineering

First Advisor
George J Pappas

Second Advisor
Vijay Kumar

Keywords
single cell manipulation, microrobotics, biosensors, biointegrated microsystems

Subject Categories
Biological Engineering | Biomedical | Controls and Control Theory | Nanoscience and Nanotechnology

MICROBIOROBOTS FOR SINGLE CELL MANIPULATION

Mahmut Selman Sakar

A DISSERTATION

in

Electrical and Systems Engineering

Presented to the Faculties of the University of Pennsylvania in Partial

Fulfillment of the Requirements for the Degree of Doctor of Philosophy

2010

George J. Pappas, Supervisor of Dissertation,   Vijay Kumar, Co-Supervisor of Dissertation,

Professor of Electrical and Systems Engineering   Professor of Mechanical Engineering and

Applied Mechanics

Roch Guerin, Graduate Group Chair,

Professor of Electrical and Systems Engineering

Dissertation Committee:

Alejandro Ribeiro, Asisstant Professor of Electrical and Systems Engineering

Min Jun Kim, Assisstant Professor of Mechanical Engineering and Mechanics

Paulo Arratia, Assisstant Professor of Mechanical Engineering and Applied Mechanics

MICROBIOROBOTS FOR SINGLE CELL MANIPULATION

COPYRIGHT

2010

Mahmut Selman Sakar

To my parents

Acknowledgements

First, and foremost, I would like to express my gratitude to my advisor Prof George J Pappas for his confidence in me and giving me the opportunity to conduct my own research in microrobotics, and to my co-advisor Prof Vijay Kumar for his guidance and establishing the collaborations that made the work presented here possible. I feel lucky for having the privilege to observe these two great minds in action. I am also indebted my committee: Professors Alejandro Ribeiro, Paulo Arratia, and Min Jun Kim for their suggestions and encouragement. I specifically thank Professors Min Jun Kim and Paulo Arratia for treating me as if I am one of their group members. In addition, I would like to thank the whole GRASP Laboratory for making Penn such a fruitful experience to me.

During my time at Penn, I have collaborated with many researchers from various different departments, as well as faculty members working in different colleges. Among these people, Dr Edward B Steager was more than a colleague to me. We worked on various different projects together and he always found a way out when we got stuck no matter how hopeless the situation was. I thank him for all his help as well as for his friendship throughout my years in graduate school. I also learned a lot from Prof Agung Julius during my first years of my graduate work while we were working together. From our group members, I would like to thank Prof. David Cappelleri, Dr Spring Berman, Quentin Lindsay, Prof Ani Hsieh and Prof Adam Halasz. Additionally, I would like to thank our collaborators Professors James Eberwine, Junhyong Kim, Harvey Rubin, Stephen Pratt, Shun-ichi Azuma,

ABSTRACT

MICROBIOROBOTS FOR SINGLE CELL MANIPULATION

Mahmut Selman Sakar

Supervisor: George J. Pappas

One of the great challenges in nano and micro scale science and engineering is the independent manipulation of biological cells and small man-made objects with active sensing. For such biomedical applications as single cell manipulation, telemetry, and localized targeted delivery of chemicals, it is important to fabricate microstructures that can be powered and controlled without a tether in fluidic environments. These microstructures can be used to develop microrobots that have the potential to make existing therapeutic and diagnostic procedures less invasive.

Actuation can be realized using various different organic and inorganic methods. Previous studies explored different forms of actuation and control with microorganisms. Bacteria, in particular, offer several advantages as controllable microactuators: they draw chemical energy directly from their environment, they are genetically modifiable, and they are scalable and configurable in the sense that any number of bacteria can be selectively patterned. Additionally, the study of bacteria inspires inorganic schemes of actuation and control. For these reasons, we chose to employ bacteria while controlling their motility using optical and electrical stimuli.

In the first part of the thesis, we demonstrate a biointegrated approach by introducing MicroBioRobots (MBRs). MBRs are negative photosensitive epoxy (SU8) microfabricated structures with typical feature sizes ranging from 1-100 μm coated with a monolayer of the swarming *Serratia marcescens*. The adherent bacterial cells naturally coordinate to propel the microstructures in fluidic environments which we call Self-Actuation. First, we demon-

strate the control of MBRs using self-actuation, DC electric fields and ultra-violet radiation and develop an experimentally-validated mathematical model for the MBRs. This model allows us to to steer the MBR to any position and orientation in a planar micro channel using visual feedback and an inverted microscope. Examples of sub-micron scale transport and assembly as well as computer-based closed-loop control of MBRs are presented. We demonstrate experimentally that vision-based feedback control allows a four-electrode experimental device to steer MBRs along arbitrary paths with micrometer precision. At each time instant, the system identifies the current location of the robot, a control algorithm determines the power supply voltages that will move the charged robot from its current location toward its next desired position, and the necessary electric field is then created. Second, we develop biosensors for the MBRs. Microscopic devices with sensing capabilities could significantly improve single cell analysis, especially in high-resolution detection of patterns of chemicals released from cells in vitro. Two different types of sensing mechanisms are employed. The first method is based on harnessing bacterial power, and in the second method we use genetically engineered bacteria. The small size of the devices gives them access to individual cells, and their large numbers permit simultaneous monitoring of many cells.

In the second part, we describe the construction and operation of truly micron-sized, biocompatible ferromagnetic micro transporters driven by external magnetic fields capable of exerting forces at the pico Newton scale. We develop micro transporters using a simple, single step micro fabrication technique that allows us to produce large numbers in the same step. We also fabricate microgels to deliver drugs. We demonstrate that the micro transporters can be navigated to separate single cells with micron-size precision and localize microgels without disturbing the local environment.

Contents

List of Figures

Chapter 1

Introduction

The field of microrobotics can be defined as the design and fabrication of robotic agents in the micrometer range and the robotic manipulation of objects with characteristic dimensions in a similar size range [2]. Applications of micromanipulation include manipulation of biological cells and assembly of micro-sized parts. The dominant forces at these length scales are considerably different than those in typical macroscale systems. As length scale (L) decreases, surface forces (L^2) begin to dominate body forces (L^3). Gravitational and inertial forces become less influential, and adhesive interactions as well as viscous fluid forces become more significant [3]. In addition, traditional fabrication methods become unfeasible and novel technologies must be considered in the design of microrobots.

The fundamental challenge with decreasing robot size is providing wireless actuation and power to the robot. Microrobots can receive both power and instructions through a patterned surface with a scratch drive actuation technique [4]. However, microrobots that do not rely on specialized surfaces for power delivery and control are needed to perform complicated tasks like single cell manipulation. It is well understood that non-reciprocal movements are necessary for propulsion in low Reynolds number fluidic environments [3], and bio-inspired devices based on the helical shape of the bacterial flagellum or the shape-

varying stroke of the cilium have garnered considerable attention [5–9]. Such biomimetic microactuators can be manufactured using inorganic materials. Inspired by the flagella of bacteria, helical microrobots have been demonstrated to swim in low Reynolds number regimes by using rotating magnetic fields. In one line of work, artificial bacteria with a helical semiconductor tail and soft magnetic head are controlled using magnetic fields [6]. In a related work, artificial bacteria are fabricated from silicon dioxide using a glancing angle deposition technique [7]. In this technique, silicon dioxide is vapor deposited on an array of beads using a shadow growth method. However, the ability to fabricate the required geometries is practically limited by the planar nature of microfabrication processes. Hybrid organic/inorganic schemes can also be realized. Magnetic particles linked by DNA are attached to a red blood cell, and created a propulsive, beating motion [5].

The use of magnetic fields provides an attractive source of energy for untethered wirelessly controlled microrobotic agents. Systems have been proposed that rely on field gradients to propel the robots [10]. Gradient propulsion requires relatively large magnetic fields as magnetic force scales with both distance and agent volume. These restrictions place strong limits on the minimum size of the robots [11]. Torques induced on ferromagnetic materials in a magnetic field scale more favorably than the gradient force, which has led to a number of different approaches for microrobotic locomotion. Miniature robotic systems with wireless magnetic end effectors have been proposed for biomanipulation [12]. In a similar approach, hard magnetic materials such as NdFeB have been employed to induce a stick slip motion on different substrates [13]. Another class of actuators utilizes magnetic energy from the environment and transforms it to impact-driven mechanical force. This concept is called wireless resonant magnetic micro-actuation (WRMMa) for untethered mobile microrobots and it has been introduced in [14] while their application and driving performance were demonstrated by [15]. In another line of work, untethered thermobio-chemically actuated microgrippers are employed as microscale tools to grasp, transport and

2

release clusters of fibroblast cells [36].

Using biomolecular motors is another option [16,17]. The integration of parallel motor assemblies, such as muscle bundles, with MEMS technologies is very attractive because the developed system can be highly scalable. Besides, these devices have onboard actuators that can be powered by glucose present in physiological liquids. Neonatal rat ventricular cardiomyocytes [18,19] and insect dorsal vessel tissue [20] are assembled on microfabricated structures to develop muscle-powered controllable autonomous microdevices.

As an alternative solution, previous studies explored different forms of actuation and control with microorganisms. Several groups reported attempts to integrate living organisms into micromechanical devices and presented methods for harnessing the power produced by biological motors in efforts to realize microrobots or autonomous microdevices [21–24]. Such cyborg microrobots could use chemical gradients, light or other stimuli to passively or actively control the motion of the cell component. The earliest demonstration of control of microorganisms for microrobotics involved the galvanotactic (electrode-seeking) control of the protozoan *Paramecium* [25]. Similar work has recently demonstrated steering *Tetrahymena pyriformis* cells using galvanotaxis while using phototaxis for temporary cell trapping [26].

Bacteria, in particular, offer several advantages as controllable microactuators: they draw chemical energy directly from their environment, they are genetically modifiable, and they are scalable and configurable in the sense that the cells can be selectively patterned. Bacteria are a key component of several biointegrated hybrid organic/inorganic MEMS devices, including a host of actuators and sensors. In one of the first instances of biointegrated, mechanical actuators, microscale rotors were driven using the gliding bacteria *Mycoplasma mobile*, which were directionally attached to the rotor teeth [21]. Lab-on-a-chip fluid pumping and mixing was also demonstrated with *Serratia marcescens* and E. coli, respectively [27]. The chaotic interactions of swimming bacteria with microscale

3

gears have also been shown to produce useful work given the proper choice of device geometry [28,29]. Other work that shows considerable promise has focused on using bacteria for optical or chemical read-out techniques to develop hybrid sensors.

Much of the current work on harnessing the mechanical energy of bacteria has been directed by researchers with interest in robotics. As such, there has been a focus on the ability to control groups of cells with the goal of directing and harnessing their energy to accomplish tasks such as manipulation and assembly. Magnetotactic bacteria may be controlled to swim *en masse* in the direction of magnetic field lines, and have been used as collectives to move microscale structures [30]. On/off microbead propulsion in response to chemical stimulus has been demonstrated using the bacterium *Serratia marcescens* [31], but controlled actuation in response to chemical gradients is inherently limited by the development of the chemical concentrations, as governed by the diffusion equation. On/off control of microstructure movement powered by swarming *S. marcescens* has also been investigated using short-term exposure to ultraviolet light [32].

1.1   Problem Statement

Autonomous smart microdevices with sensing and information processing capabilities have great potential use in drug delivery and single cell analysis [33]. For the specific application of automatic, remotely controlled manipulation of cells or microobjects, control of both rotation and translation is desired. Rotational control is of particular interest where the device has a nonsymmetrical geometry designed for engagement and trapping. Since many potential applications for micromanipulation are performed on a glass slide in a single focal plane using standard light microscopy, the manipulation techniques presented in this work are restricted to two-dimensional planar motion. There is still no microrobot that has a characteristic length in the order of the size of a mammalian cell and has the capability

of sensing biologically relevant chemicals. The ability to monitor the behavior of these microrobots in response to biologically relevant chemicals is an important requirement for further development.

As the length scales of robotic systems continue to decrease, one of the clear emerging applications is the manipulation of single biological cells in fluid environments. Single-cell manipulation has traditionally been achieved with pipettes, optical tweezers, or specialized microfluidic channel designs [34]. Magnetic control of microrobots and microgrippers has also been established as an effective means of microobject manipulation [15, 35–37]. However, significant challenges remain for applications relating to single cell manipulation mainly due to appropriate scaling of robot size and geometry of existing designs.

To define the appropriate design constraints for robotic single cell manipulation, it is assumed that the most appropriate workspace is on the stage of existing inverted or upright light microscopes. Such microscopes are ubiquitous in life science research laboratories, and include essential capabilities such as phase contrast and fluorescence microscopy. Therefore, the integration of the full design necessarily includes not only an appropriate robot design, but also a compact controller that is compatible with the stage of existing microscopes. By integrating the design into existing microscopes, imaging capture capabilities of the microscopes may also be harnessed.

One of the most important length scales to consider for the system is the workspace for the robot. When working with single cells, fine details of individual cells must be resolved. It is essential to have microstructures with sizes in the same order of target cells in order to transport and position them with some precision. The mammalian cell is an entity with typical dimensions of tens of microns. This requires a magnification of at least 40X. The workspace is then 150 μm $\times$ 150 μm. Based on this, it becomes clear that the robot must not only be small relative to the workspace, but also that precise control of movement is much more important than high speed. In fact, rapid movements may cause significant

unwanted disturbances to the microenvironment.

Biocompatibility is another essential consideration for the design of a microrobotic cell manipulator. For experiments with living cells, the idea of biocompatibility must be extended from the basic concept of not causing injury to cells to not influencing the behavior of cells due to the chemical composition of the robot. Furthermore, the biocompatibility of the overall design should include any chemicals released in the process of introducing the robot to the cellular microenvironment.

Robotic manipulators on the scale of cells themselves offers significant potential benefits beyond simply moving cells. Wirelessly controlled (*i.e.* untethered) cell-sized robots are highly noninvasive. At this length scale, where viscous fluid forces dominate inertial forces, motile microrobots cause very little mixing or agitation of the surrounding environment. This is a significant advantage over suction pipetting for life scientists, since pipettes cause relatively large fluid disturbances. Traditionally, the focus of robotic manipulators has been centered on applying mechanical forces. However, on the scale of individual cells, the understanding of the word manipulation itself must be expanded to include chemical manipulation of local microenvironments. To a great extent, research in single cell life sciences is concerned with biochemistry. Due to this, a system for the delivery of chemicals in the microenvironment would also greatly enhance the potential of a microrobotic system.

1.2 Approach

In the first part of this thesis (Chapters 3,4 and 5), we investigate a hybrid solution for the controlled manipulation of microscale components with a biointegrated approach. Bacteria attached to the surface of microfabricated parts, referred to as microbiorobots (MBRs), naturally impart a predominantly rotational motion, largely due to the distribution of bacterial cell body orientations and hence, flagellar thrusts. Here we show that the rate of rota-

tion can be adjusted using optical stimuli. By harnessing both the collective work and the electrostatic potential of bacteria, MBRs are actuated and their motion is controlled using a combination of external stimuli. These robots are steered in a fully-automated fashion using computer control, used to transport and manipulate micron-size objects. To take advantage of integrated live cells, they can be genetically modified and employed as sensing elements. We describe the development of self-sustained mobile biohybrid microdevices that harness bacterial cells for biosensors. We demonstrate two different approaches for biosensing: motility-based sensing and fluorescent-based sensing.

In the second part of the thesis (Chapter 6), we develop a microrobotic manipulation system using electromagnetic actuation supported with visual feedback to meet these challenges. The robot, which is only slightly larger than the rat hippocampal neurons which we are interested in manipulating, has been designed to work on a scale appropriate for the working space of a standard optical microscope. It is aligned by magnetic fields and pulled by field gradients. An oscillating out-of-plane magnetic field induces a stick/slip mechanism that enhances control of the robot [38]. This is useful not only for adjusting the velocity of the robot [35], but also for traversing irregular microscale topographies such as surfaces densely patterned with adherent cells. Composed of iron oxide nanoparticles embedded in a polymer, the robot is fully biocompatible and is patterned using a single-mask photolithographic process. The robot is similar in density to the working fluid. Thus, very small magnetic forces are required for movement. Furthermore, due to the sub-micron resolution of the photolithographic micromachining process, the robot's shape can be tailored to and scaled appropriately for geometric compatibility with different cell types. Release in the microenvironment is enabled by a biocompatible, water-soluble etch process.

A five-coiled magnetic controller was designed for rapid integration with existing microscopes. This is essential due to the fact that many features of single cells are nearly indistinguishable without the aid of phase contrast or fluorescence microscopy. Visual ser-

voing was incorporated for either teleoperation or fully automated manipulation, and was demonstrated using latex microbeads, *Tetrahymena* cells and rat hippocampal neurons.

Finally, we present results on the integration of microscale hydrogels designed for the localized delivery of chemicals using the microrobot. Hydrogels have been established as an effective means of encapsulating and delivering drugs, and their design may be specifically tailored for customized time-based release [39] or even release in response to environmental triggers such as pH and temperature [40]. The gels are capable of creating localized complex gradients and transporting drugs or chemicals to specific positions of target cells.

1.3   Organization of this work

To understand microrobotics, we must begin with a discussion of how physical effects manifest at the microscale. In the first part of the thesis, fabrication, mathematical modeling, control and experimental characterization of MBRs is described. In Chapter 3, a stochastic mathematical model for the system is constructed, based on the assumption that the behavior of each bacterium is random and independent of that of its neighbors. In addition to developing the stochastic model, parameters of the model are identified, based on experimental data. Then it is shown that that the model with the estimated parameters is able to predict the behavior of the system very well. In Chapter 4, two-dimensional control of MBRs is demonstrated using DC electric fields. A novel electrotaxis chamber is designed and fabricated to harness the electrical potential of the cells. Further, the system is rigorously analyzed and a comprehensive understanding of the fundamental physics and a complete model are developed. In Chapter 5, the control techniques are applied to orient and steer bacterial microbiorobots as well as to transport target loads. We also integrate genetically engineered bacterial cells with our robots and show the feasibility of developing the technology base for producing hybrid biosensors. In Chapter 6, the construction

8

and operation of truly micron-sized, biocompatible ferromagnetic microtransporters driven by external magnetic fields is described. We also describe the fabrication of microgels to deliver drugs. We demonstrate that the microtransporters can be navigated to separate single cells with micron-size precision and localize microgels without disturbing the local environment.

Chapter 2

Background

2.1 Life at Low Reynolds Number

The physics governing swimming at the micron scale is fundamentally different from the physics of swimming at the macroscopic scale. The world of microrobots is the world of low Reynolds number, a world where inertial forces are small compared to viscous drag forces. The response of the fluid to the motion of boundaries is instantaneous and the rate at which the momentum of a low Reynolds number swimmer changes is negligible when compared with the typical magnitude of the forces from the surrounding viscous fluid. As a result, Newtons law becomes a simple statement of instantaneous balance between external and fluid forces and moments.

The Reynolds number Re is defined as $Re = \rho U L/\eta$, where ρ is the fluid density, η is the viscosity and U and L are characteristic velocity and length scales of the flow, respectively. In water ($\rho \approx 10^3$ kg m^{-3}, $\eta \approx 10^{-3}$ Pa s), a swimming bacterium such as *E. coli* with $U \approx 10$ μm s^{-1} and $L \approx 1 - 10$ μm has a Reynolds number $Re \approx 10^{-5} - 10^{-4}$.

At these low Reynolds numbers, it is appropriate to study the limit $Re = 0$, for which the Navier-Stokes equations simplify to the Stokes equations

$$-\nabla p + \eta \nabla^2 u = 0, \ \nabla \cdot u = 0. \tag{2.1}$$

where u is the velocity of the swimmer, p is the pressure and η is the viscosity of the fluid.

The Stokes equation (2.1) is linear and independent of time. When applied to low Reynolds number locomotion, the linearity and time-independence of Stokes equation of motion lead to two important properties. The first is rate independence: if a body undergoes surface deformation, the distance travelled by the swimmer between two different surface configurations does not depend on the rate at which the surface deformation occurs but only on its geometry. The second important property of swimming without inertia is the so-called scallop theorem: if the sequence of shapes displayed by a swimmer deforming in a time periodic fashion is identical when viewed after a time-reversal transformation, then the swimmer cannot move on average. As a result, locomotion results from non-reciprocal deformations in order to break time-reversal symmetry [3].

2.2 The hydrodynamics of swimming microorganisms

Swimming strategies employed by larger organisms that operate at high Reynolds number, such as fish, birds or insects, are ineffective at the small scale. For example, any attempt to move by imparting momentum to the fluid, as is done in paddling, will be foiled by the large viscous damping. Therefore microorganisms have evolved propulsion strategies that successfully overcome and exploit drag [41].

Examples of low *Re* swimmers include bacteria, sperm cells, and various kinds of proto-zoa. Flagellated bacteria, such as *Escherichia coli*, swim by rotating thin helical filaments, each driven at its base by a rotary motor. The filament has a diameter of ≈ 20 nm and traces out a helix with contour length ≈ 10 μm. In the absence of external forces and moments,

the helix is left-handed with a pitch $\approx 2.5\ \mu$m and a helical diameter $\approx 0.5\ \mu$m [42]. There are usually several flagella per cell. When the motor turns counter-clockwise (when viewed from outside the cell body), the filaments wrap into a bundle that pushes the cell along at speeds of 25-35 μm s^{-1} [43]. When one or more of the motors reverse, the corresponding filaments leave the bundle and undergo polymorphic transformations in which the handedness of the helix changes; these polymorphic transformations can change the swimming direction of the cell.

2.2.1 Flagellar Dynamics in Viscous Fluids

Direct visualization of the flow patterns around individual flagellar filaments is quite challenging due to the filament small length scale ($\approx$ 20 nm) and its high rotation rates ($\approx$ 100 Hz).

In our previous work, we investigated the flow behavior of a helical impeller rotating in a viscous fluid at low Reynolds number, defined as $Re = \rho \Omega \lambda^2 / \mu$, using a macroscopic-scale model system [44,45]. Here, Ω is the angular velocity, λ is the helical pitch, and ρ and μ are the fluid density and viscosity, respectively. Experiments were performed in a transparent flat-bottom cylindrical vessel placed in a large cubic chamber made of acrylic to correct for optical distortion. Both chamber and tank were filled with the same working fluid in order to match the refraction index. The working fluid was pure glycerol ($\rho = 1.2$ g/cm^3, $\mu = 800$ cP). The tank height and diameter were 36 cm and 24 cm, respectively. A rigid helical filament, which was attached to an electric motor, was immersed in the fluid. The motor typically rotated at 1.2 Hz and the helical pitch is 6 cm. Under such conditions, $Re \approx 0.8$. The flow was visualized using ultra-violet(UV) fluorescence. The flow behavior was assessed by the location of a neutrally buoyant dye as a function of time using a digital camera (see Figure 2.1). The geometry of the cylindrical tank seems to be the main factor determined the symmetrical bowl shape of the envelope. Over time these envelopes become
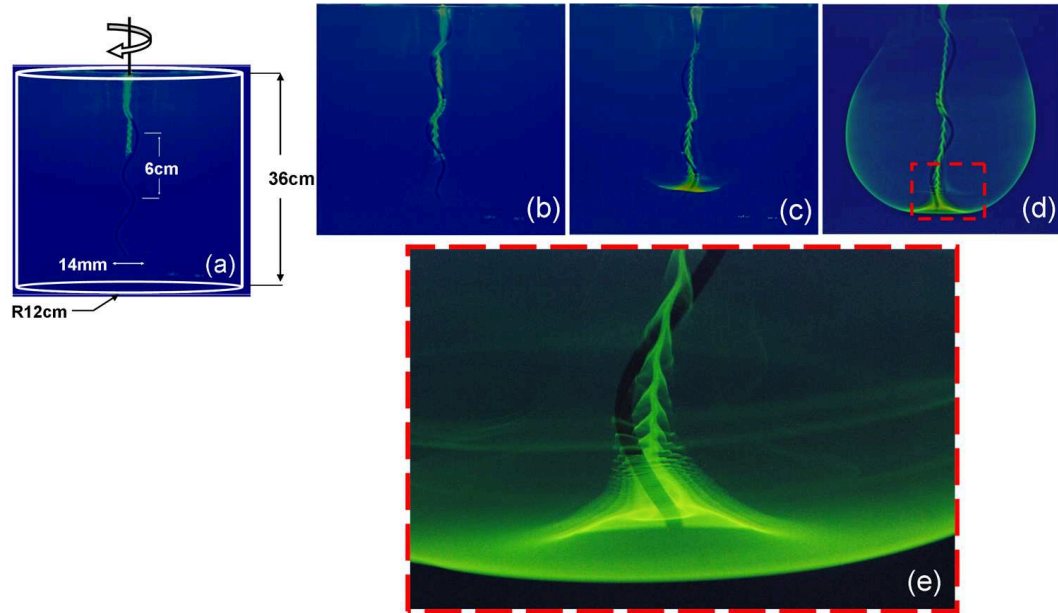
Figure 2.1: (a) - (b) The gradual movement of the dye downwards while wrapping around the filament and producing a fishscale-like pattern until it reaches an unstable point at the tip of the helix. This instability forms due to the helical shape of the flagellum and continues to be generated at the tip of the helix as shown in (c). (d) Fully developed flow pattern. The flow in the far field falls of inversely with distance. (e) A close-up of the tip of the flagellum revealing complex flow patterns.

cyclic.

Eukaryotic flagella and cilia are much larger than bacterial flagella, with a typical diameter of ≈ 200 nm. There is a vast diversity in the beat pattern and length of eukaryotic flagella. The cilia and flagella of sperm cells and protozoa are autonomously active structures that propagate bending waves from their base to the tip. The sperm of many organisms consists of a head containing the genetic material together with enzymes that enable fertilization to occur propelled by a filament with a planar sinusoidal or helical beat pattern, depending on the species. The length of the flagellum is ≈ 40 μm for humans. In ciliate protozoa, hundreds of cilia can coordinate and self-organize to produce a collective thrust. *Paramecium* is one classic example of a ciliated microorganism. Its surface is covered by thousands of cilia that beat in a coordinated manner [46], propelling the cell at speeds of

13

$\approx 500~\mu\text{m s}^{-1}$. Tetrahymena pyriformis (T. pyriformis) also swim using cilia and there are approximately 600 cilia, both oral and locomotive, covering the cell body. Cilia closely resemble the eukaryotic flagella in internal structure and mode of action. They are also active organelles but their waveform is more complex consisting of a power stroke and a recovery stroke. The cell rotates as swims due to a slight time lag between the beating of successive rows of cilia and moves through water with a net rate of up to several millimeters per second. *Chlamydomonas reinhardtii* is an alga with two flagella that can exhibit both ciliary and flagellar beat patterns. A cell swimming in the dark stochastically switches between synchronous and asynchronous flagellar beating. These regimes lead to nearly straight swimming and to abrupt large reorientations, which yield a eukaryotic version of the "run-and-tumble" motion of peritrichously flagellated bacteria [47].

Many cell types travel from one location to another throughout their life. The direction of this movement is intricately linked to their local environment. This directed movement, or taxis, may be an active signaling response such as chemotaxis, whereby the cells sense and process the composition of their chemical environment. When a cell moves toward higher concentrations of attractant or lower concentrations of repellent, clockwise flagellar rotation and, hence, tumbling are suppressed. The random walk is thereby biased so that the cell migrates up an attractant gradient or down a repellent gradient. Gradients are sensed as temporal changes in concentration by comparing the instantaneous concentration with the concentration the cell experienced a few seconds earlier [48].

The taxis may also be passive, where the stimuli impose a change on the motion. As an example of such passive movement, the motion of magnetotactic bacteria such as MC-1 is heavily influenced by weak magnetic fields. The cell bodies align with external magnetic fields as they carry chains of iron-rich magnetosomes [49]. This kind of directed movement is a form of adaptation enabling these cells to move to oxygen-rich environments. There a rich repertoire of conditions that causes tactic behavior. For instance, different species

of bacteria have been shown to have several mechanisms to move toward or away from light. Multiple mechanisms for this movement have been discovered, and sensitivities to various wavelengths have been reported. The unicellular algae *Chlamydomonas reinhardtii* is phototactic and can be guided using visible light. Cells have been controlled by switching light emitting diodes on or off at either end of a microfluidic channel. This mechanism has been exploited to direct and transport microscale loads [23].

2.3   Controlling Biological Systems

Biological systems exhibit many features of complex engineering systems. The origin of system complexity is generally the presence of multiple regulatory mechanisms such as feedback. Among several possible control strategies, feedback seems to be favored in biological systems [50]. Hierarchies of feedback loops result in system robustness, performance, and noise rejection, which are the properties of almost every biological system. Another key feature of biological systems is emergence, aggregate behaviors that may not be predicted by only investigating the individual components or subsystems. The existence of emergent properties can also be explained by the presence of control mechanisms [51].

2.3.1   Stochasticity and Single Cell Studies

Cellular function often involves small numbers of molecules like DNA. These molecules give organisms their unique genetic identity. Even genetically identical organisms grown in homogenous environments can be very different. One of the main sources of this variability is noise in gene expression - the random fluctuations in the expression of individual genes. This is because the expression of a gene involves discrete and random biochemical reactions involved in the production of mRNAs and proteins. The lox copy numbers further exacerbate the noisiness of the system. In the past few years, it has been recognized that

stochastic phenomena may have a crucial role in the fate of individual cells [52]. Stochastic gene expression has important consequences for cellular function, being beneficial in some contexts by producing adaptive phenotypes and harmful in others. As an example, studies have found that the decisions by *E. coli* to enter a quiescent state to survive antibiotic exposure (persistence) are stochastically controlled [53]. The most prominent adaptive explanation for this strategy is bet-hedging. In microorganisms, a population might enhance its fitness in fluctuating environments by allowing individual cells to stochastically transition among multiple phenotypes, thus ensuring that some cells are always prepared [54]. Without the need to sense the environment, cells could blindly anticipate and survive environmental changes with this strategy assuming that each phenotype fit to a particular environment. Persistence has a direct benefit to the population as it allows survival during catastrophes. Furthermore, persistent cells can provide an indirect benefit to other individuals, as the reduced growth rate can reduce competition for limiting resources.

Cells in the population can exist in a continuum of phetoypes too, as occurs in swimming in *E. coli*. In complex habitats with a sparse distribution of nutrients, variability among individual cells in the time periods between motility switches can be expected to form the basis of an ideal search strategy. In addition, variable responsiveness to chemoattractants could help individual bacterial cells avoid predators, where attractant release is a mechanism for luring bacterial prey [55].

2.3.2 Performing Collective Tasks with Cells and Microorganisms

There is a recent interest in the scientific community to integrate microorganisms and living cells with engineered systems to develop microrobots, novel biosensors and intelligent microdevices. The overall system can be compact, fast and inexpensive. Furthermore, the cellular propulsion or actuation component could be multifunctional, perhaps serving as a biochemical sensor or navigation controller [56]. Such systems are, however, limited by the
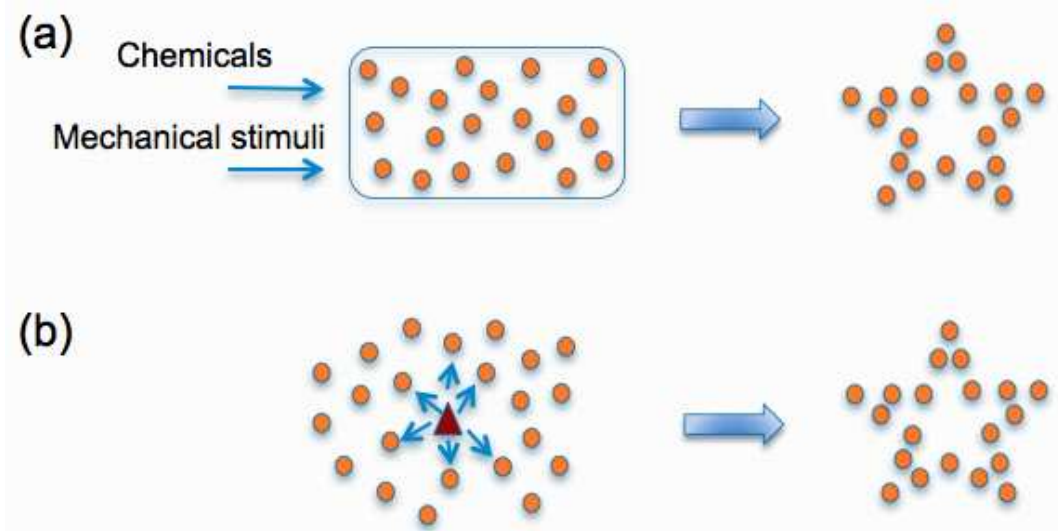
Figure 2.2: Controlling collective behavior of cells. (a) Using a global signal and/or physical limitations. (b) Using an agent and local communication through chemical and mechanical signals

often stochastic nature of cellular motion as described in the previous section. As a result, novel strategies have to be employed to harness and control ensembles of cells. There are two different methods control methodologies as shown in Figure 2.2. In the first approach, the collective behavior of cells are controlled by applying a global signal: a mechanical and/or chemical signal that affects all the cells in the environment.

In our previous work, we explored such a scenario which involves pure chemical control [57]. The architecture of the control system is illustrated in Figure 2.3. The plant to be controlled is a large colony of *E. coli* bacteria. We constructed an abstraction of the stochastic model that is simple enough to allow for fast computation. This is particularly desirable, for example, when we want to simulate the behavior of a colony of bacteria. Without the abstraction, we would have to run multiple copies of the stochastic simulation, which can be computationally prohibitive.

The controller affects the plant by adjusting the external concentration of thio-methyl galactosidase (TMG) in the environment. Feedback information is read from the plant in
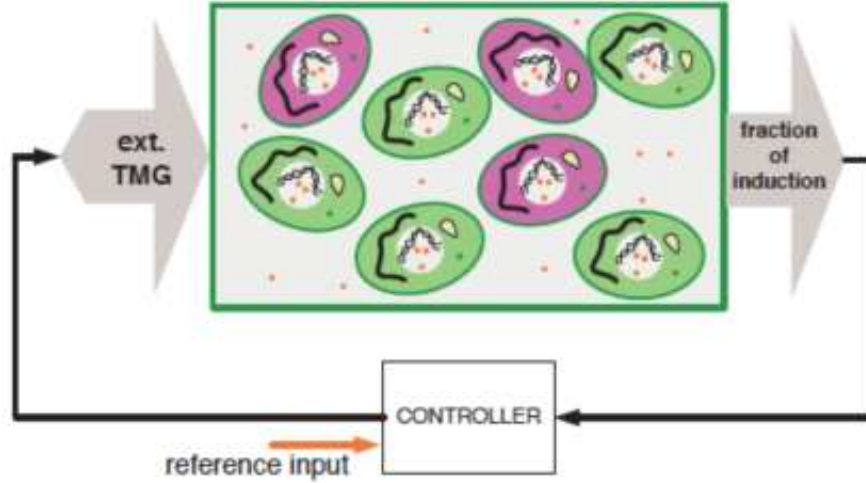
Figure 2.3: Control block diagram for the lactose regulation problem

the form of a global quantity, which we consider as the output of the control system. By this, we mean the controller does not have any information about the individual cells in the colony. Rather, the controller relies on sensing a global quantity, for example, the fraction of induced cells in the population. The control goal is to make the output track a given reference trajectory or attain a desired level. Similar control architecture, where feedback control of a group of Markov chains by adjusting the transition rates has been studied, for example in [58]. There, the plant is a group of artificial muscle cells that can switch between contracting and non-contracting states.

In the second method, a wirelessly-controlled synthetic agent is introduced into a colony of cells. The agent uses the same mechanical and chemical signals that the cells use and communicate with the members of the community in its vicinity to initiate a series of inter-connected interactions among other members. As a result, a collective task is performed by all the members even tough the agent has limited manipulation capability. In one experimental study, authors showed collective decision-making by mixed groups of cockroaches and socially integrated autonomous robots. Individuals were perceived as equivalent due

to pheromone treatment, and the collective decision emerged from local interactions [59].

Chapter 3

Experimental Characterization and Stochastic Modeling of Bacterial Actuation

The work in this chapter was first presented in [60] and was done in collaboration with Edward Steager, Agung Julius, UKei Cheang and Min Jun Kim

3.1   Introduction

The main challenges that need to be addressed in realizing the idea of using bacterial power to actuate microstructures are

1) how to fabricate the structures and integrate the bacteria to them, and

2) what is the behavior of the swarm of bacteria under certain environmental conditions and how to regulate it.

We focus our attention to the chemotactic behavior of flagellated bacteria, such as *Escherichia coli* and *Serratia marcescens*. The motile behavior of these bacteria has been
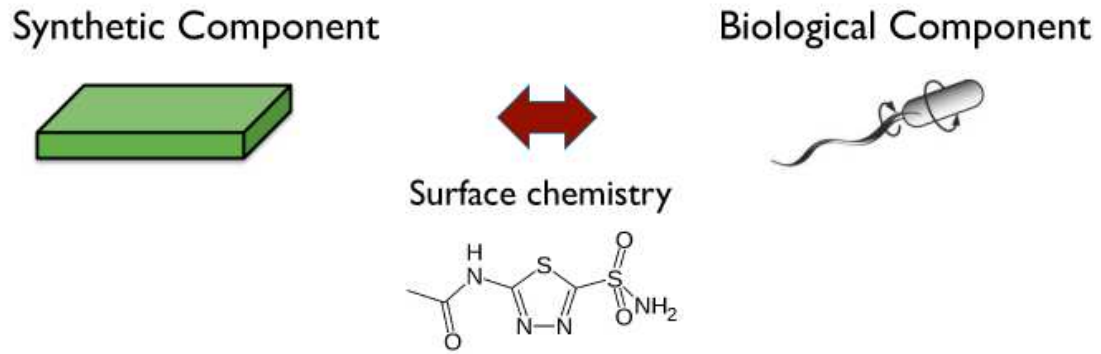
Figure 3.1: Experimental approach. We integrate motile microorganisms with microfabricated structures using a chemical treatment if needed to develop MBRs

extensively studied since the 1970's (c.f. the seminal paper by Howard Berg [61], and a more recent book [62]). It has been established that these bacteria use their flagella to generate propulsion by rotating them [63] and that the motile behavior of the bacteria is similar to a biased random walk toward higher concentration of chemotactic attractant.

We build buoyancy-neutral plate-like microstructures, which we call *microbarges*. We then blot flagellated bacteria on the surface of the microbarge, which is then released to the medium (see Figure 3.1). The motion of the microbarge is carefully tracked and compared with model prediction.

We construct a stochastic mathematical model for the system, based on the assumption that the behavior of each bacterium is random and independent of that of its neighbors. In a recent paper [64], the authors proposed an approximate stochastic model to study the diffusion or random walk properties of microbeads with bacterial propulsion. In this paper, we study smooth and regular propulsion that is potentially more beneficial than random walk. The study of actuation by using a large number of random actuators has also been reported elsewhere, e.g. [58]. In addition to developing the stochastic model, we also perform parameter identification for the model, based on experimental data. We then demonstrate that the model with the estimated parameters is able to predict the behavior of

the system very well. One of the key findings in this paper is that although the system is inherently distributed, in the sense that there are a large number of independent actuators, we can construct an accurate model with only a few parameters representing the distribution of the bacteria.

3.2   Experimental Methods

To accomplish effective actuation of custom designed microstructures several processes are necessary. These processes include culturing bacteria *S. marcescens* using the swarm plate technique, fabricating microstructures, blotting and manipulating microstructures with bacteria into the working fluid, and finally tracking the microstructures using an algorithm to quantify the magnitude and direction of motion.

3.2.1   Cell Culturing

Swarming *S. marcescens* were cultured on a 0.6% agar plate. To prepare agar plates for swarming, 5 g Difco Bacto tryptone, 2.5 g yeast extract, 2.5 g NaCl and 3 g Difco Bacto agar are dissolved into 500 ml of deionized water. After autoclaving the solution was poured into smaller bottles for later redistribution to Petri dishes. Before pouring individual agar plates, the agar solution was mixed with 25 % glucose solution by adding 1 ml glucose solution for 100 ml of prepared agar solution. Then, 50 ml of this new agar solution was pipetted into large 14 cm Petri dishes. The swarm plate was inoculated on one edge with 2 μl of *S. marcescens* saturated culture. Agar plates were incubated at $30 - 34\,^{\circ}$C, and swarming began within 8-16 hours.

3.2.2 Mask design

Masks are an integral component in the photolithographic process of microstructure fabrication. Using AutoCAD, the designed two-dimensional micro-geometry was drawn with precision, and printed onto a transparency film (CAD/Art Service, Inc, Bandon, OR) with high resolution (18,000 dpi). A dark field mask design for microstructures was generated with $50 \times 100 \mu\mathrm{m}^2$ rectangles placed in an array. The distance between each individual pattern was approximately 40 μm to allow working space for extraction of individual microstructures.

3.2.3 Fabrication of Microstructures

The fabricated structures should be biocompatible, i.e. the structure material should preserve and promote bacterial motility and provide a surface to which bacteria can attach readily. Additionally, the composite specific gravity of the structure should be similar to the working fluid and provide both chemical and thermal stability. It is additionally helpful if the fabricated structures are transparent and have a high refractive index to provide clearly defined boundaries which can be readily discerned by a tracking algorithm.

SU8 Series 2 (MicroChem, Newton, MA) negative photoresist forms strong cross links on exposure to ultraviolet (UV) light, and the unexposed regions are easily removed using a developer solution. The SU8 microfabrication and development procedure is compatible with a technique of release using a water-soluble sacrificial dextran layer (27). Traditional techniques for release of structures using a sacrificial layer have required toxic chemicals. Using dextran for the release layer, the motility medium in which the studies are performed acted as an agent of release.

The chosen substrate for the patterning of SU8 microstructures is glass. The fabrication sequence is shown in (Figure 3.2). The first spin-coating procedure was used to prepare
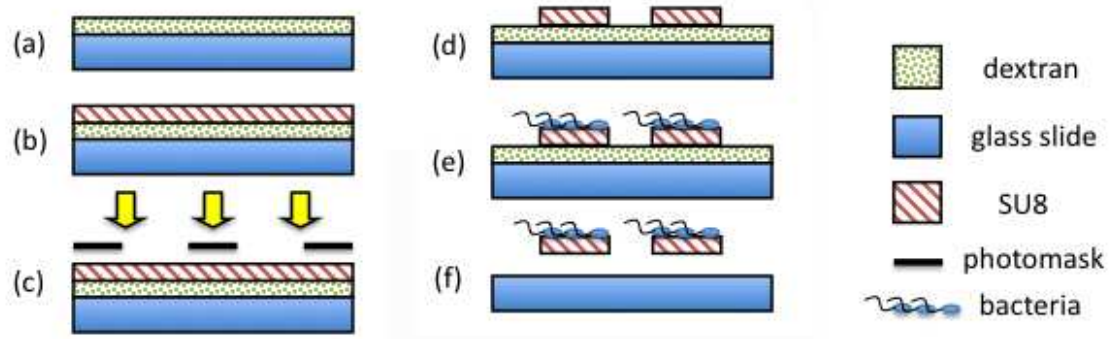
Figure 3.2: Microfabrication of biocompatible SU8 microstructures: (a) The glass slide is coated with Dextran. (b) SU8 layer is spin coated onto the sacrificial dextran layer. (c) UV light is transmitted through a photomask to create an exposure pattern. (d) SU8 photoresist is developed. (e) Sections of the glass slide each with many microstructures are inverted along the swarm edge for bacterial attachment. (f) Individual microstructures are released into motile buffer.

the water-soluble sacrificial dextran layer. An aqueous solution of 5% (w/v) dextran 50-70 kDa was prepared. The solution was dispensed onto the glass slide, spin-coated, and baked. Next, a 5 μm layer of SU8-2 was spin-coated. The exposed substrate was post-baked and developed in Propylene Glycol Monomethyl Ether Acetate (PGMEA). The wafer was then blow dried with a jet of Nitrogen gas, and the SU8 pattern was ready for blotting and then extraction.

3.2.4   Microstructure tracking

A tracking algorithm was designed to analyze the motion of the MBRs in motility buffer. The current study analyzed two distinct motions of rigid bodies, translation and rotation. To characterize the motion of the bacteria-driven microstructures, the geometric centroid and orientation angle was traced. The algorithm was validated by testing the motion and velocity of a theoretical test structure with predetermined shape and velocity.

Imaging was performed on a Leica DMIRB inverted microscope using phase contrast.
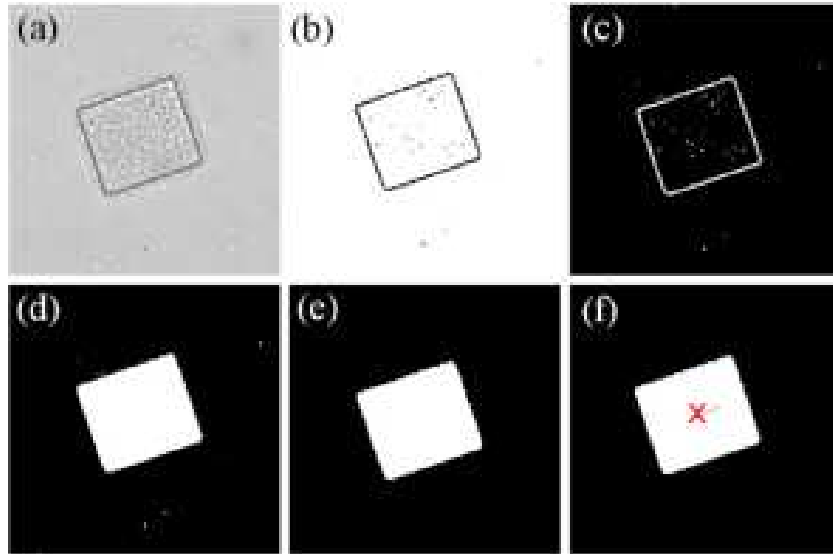
Figure 3.3: Image processing procedure: (a) Phase contrast capture. (b) Binary image tuned threshold. (c) Inverted image. (d) Closed region filling. (e) Size thresholding. (f) Centroid identification

Video was captured using a Retiga 4000R digital camera. A tracking algorithm was designed to analyze the motion of the geometric centroid. Frames of video were captured, digitized and imported directly into MATLAB for analysis. The grayscale images were converted to binary images using a threshold tuned to optimize the effect of edge contrast of the SU8 microstructure. The binary images were then inverted and all closed regions were filled. Closed structures of all sizes were next identified as individual elements, and elements smaller and larger than a predetermined pixel count were deleted leaving the area of the microstructure clearly defined and isolated. Finally, microstructure centroid location and orientation for each frame were determined and written to a data file. This data file is passed to the control algorithm for further analysis.
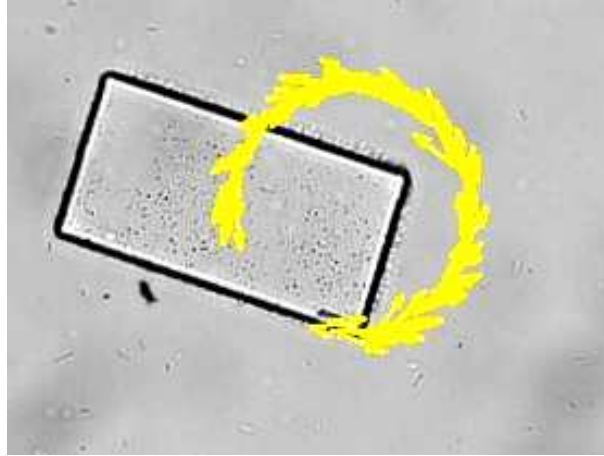
Figure 3.4: A rectangular MBR (50μm x 100μm) that is used in this paper. The computer vision tracking system marks the trajectory of the MBR and its computed interframe velocity with the arrows.

3.3 Experimental Characterization

The swarmer cells of *S. marcescens* are hyperflagellated (10 to 100), elongated (5 to 30 μm) and migrate cooperatively (25). The polysaccharide-rich pink slime produced by bacteria enables them to stick to the surface of the microstructures (26). Bacteria were attached by blotting directly along the active swarm edge and readily adhered to the SU8 microstructures, generally covering more than 90% of the surface. An analysis of the orientation of the attached bacteria showed local correlation. With a fluorescent labeling technique, it was observed that the flagella were free to move even though the cell bodies were fixed. Using a water-soluble sacrificial dextran layer (27), hundreds of MBRs were released into the fluidic chamber without causing structural damage.

MBRs were initially tested without external stimuli, that is, with no electric field or ultraviolet (UV) light. The MBRs were free to move inside the fluid, and their movement due to bacterial actuation was immediately observed. This collective response is due to flagellar actuation of the adherent bacteria and results in translation of the center of mass

combined with rotation (Figure 3.4). We call this *self actuation*.

3.4 Mathematical modeling and analysis

As the hydrodynamic interactions among flagella of neighboring cells are complex and very difficult to model, the model begins with the naive assumption that the cells are independent from each other. Remarkably, this model showed very good agreement with observed results. The unknown parameters of the model are estimated from the experimental results recorded in the beginning of each trial in the absence of external stimuli.

3.4.1 Stochastic kinematic model

The state of the microbarge is characterized by its position on the plane and its orientation. See Figure 3.5 for an illustration. We define the vector $\mathbf{r} = (x, y)$ to be the planar position of the microbarge's center of mass. The orientation of the microbarge is characterized by the angle α, which is formed by the main axis of the microbarge and the x-axis of the inertial coordinate frame.

We assume that there are N_b bacteria attached to a microbarge. The position of the i-th bacterium with respect to the center of mass of the microbarge is denoted by the vector $\mathbf{b}_i = (b_{i,x}, b_{i,y})$ in the body-fixed coordinate frame, and its orientation is characterized by the angle θ_i. We also define the amount of (time varying) propulsive force provided by the i-th bacterium as $p_i(t)$.

The equation of translational motion of the microbarge is given by

$$M\frac{d^2\mathbf{r}}{dt^2} = \sum_{i=1}^{N_b} p_i\psi_i - k_T\frac{d\mathbf{r}}{dt},$$

(3.1)

where M is the total mass of the microbarge system (including the bacteria), ψ_i is the unit
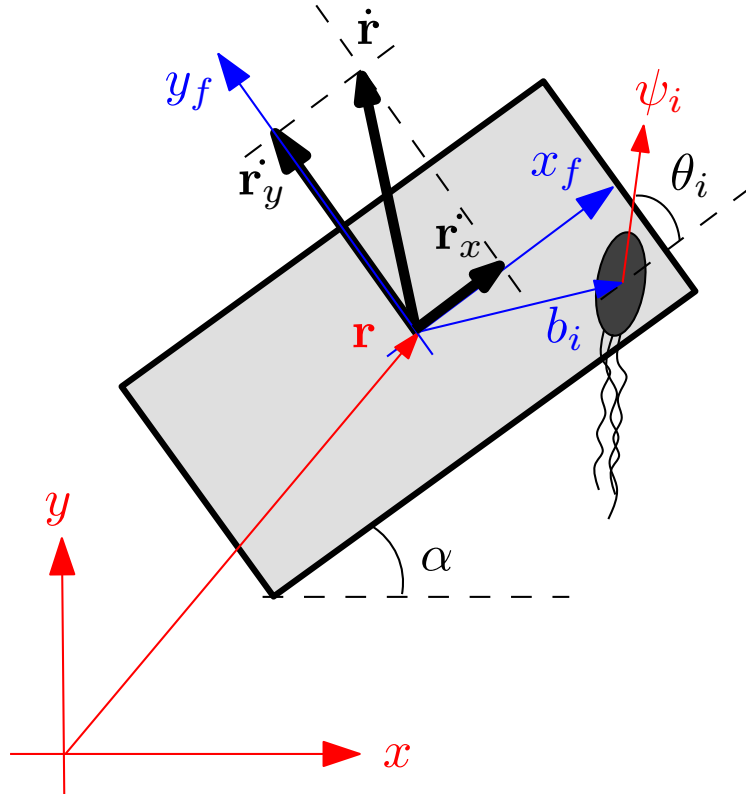
Figure 3.5: A schematic of a microbarge and a bacterium. The angle α is formed by the main axis of the microbarge and the x axis. The vector $\mathbf{r}$ denotes the position of the microbarge's center of mass. The vector b_i denotes the position of the i-th bacterium w.r.t the microbarge's center of mass. The vector ψ_i is a unit vector that denotes the orientation of the i-th bacterium. The angle θ_i is formed by the microbarges main axis and the orientation of the i-th bacterium.

vector in the inertial coordinate frame that represents the orientation of the i-th bacterium, and k_T is the translational viscous drag coefficient. Similarly, the rotational motion can be characterized by

$$I\frac{d^2\alpha}{dt^2} = \sum_{i=1}^{N_b} p_i \cdot (b_{i,x}\sin\theta_i - b_{i,y}\cos\theta_i) - k_R\frac{d\alpha}{dt}, \tag{3.2}$$

where I is the total moment of inertia of the microbarge system and k_R is the rotational viscous drag coefficient. In an environment with very low Reynolds number, the inertia effect is negligible, i.e. $k_T \gg M,\ k_R \gg I$.

Consequently, the translational and the rotational accelerations are negligible. Therefore, (3.1) and (3.2) can be accurately replaced with

$$\frac{d\mathbf{r}}{dt} = \frac{1}{k_T}\sum_{i=1}^{N_b} p_i\psi_i, \tag{3.3a}$$

$$\omega := \frac{d\alpha}{dt} = \frac{1}{k_R}\sum_{i=1}^{N_b} p_i \cdot (b_{i,x}\sin\theta_i - b_{i,y}\cos\theta_i). \tag{3.3b}$$

The propulsion forces, $p_i(t)$, are stochastic processes. Biological investigation by Berg *et al* [43] reveals that in the absence of chemotactic chemical agents, the process can be accurately modeled as a continuous-time Markov chain [65] with two states, *run* and *tumble* (see Figure 3.6). We assume that during *tumble*, a bacterium does not provide any propulsion, while during *run* it delivers the maximal propulsive force of $p_{\max} = 0.45$ pN reported in the literature [66].

If we define $\phi(t) = (\phi_1(t), \phi_2(t))^T$ as the probability of finding the system in the *run* and *tumbling* state at time t, the evolution of $\phi(t)$ is given by

$$\frac{d}{dt}\begin{bmatrix} \phi_1 \\ \phi_2 \end{bmatrix} = \begin{bmatrix} -\lambda_1 & \lambda_2 \\ \lambda_1 & -\lambda_2 \end{bmatrix}\begin{bmatrix} \phi_1 \\ \phi_2 \end{bmatrix}. \tag{3.4}$$
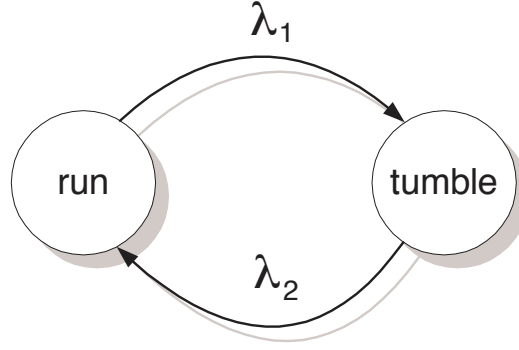
Figure 3.6: A two-state continuous Markov chain model for the stochastic behavior of the bacteria. The transition rates between the states are given as λ_1 and λ_2. In chemical attractant free environment, measurements in biological experiments reveal that $\lambda_1 = 1 \text{ s}^{-1}$ and $\lambda_2 = 10 \text{ s}^{-1}$.

From here, it follows that any initial distribution $\phi(0)$ converges exponentially to a steady state distribution given by

$$\begin{bmatrix} \phi_1(\infty) \\ \phi_2(\infty) \end{bmatrix} = \begin{bmatrix} \frac{\lambda_2}{\lambda_1 + \lambda_2} \\ \frac{\lambda_1}{\lambda_1 + \lambda_2} \end{bmatrix}. \tag{3.5}$$

3.4.2 Quantitative analysis of the microbarge rotation

If we denote the parameter

$$c_i := \frac{b_{i,x} \sin \theta_i - b_{i,y} \cos \theta_i}{k_R}, \tag{3.6}$$

then the orientation of the barge α satisfies the following relation

$$\alpha(t) = a(0) + \int_0^t \sum_{i=1}^{N_b} c_i \cdot p_i(\tau) \, d\tau. \tag{3.7}$$

From here, we can compute the expectation of $\alpha(t)$ as

$$E(\alpha(t)) = \alpha(0) + \bar{p}\sum_{i=1}^{N_b}c_i t. \tag{3.8}$$

Here we use the assumption that at the beginning of the time interval of interest, $t = 0$, the processes $p_i(t)_{i=1...N_b}$ have reached their steady state. In that case, their expectation is then given by the steady state expected value, $\bar{p}$, which can be computed as

$$\bar{p} = \frac{\lambda_2}{\lambda_1 + \lambda_2} \cdot p_{\max} = 0.41 \text{ pN}. \tag{3.9}$$

Similarly, we can compute the variance of $\alpha(t)$ as follows.

$$\text{Var}(\alpha(t)) = E\left(\int_0^t \sum_{i=1}^{N_b} c_i \cdot (p_i(\tau) - \bar{p}) \, d\tau\right)^2,$$

$$= E\left(\int_0^t \int_0^t \sum_{i=1}^{N_b} c_i \cdot (p_i(\tau) - \bar{p}) \sum_{j=1}^{N_b} c_j \cdot (p_j(\eta) - \bar{p}) \, d\tau \, d\eta\right),$$

$$= \int_0^t \int_0^t \sum_{i=1}^{N_b} \sum_{j=1}^{N_b} c_i \cdot c_j \cdot \left(E\left(p_i(\tau)p_j(\eta)\right) - \bar{p}^2\right) \, d\tau \, d\eta. \tag{3.10}$$

Assuming that the random behavior of the bacteria are independent one from another, we can simplify (3.10) into

$$\text{Var}(\alpha(t)) = 2\int_0^t \int_\eta^t \sum_{i=1}^{N_b} c_i^2 \cdot \left(E\left(p_i(\tau)p_i(\eta)\right) - \bar{p}^2\right) \, d\tau \, d\eta. \tag{3.11}$$

Furthermore, using the above mentioned assumption that the processes have reached the steady state at $t = 0$, we can compute $E\left(p_i(\tau)p_i(\eta)\right)$ through the Bayesian formula. The values of $P\left\{(p_i(\tau) = A), (p_i(\eta) = B)\right\}$ is given in the following table.

31

$A\backslash B$	$p_{\max}$	0
$p_{\max}$	$\dfrac{\lambda_2^2+\lambda_1\lambda_2 e^{(\lambda_1+\lambda_2)(\eta-\tau)}}{(\lambda_1+\lambda_2)^2}$	$\dfrac{\lambda_1\lambda_2-\lambda_1\lambda_2 e^{(\lambda_1+\lambda_2)(\eta-\tau)}}{(\lambda_1+\lambda_2)^2}$
0	$\dfrac{\lambda_1\lambda_2-\lambda_1\lambda_2 e^{(\lambda_1+\lambda_2)(\eta-\tau)}}{(\lambda_1+\lambda_2)^2}$	$\dfrac{\lambda_1^2+\lambda_1\lambda_2 e^{(\lambda_1+\lambda_2)(\eta-\tau)}}{(\lambda_1+\lambda_2)^2}$

We can compute that

$$E\left(p_i(\tau)p_i(\eta)\right) = \frac{\lambda_2^2 + \lambda_1\lambda_2 e^{(\lambda_1+\lambda_2)(\eta-\tau)}}{(\lambda_1 + \lambda_2)^2} p_{\max}^2, \tag{3.12}$$

and

$$\mathrm{Var}(\alpha(t)) = \frac{2\lambda_1\lambda_2 p_{\max}^2}{(\lambda_1 + \lambda_2)^3}\sum_{i=1}^{N_b} c_i^2 \cdot \left(t - \frac{1 - e^{-(\lambda_1+\lambda_2)t}}{\lambda_1 + \lambda_2}\right). \tag{3.13}$$

From (3.13), we see that both the expectation and the variance of $\alpha(t)$ grow asymptotically linearly. The standard deviation of $\alpha(t)$ grows asymptotically with $\sqrt{t}$, which is half an order slower than the expectation. Consequently, as $t \to \infty$, the ratio of the standard deviation to the expectation goes to 0. This means the expectation can be used as a good estimate of the steady state behavior of the system. The expectation of $\alpha(t)$ predicts that the microbarge undergoes a steady rotation as a steady state behavior. In the next section, we will see that this is justified by the experimental results (see Figure 3.8(a)).

Notice that the assumption that the random behavior of the bacteria are independent one from another is not essential in deriving this result. To see this, consider the extreme case, where all the bacteria are perfectly correlated. In this case, the term $\sum_{i=1}^{N_b} c_i^2$ in (3.13) will be replaced by $\sum\sum_{i,j=1}^{N_b} c_i c_j$, which does not change the conclusion.
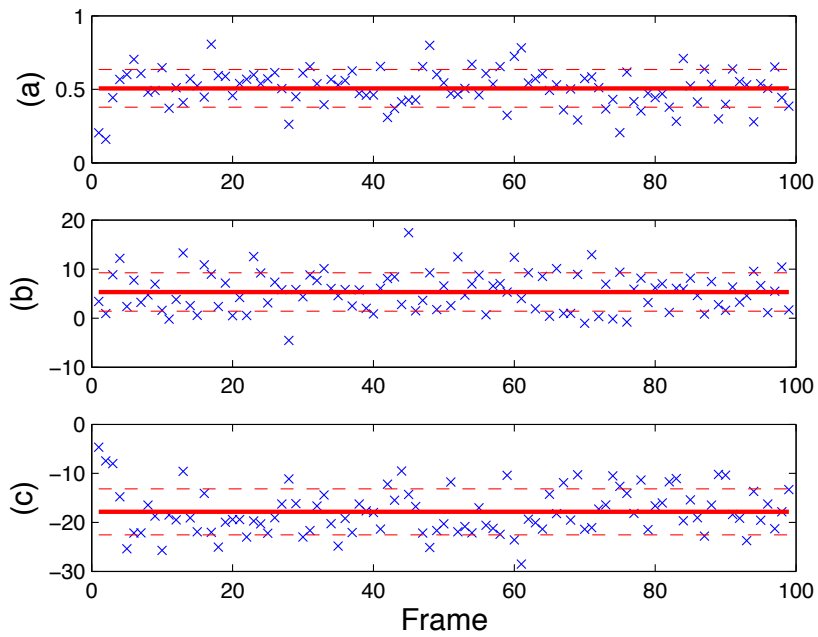
Figure 3.7: The computed data for a rectangular microbarge (50 μm $\times$ 100 μm). (a) $\{\bar{\omega}_i\}$ in rad/s, (b) $\{\bar{v}_{x,i}\}$ in μm/s, (c) $\{\bar{v}_{y,i}\}$ in μm/s. The solid lines show the averages of the data, while the gaps between the solid lines and the dashed lines represent the standard deviations.

3.5 Parameter estimation and model validation

The components of the translational velocities on the axis of the body fixed coordinate frame (see Figure 3.5) are

$$v_x := \dot{r}_x = \frac{1}{k_T} \sum_{i=1}^{N_b} p_i \cos \theta_i, \ v_y := \dot{r}_y = \frac{1}{k_T} \sum_{i=1}^{N_b} p_i \sin \theta_i. \tag{3.14}$$

Their respective expectations are then given by

$$E v_x = \frac{\bar{p}}{k_T} \sum_{i=1}^{N_b} \cos \theta_i, \ E v_y = \frac{\bar{p}}{k_T} \sum_{i=1}^{N_b} \sin \theta_i. \tag{3.15}$$

From (4.1), we can obtain the expectation of the angular velocity of the microbarge, which is given by

$$E \omega = \frac{\bar{p}}{k_R} \sum_{i=1}^{N_b} \left(b_{i,x} \sin \theta_i - b_{i,y} \cos \theta_i \right). \tag{3.16}$$

It is clear from (14-16) that the expected velocities only depend on three parameters:

$$\beta_1 := \frac{1}{k_T} \sum_{i=1}^{N_b} \cos \theta_i, \ \beta_2 := \frac{1}{k_T} \sum_{i=1}^{N_b} \sin \theta_i,$$

$$\beta_3 := \frac{1}{k_R} \sum_{i=1}^{N_b} \left(b_{i,x} \sin \theta_i - b_{i,y} \cos \theta_i \right).$$

3.5.1 Parameter estimation

We estimate the values of these parameters using experimental data. We extract frames from the video taken during the experiment. In each frame, the position and orientation of the barge are identified using digital image processing. As the results, we have three time series $\{\bar{x}_i\}$, $\{\bar{y}_i\}$, and $\{\bar{\alpha}_i\}$, with $i = 1, \ldots, N$, consisting of the planar position of the barge and its orientation in N frames. The body fixed coordinate components of the microbarge's

34

translational velocity at the i-th frame can be approximated by using the forward difference method as follows.

$$\begin{bmatrix} \bar{v}_{x,i} \\ \bar{v}_{y,i} \end{bmatrix} = \frac{1}{\delta} \begin{bmatrix} \cos \bar{\alpha}_i & \sin \bar{\alpha}_i \\ -\sin \bar{\alpha}_i & \cos \bar{\alpha}_i \end{bmatrix} \begin{bmatrix} \bar{x}_{i+1} - \bar{x}_i \\ \bar{y}_{i+1} - \bar{y}_i \end{bmatrix}, \tag{3.17}$$

for $i \in \{1, \ldots, N-1\}$, where δ is the video sampling rate. Similarly, the angular velocity of the microbarge can be extracted from the video data by $\bar{\omega}_i = \frac{\bar{\alpha}_{i+1} - \bar{\alpha}_i}{\delta}$.

By equating the averages and the expectations of the microbarge's translational and angular velocities, we can estimate the values of $\beta_{1,2,3}$ as follows.

$$\begin{bmatrix} \beta_1 & \beta_2 & \beta_3 \end{bmatrix} \approx \frac{1}{\bar{p}(N-1)} \sum_{i=1}^{N-1} \begin{bmatrix} \bar{v}_{x,i} & \bar{v}_{y,i} & \bar{\omega}_i \end{bmatrix}.$$

Figure 3.7 shows the computed $\{\bar{\omega}_i\}$, $\{\bar{v}_{x,i}\}$, and $\{\bar{v}_{y,i}\}$ for a rectangular microbarge ($50 \ \mu\text{m} \times 100 \ \mu\text{m}$) as shown in Figure 3.4. The video length is 10 seconds, sampled at 10 frames/second. Based on this data, the parameters for this microbarge are computed as $\beta_1 = 13.03 \ \frac{\mu\text{m}}{\text{s pN}}$, $\beta_2 = -43.64 \ \frac{\mu\text{m}}{\text{s pN}}$, and $\beta_3 = 1.24 \ \frac{\text{rad}}{\text{s pN}}$.

The three parameters $\beta_{1,2,3}$ summarize the distribution of the bacteria on the micro-barge. Subsequently, we will show that our mathematical model and the parameters $\beta_{1,2,3}$ can predict the behavior of the system reasonably well.

3.5.2 Model validation

In this subsection, we show that the mathematical model developed in the previous section and the parameters $\beta_{1,2,3}$ can predict the behavior of the system reasonably well. We construct a deterministic model by replacing the stochastic processes $p_i(t)$ in (4.1) with their steady state expectations $\bar{p}$. We therefore construct a reduced-order model for the system, which is given by
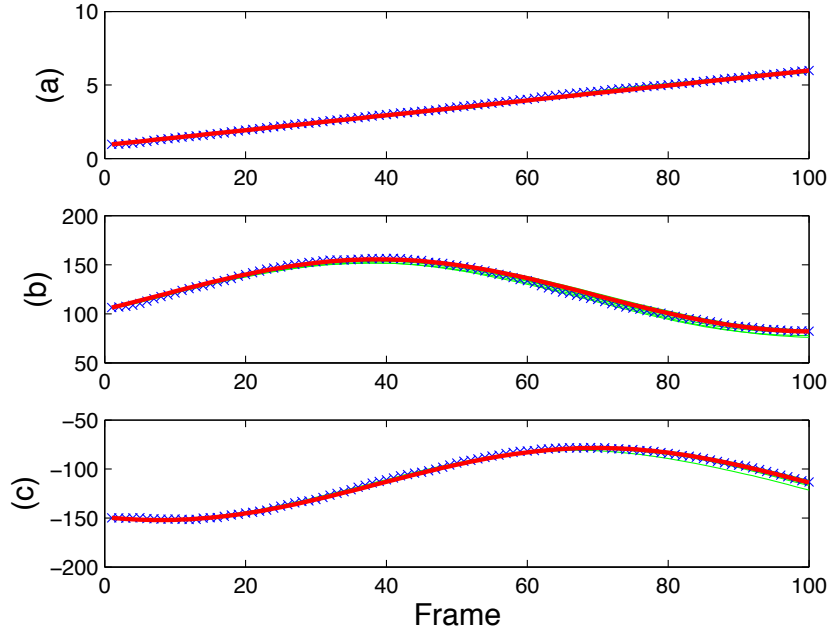
Figure 3.8: The comparison between the experimental data (x), the deterministic model prediction (thick line), and stochastic simulations (solid lines) for a rectangular microbarge (50 μm $\times$ 100 μm). (a) α in rad/s, (b) x in μm, (c) y in μm.

$$
\begin{aligned}
\frac{dx}{dt} &= \bar{p}\left(\beta_1 \cos \alpha - \beta_2 \sin \alpha\right), \\
\frac{dy}{dt} &= \bar{p}\left(\beta_1 \sin \alpha + \beta_2 \cos \alpha\right), \\
\frac{d\alpha}{dt} &= \bar{p}\beta_3.
\end{aligned}
$$

Figure 3.8 shows the comparison between the experimental data, the deterministic model prediction and the stochastic simulations of the model (4.1) for the rectangular microbarge that is analyzed in the previous section. Note that for each simulation run, the distribution of 300 bacteria on the microbarge is randomized while keeping the parameters $\beta_{1,2,3}$ constant.

We can see that the model with fitted parameter can explain the data very well, sug-

gesting that the structure of the model is suitable for this experimental setup. Furthermore, we can observe that the distributed parameter model that includes the description of the distribution of the bacteria on the microbarge ($\mathbf{r}_i$ and θ_i) can be replaced with a lumped parameter model with the initial state of the system and three parameters of bacterial distribution ($\beta_{1,2,3}$). Therefore, in order to describe the dynamics of the system accurately, it is not necessary to know how the bacteria are distributed precisely. Rather, it is sufficient to know a few high level parameters that describe the distribution.

3.5.3 The effect of orientation coherence on microbarge actuation

Due to the nature of the blotting process, the distribution of the bacteria on the microbarge (both position and orientation) is inherently random. In this subsection, we analyze the effect of coherence in the orientation distribution and the kinematic behavior of the microbarge.

Consider the expectation of the magnitude of the translational velocity of the microbarge, as given in (4.1a).

$$E \left\| \frac{d\mathbf{r}}{dt} \right\| = \frac{\bar{p}}{k_T} \left\| \sum_{i=1}^{N_b} \psi_i \right\|. \tag{3.18}$$

Since this quantity does not depend on the choice of coordinate frame, we can conveniently evaluate it in the body fixed coordinate frame. In this case, the right hand side becomes

$$\frac{\bar{p}}{k_T} \left\| \sum_{i=1}^{N_b} \psi_i \right\| = \frac{\bar{p} N_b}{k_T} \left(\frac{1}{N_b^2} \sum_{i=1}^{N_b} \sum_{j=1}^{N_b} \cos(\theta_i - \theta_j) \right)^{\frac{1}{2}}. \tag{3.19}$$

The quantity between the brackets in (3.19) can be seen as a measure of the coherence of the orientation of bacteria. If all of them have the same orientation, this quantity is 1. If there is no correlation between the orientation, the expected value of the cosine function is zero, and so is this quantity. We can therefore propose a measure of orientation coherence,
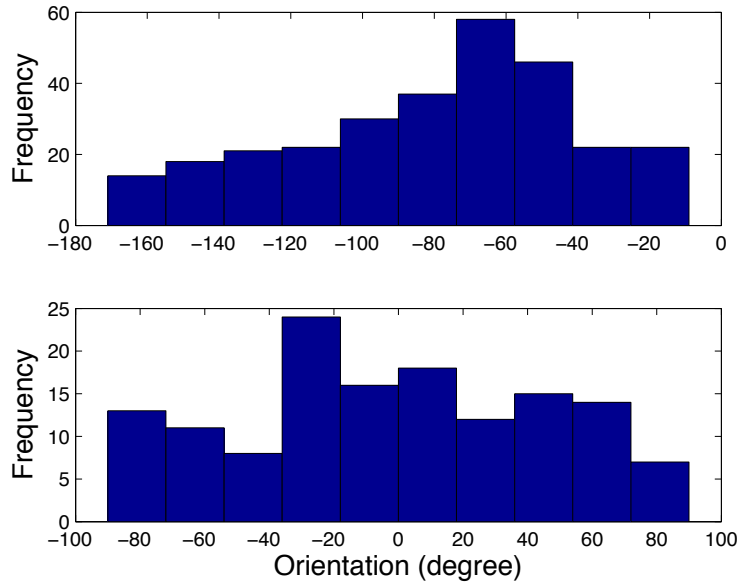
Figure 3.9: Histograms of the orientation of the bacteria on Microbarge A (top) and Micro-barge B(bottom).

based on experimental data, as $\gamma := v_{\mathrm{avg}} k_T / (\bar{p} N_b)$. By comparing measurements from two different microbarges, we can justify this idea.

From images, we can extract some information about the distribution of the bacteria on their surface. Through digital image processing, we can extract the information about the alignment of the major axis of the bacteria on both microbarges. The statistics of this data is shown in Figure 3.9.

We can compute γ for both microbarges by using the recorded average velocities and the number of identified bacteria on each microbarge. The γ values are $\gamma_A = 0.157 k_T$ and $\gamma_B = 0.5154 k_T$. Visual inspection on the histograms shown in Figure 3.9 does not reveal too much information about the orientation coherence in both microbarges. However, we can approximately[1] compute the term between brackets in (3.19) for both barges, which are 0.37 and 0.49 for Microbarge A and B, respectively. Therefore, it is likely that the bacteria

---

[1]Not all bacteria can be successfully identified by the digital image processing algorithm. Moreover, the identified orientation is that of the major axis of the bacteria, instead of the bacteria themselves.

are more coherently oriented on Microbarge B than on Microbarge A.

3.6 Discussion

In this chapter, we developed a model of a microstructure blotted with bacteria moving in a micro channel propelled by the flagella of the bacteria. The main contribution is the reduction of the complex dynamics of the system of bacteria and the microstructure to a system of three ordinary differential equations with only three parameters. The predictions from the reduced-order model are consistent with the experimental data for the motion of the microstructure. In the next chapter, we will extend the model to incorporate the effect of dc electric fields on the motion of MBRs.

Chapter 4

Electrokinetic and optical control of bacterial microrobots

The work in this chapter was first presented in [67,68] and was done in collaboration with Edward Steager, Dalhyung Kim and Min Jun Kim

4.1 Introduction

In the previous chapter, we constructed a stochastic mathematical model for the self actuation, based on the assumption that the behavior of each bacterium is random and independent of that of its neighbors. In addition to developing the stochastic model, we also performed parameter identification for the model, based on experimental data. We then demonstrated that the model with the estimated parameters is able to predict the behavior of the system very well. One of the key findings is that although the system is inherently distributed, in the sense that there are a large number of independent actuators, we can construct an accurate model with only a few parameters representing the distribution of the bacteria.
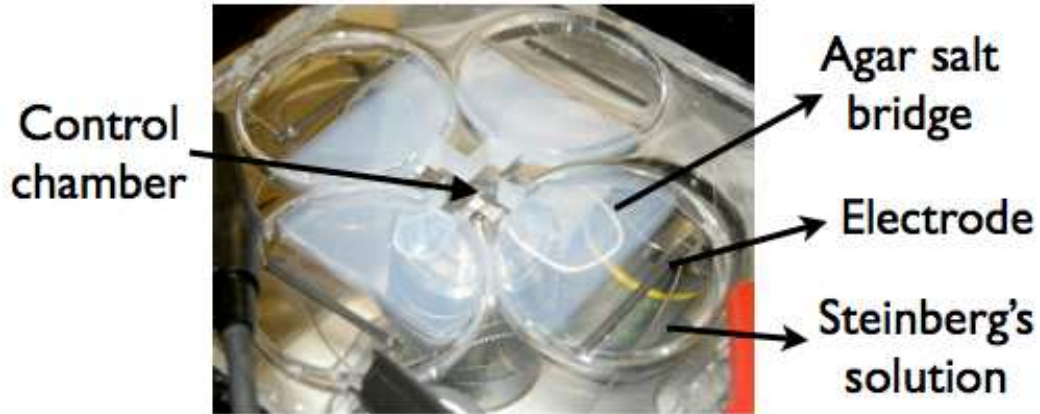
Figure 4.1: Photograph of the PDMS galvanotaxis chamber. All experimental observations were performed in the central portion of the control chamber.

In this chapter, we demonstrate the control of MBRs using DC electric fields, and develop an experimentally validated mathematical model for the MBRs. This model allows us to steer the MBR to any position and orientation in a planar micro channel using visual feedback from an inverted microscope. We demonstrate that our approach allows us to steer MBRs along arbitrary trajectories in an autonomous fashion [67]. The control algorithm steers the robots along their desired paths even if the properties of the robots (their charge, size and shape) and the properties of the fluid (pH, the zeta potential, temperature) are not known precisely. We also characterize the overall system performance by applying sinusoidal control voltages to the system with varying frequencies. The method is wireless and non-invasive, and the entire system can be miniaturized further.

4.2   Fabrication of experimental chamber

All experiments were conducted in a polydimethylsiloxane (PDMS) chamber on a 50×50 mm^2 glass plate (see Figure 4.1). Direct current (d.c.) electric fields (EFs) were applied to the MBRs via agar salt bridges, Steinberg's solution (60 mM NaCl, 0.7 mM KCl, 0.8

mM MgSO$_4\cdot$7H$_2$O, 0.3 mM CaNO$_3\cdot$4H$_2$O) and graphite electrodes. It has been shown that salt bridges avoid contamination of possible electrode byproducts by successfully applying electric fields to a variety of cell types using similar devices [69]. They also keep bubbles formed around electrodes outside the control chamber. The temperature, calcium level and pH are normally very stable inside chamber within the 1-hour duration of experiments [70]. This design was optimized to apply EFs efficiently in multiple directions. In order to minimize the possible adverse effects of electrode byproducts, we used graphite electrodes. The electrodes were fixed in parallel horizontal positions inside the compartments filled with Steinberg's solution to generate uniform EFs all over the control chamber. The control chamber was filled with motility buffer (0.01 M potassium phosphate, 0.067 M sodium chloride, 10^{-4} M ethylenediaminetetraacetic acid (EDTA), and 0.002% Tween-20, pH 7.0). Observations were performed in the central portion of the control chamber where dielectrophoretic effects due to field nonlinearities are minimized.

4.3 Data acquisition and analysis

Imaging was performed on a Leica DMIRB inverted microscope with automated stage using both phase contrast. Videos were captured using a high-speed camera (MotionPro X3, Redlake) with a frame rate of 30 frames/s. A simple tracking algorithm was designed to feedback the position and orientation of the MBR in the motility buffer. The control algorithm and the serial port connection protocol to interface with the programmable power supply for the electrodes were written in MATLAB 7.0. Voltages were applied to the control chamber through a National Instruments PCI-6713 analog output board. Two analog output channels were routed to two single channel Ametek XTR 100-8.5 amplifiers using analog programming mode in conjunction with isolated connectors. Two additional analog output channels were used to control double pole, double throw (DPDT) switches, which

functioned to reverse polarity of the system.

4.4 Electrophysiology of bacteria

Because bacteria are charged, an electric field exerts an electrostatic Coulomb force on the particles. Thus the individual bacteria and therefore the MBR exhibit electrophoresis. A series of experiments were performed to characterize the effect of electric fields on the orientation of freely swimming S. marcescens. This study was performed to determine which electrokinetic phenomena cause directed movement of the MBRs. Upon application of electric fields in the range of 1-10 V/cm bacteria showed a uniform tendency to move toward the positive electrode; however, it was difficult to observe if the cells were orienting along electric field lines, as would be expected in the case of bacterial galvanotaxis. Due to the fact that preferential orientation may take several seconds to develop, 20 s were allowed to pass after electric fields were applied, but before images were taken. Between image acquisitions at discrete voltages, several seconds were allowed to pass to account for potential charging/discharging of the agar electrodes. Images were processed using MATLAB, and orientation was evaluated on a basis of 180 since the polarity of the flagellar bundle cannot be resolved using phase contrast microscopy.

Experiments with individual bacteria showed that the movement is electrophoresis caused by the inherent charge of the bacterial cells rather than galvanotaxis, a directed response arising from the thrust of the bacterial flagella. Galvanotaxis in bacteria is caused by a difference in electrophoretic mobility between the cell body and flagellum (29). Unlike previous observations made on swimming cells of *Escherichia coli* and *Salmonella typhimurium*, swarmer cells of *S. marcescens* did not align themselves along the applied electric fields (see Figure 4.2). The results of experiments designed to study the fundamental electrokinetics of individual bacteria indicated that there was not a significant effect of electric fields on
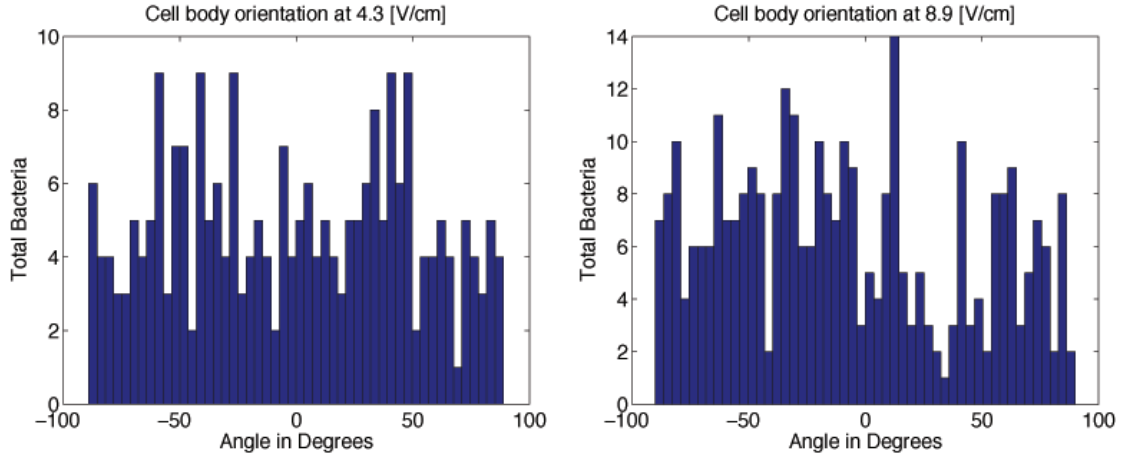
Figure 4.2: Histograms of the cell body orientation of *S. marcescens* at electrics fields of 4.3 and 8.9 V/cm. Electric fields were coincident with zero degrees. The individual cells do not exhibit galvanotaxis as might be expected, and distributions are relatively uniform across the range of angles.

the orientation of *S. marcescens* for the experimental conditions of this research, with a uniform distribution of orientations across the range of angles and applied electric fields. This would imply that there is not a significant difference in electrophoretic mobility between the flagella and the cell body. Despite the uncorrelated orientations between cells, with the increased strength of EFs cells were pulled towards the positive electrode involuntarily while trying to swim in random directions. Thus, the bulk cell movement is electrophoretic in nature due to negative surface charge. It should be emphasized that the cells in this study were swarm cells taken directly from the agar plate to reflect the morphology of the cells blotted on the MBRs.

4.5   Model for electrokinetic actuation

In order to develop a model for electrophoresis, two sets of experiments were performed. First, the SU8 microstructures were tested in the experimental chamber without bacteria attached using DC electric fields ranging from 1-10 V/cm. For the electric fields applied

during these experiments, the structures demonstrated no movement that might be expected due to electrokinetic effects. In the next set of experiments, electric fields ranging from 1-10 V/cm were applied to the MBRs. They responded by immediately seeking the positive electrode with a directed movement that was primarily translational, but also includes some rotation because of *self actuation*. Upon switching the polarity of the field, the motion immediately reversed direction. This investigation yielded a linear relationship between the two parameters reflective of electrophoretic movement (Figure 4.3). Thus, the detailed motion of the MBR could be accurately modeled by a sum of the movement due to the self-coordinating, unstimulated movement and electrophoretic movement. Indeed, surface patterning of bacteria imparts a charge that leads to a direct mechanism of translational control of the MBR.

We now extend the model developed in the previous section to incorporate electrokinetic actuation (See Figure 4.4). If each of the N_b bacteria in the MBR is subject to the same electric field, we arrive at the stochastic kinematic model:

$$\frac{dr}{dt} = \frac{1}{k_T}\{\sum_{i=1}^{N_b} p_i n_i + N_b(\epsilon_C|E|)u\},$$
(4.1a)

$$\frac{d\alpha}{dt} = \frac{1}{k_R}\{\sum_{i=1}^{N_b} p_i \cdot (b_{i,x}\sin\theta_i - b_{i,y}\cos\theta_i) +$$

$$(\epsilon_C|E|)\sum_{i=1}^{N_b}(b_{i,x}\sin(\Psi - \alpha) - b_{i,y}\cos(\Psi - \alpha))\}.$$
(4.1b)

where the strength of the electric field is denoted by $|E|$ and u is the unit vector that represents the direction of the electrophoretic force exerted on each bacterium. The strength of the electrophoretic force is given by $\epsilon_C|E|$ where ϵ_C is a constant related to the charge of the cell body.

Experimental observations suggest that the angular velocity of the MBR is not modu-
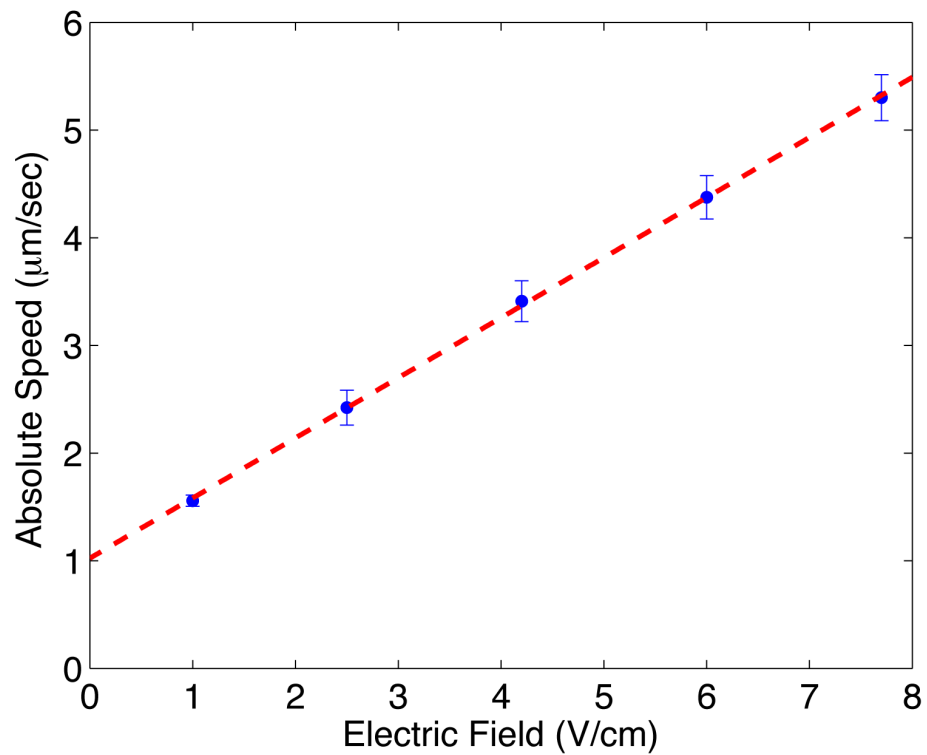
Figure 4.3: MBR speed is directly proportional to applied electric field which shows electrophoresis is the dominant electrokinetic phenomenon. The component of speed due to self actuation appears as an offset along the vertical axis.
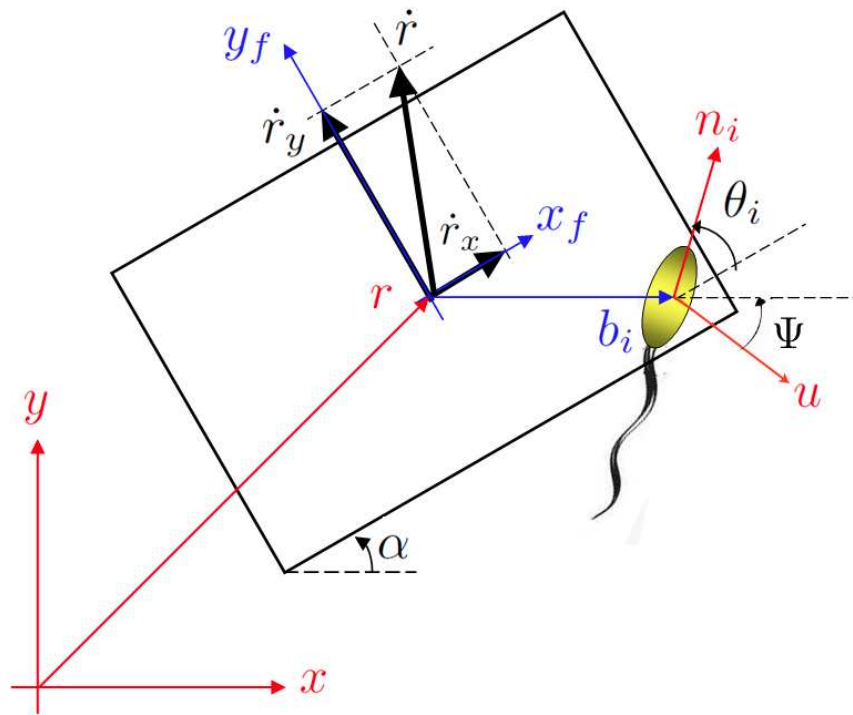
Figure 4.4: A schematic of an MBR. The angle α is formed by the main axis of the MBR and the x axis. The vector $\mathbf{r}$ denotes the position of the MBR's center of mass. The vector b_i denotes the position of the i-th bacterium w.r.t the MBR's center of mass. The vector n_i is a unit vector that denotes the orientation of the i-th bacterium. The angle θ_i is formed by the MBR's main axis and the orientation of the i-th bacterium. The angle Ψ is the angle between the direction of electrophoretic force u and the x axis.

lated by the application of the electrical fields. In other words, the observed angular veloc-
ity with the application of electrical fields was indistinguishable from the angular velocity
under self actuation. We conclude that if the whole surface of the MBR is coated with a
monolayer of bacteria, the moments due to the applied electric field must be zero. In other
words,

$$\sum_{i=1}^{N_b} (b_{i,x} \sin(\Psi - \alpha) - b_{i,y} \cos(\Psi - \alpha)) = 0 \tag{4.2}$$

This simplifies the model. The expected velocities can be derived from the stochastic
kinematic model:

$$Ev_x = \beta_1 \bar{p} + \beta_4 u_x \tag{4.3}$$

$$Ev_y = \beta_2 \bar{p} + \beta_4 u_y \tag{4.4}$$

$$E\omega = \beta_3 \bar{p} \tag{4.5}$$

where $\beta_4 = (1/k_T)N_b\epsilon_C$ is experimentally determined via linear regression from experi-
mental data (Figure 4.3).

The comparison of the experimental observations with theoretical predictions is shown
for a representative experiment in Figure 4.5 and Figure 4.6 with a 40×45 μm^2 rectangular
MBR with the parameters $\beta_1 = -6 \times 10^{12}$ $\mu m \cdot s^{-1} N^{-1}$, $\beta_2 = -5 \times 10^{12}$ $\mu m \cdot s^{-1} N^{-1}$,
$\beta_3 = -0.43 \times 10^{12}$ $rad \cdot s^{-1} N^{-1}$, and $\beta_4 = 0.56 \times 10^4$ $\mu m^2 \cdot s^{-1} V^{-1}$. In the first part of
the experiment, we recorded a video of the motion of the MBR in the absence of external
stimuli showing motility due to self actuation. We estimated the values of $\beta_{1,2,3}$ using the
processed data as described in the previous section. Compared to the match we obtained
in the previous chapter for the larger rectangular MBR, there is more discrepancy between
experimental data and simulation results. As the number of random actuators decreases,
the motion of the MBR becomes more unpredictable. A small change in the orientation
of one of the bacterium would cause an observable change in the overall MBR motion
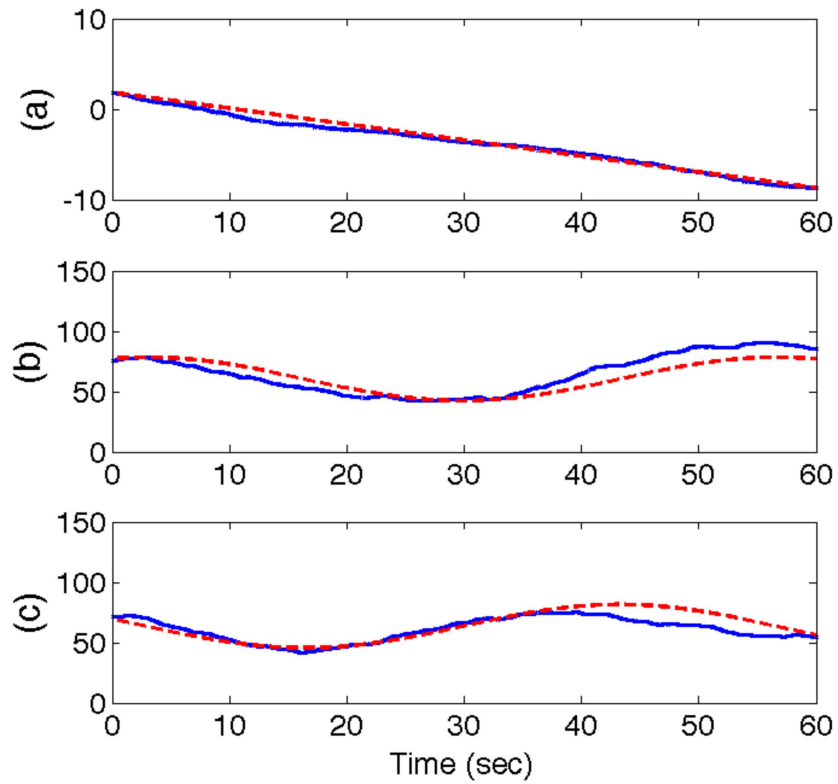
Figure 4.5: The comparison between the experimental data (blue line) and the model prediction (red line) for a rectangular MBR (40 μm × 45 μm) showing self actuation. (a) α in rad, (b) x in μm, (c) y in μm
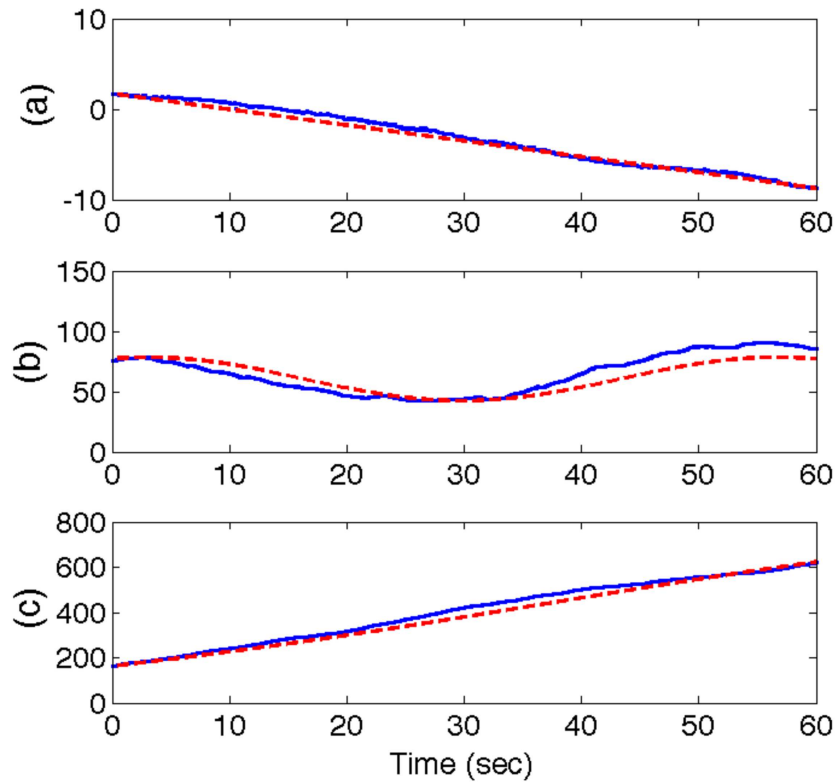
Figure 4.6: The comparison between the experimental data (blue line) and the model prediction (red line) for a rectangular MBR ($40\ \mu$m $\times\ 45\ \mu$m). $10V/cm$ was applied to the MBR in $+y$ direction. (a) α in rad, (b) x in μm, (c) y in μm

if the applied force by this bacterium is comparable to the net force acting on the robot. This change could be due to loose attachment of the bacterium. We fabricated smaller microstructures with sizes less than 10 μm and they showed even more erratic behavior.

During the second part of the experiment, 10 $V \cdot cm^{-1}$ was applied to the MBR in $+y$ direction. There was no significant variation in the angular velocity or the translational velocity in x direction as expected. The observed difference could be initiated by galvan-otaxis, a directed response arising from the thrust of the bacterial flagella. Galvanotaxis in bacteria is caused by a difference in electrophoretic mobility between the cell body and flagellum [71]. The MBR moved with a constant velocity of 7 $\mu m \cdot s^{-1}$ in $+y$ direction. The electrokinetic model with the fitted parameters can explain the data well, suggesting that the overall structure of the model is suitable for this system.

One shortcoming of the model that may explain the slight deviation in terms of linear velocities between predictions and experiments is our implicit assumption of symmetry when calculating the drag force. Our drag coefficients k_T and k_R are independent of the orientation of the MBR. We are currently developing a numerical analysis of the drag force acting on a rectangular plate moving parallel to a surface in a low Reynolds number regime and this may yield an even better match with the data. This analysis would also lead us to estimate the force required to move the microstructures with certain speeds. An alternative method for quantifying the drag coefficients is to apply a known force using an Atomic Force Microscope (AFM) and then measure the corresponding speed of the microstructure. A force sensor could also be used however the sensor needs to be extremely sensitive as the total force applied is in the order of piconewtons.
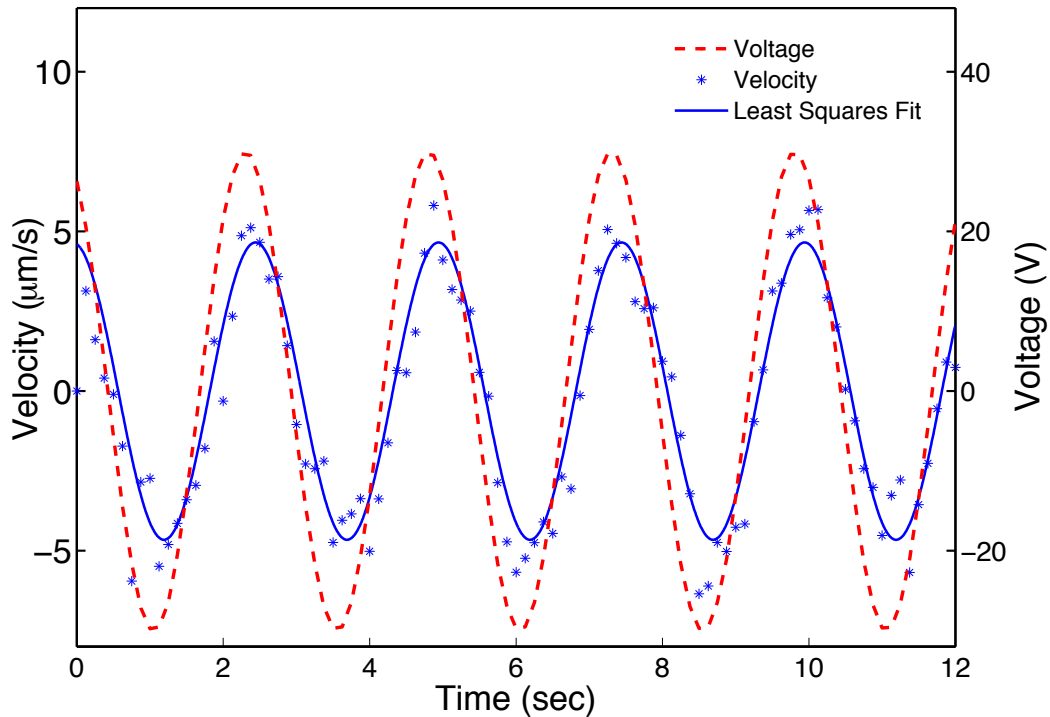
Figure 4.7: The velocity of $20 \times 22 \ \mu\text{m}^2$ rectangular MBR as a response to a sinusoidal input voltage (dashed line) with an amplitude of 30 V and a frequency of 0.4 Hz. A least squares minimization was used to fit a sine curve (solid line) representing the velocity data (*)

4.6   System Characterization

The entire MBR system incorporates several elements that have not been previously characterized in great detail. These elements include the electrokinetic response of groups of cells attached to microfabricated structures, the movement of microscale plates along substrates in fluidic environments, and the electronic response of agar-based galvanotactic control chambers at relatively high switching frequencies.

As such, a system characterization was performed to accomplish several objectives. Primarily, the characterization was performed to understand the overall dynamic response, and in turn, the degree of controllability of the MBR system. Additionally, the characterization

results lend insight to future experimental design. In particular, knowledge of the dynamic response is useful for determining video sampling rates and computational requirements. The characterization is also necessary to test the feasibility of using electrokinetic actuation for applications like microassembly, and to lay groundwork for the optimization of controller design.

To characterize the electrokinetic response of the system, a series of trials were run with a sinusoidal control voltage with amplitude of 30 V. The frequency was varied from 0.05 to 5 Hz in one direction. The MBRs were tracked with subpixel resolution to determine velocity, which is directly related to voltage through the relation for electrophoresis given in (18). As such, the response of the system was determined by using the amplitude of the sinusoidal velocity. Since the self-actuation component of MBR motion causes deviation from the purely electrokinetic component, a least squares minimization was used to fit the sine curves at each frequency (Figure 4.7). The curve fit was applied only after steady state was achieved. The least squares fit routine additionally smooths the noise that is introduced in the tracking algorithm. The tracking noise arises due to fluctuations in light intensity and movements of individual bacteria along the edges of MBRs. The MBR follows the input signal quite well up to a cutoff frequency near 3 Hz, where the magnitude drops off considerably (Figure 4.8). At 3 Hz, the phase lag increases to 2.73 radians.

Due to the dominance of viscous forces at such small length scales, inertial effects would typically be expected to be negligible at the tested frequencies. Thus, other sources for the loss of phase coherence and drop in magnitude should be considered. The electrochemical circuitry of the experimental chamber includes buffer solutions and agar electrodes, and charging effects may play a role in the observed changes in response around 3 Hz.

We do not measure the electrophoretic mobility of the bacteria or the individual robots. Yet, the estimated value of β_4 is good enough to predict the average effect of electric fields
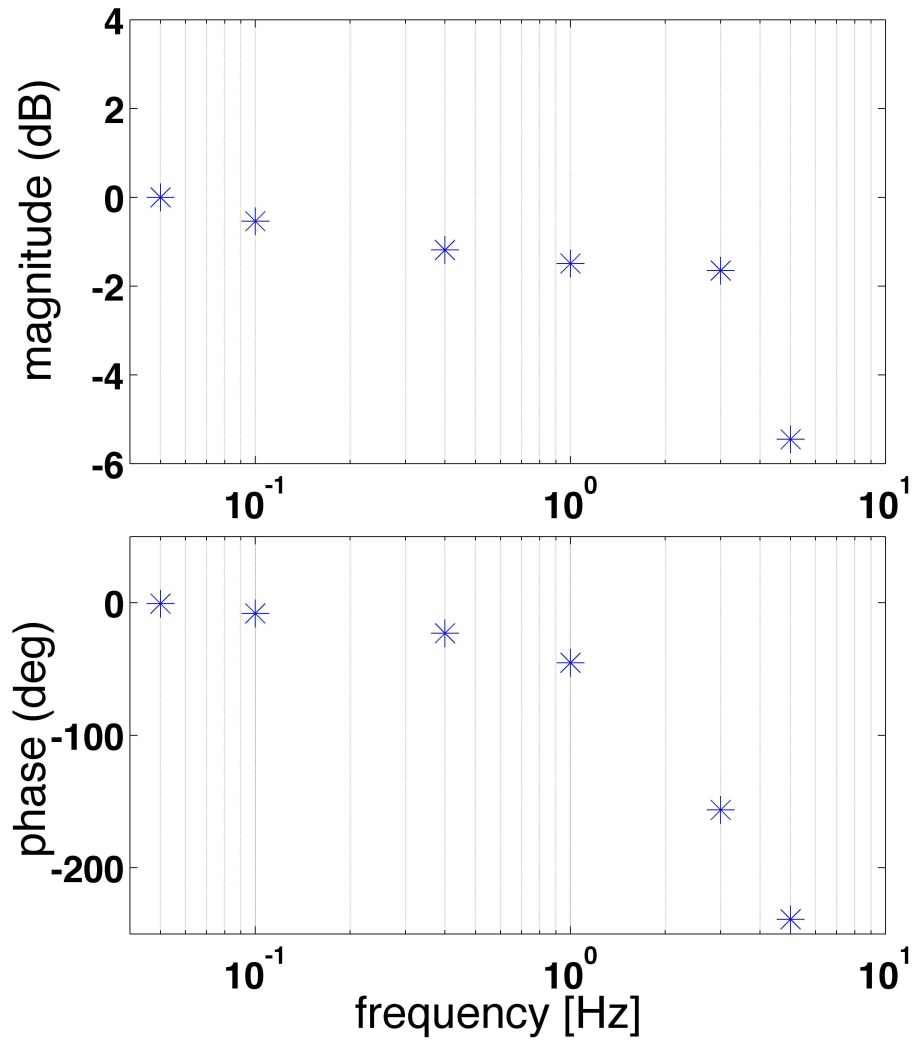
Figure 4.8: Bode plot of the system. The MBR follows the input signal quite well up to a cutoff frequency near 3 Hz, where the magnitude drops off considerably

on the motion of MBRs. By making an on-line measurement of β_4 for each MBR during the steering experiments, a better controller for the electrokinetic actuation can be obtained. The mathematical model can also be incorporated into the control algorithm as a predictive tool to improve the overall accuracy. The current experimental setup does not allow us to control the distribution of the attached bacteria. However, in our future work, we plan to explore different techniques to control the position and orientation of the cells before, during and after attachment. It has been shown that motility of microrobots could be enhanced by selectively patterning cells on specific sites [64].

The control capabilities of the MBRs can be extended by patterning cells on different parts of microstructures. In order to enrich our understanding of electrokinetic and viscous forces acting on our robots, we patterned bacteria on specific parts of the microstructures. By this way, we can further test the accuracy of the predictions of our model. Besides, due to nonuniform distribution of charges, the angular velocity of the MBR will become controllable using electric fields. Here, we present a method of creating motile bacterial carpets of *S. marcescens* on predetermined regions of SU8 microstructures using PDMS sieves and flow deposition. We modified a technique originally used for patterning active proteins on glass substrates [72].

The general concept of patterning *S. marcescens* is illustrated in Figure 4.9. A suspension of bacteria that are collected from the swarm plate is introduced inside microchannels by degassing in a vacuum chamber. PDMS adheres reversibly to SU8 microstructures and the regions covered are protected from cell attachment. The holes were filled with the solution after 2 min. and the bacteria adhere to uncovered parts of microstructures by natural accretion.

In a previous study [73], the authors reported the density of bacterial carpet during a carpet-deposition process on the walls of a PDMS microfluidic channel. According to their results, the flow-deposited carpet asymptotes very slowly towards 100% coverage and af-
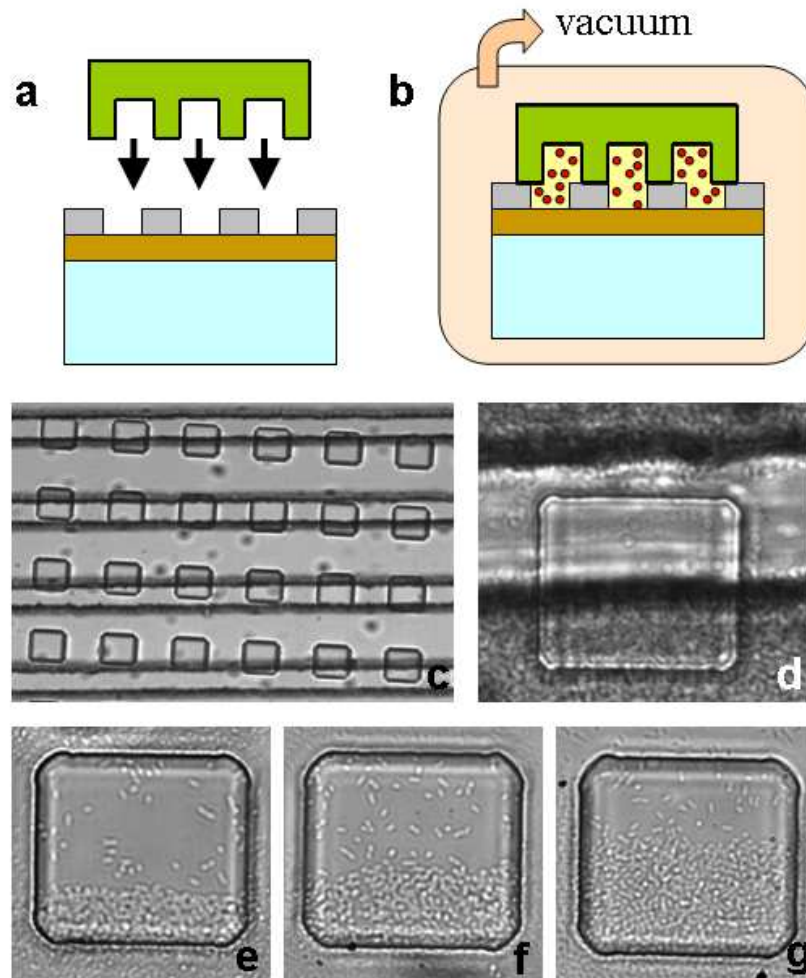
Figure 4.9: Sequence of cell patterning using a PDMS sieve. (a) PDMS sieve is attached to the SU8 microstructures (b) Cell suspension is poured and the solution is degassed in a vacuum chamber. (c)10X phase contrast image of PDMS sieve in contact with microstructures (d) 63X phase contrast image of microchannels filled with bacteria suspension (e)-(g) Bacteria were patterned on different parts of microstructures.

ter approximately 20 min. more than 80% of the surface would be covered by bacteria. After 20 min. we washed out excess bacteria solution with motility buffer and the sieve was peeled off subsequently. Using this method, we successfully patterned bacteria on different parts of microstructures, while the selection of patterned regions can be adjusted by changing the initial design and placement of the sieve (Figure 4.9(e-g)). MBRs with different bacteria patterns were transferred to the electrotaxis chamber for further experimentation. Their movement due to self-coordination of bacteria was observed. We are currently analyzing their movement under various strengths of electric fields.

4.7 Optical Control

Exposure to UV light has been established as a mechanism which affects the motility of bacteria [74]. Since MBRs generally exhibit rotational motion in the absence of external stimuli, use of UV light exposure is an effective means of adjusting angular velocity or completely stopping rotational motion [32]. Several trials were performed by recording the motion of the MBRs upon exposure to UV light until motion ceased. The optical path included a 100 W Hg light source and a 63X PL Fluorotar objective. To capture the unstimulated motion, video was recorded for 10 s before exposing the MBRs to UV light. The orientation of the MBRs was tracked and evaluated in MATLAB using a feature-based tracking algorithm [75]. It was discovered that the general behavior was quite similar between trials, and three distinct regions could summarize motion. Between 0-10 s angular velocity was relatively constant as expected since no stimulus had been applied. After exposing UV light, the rotational motion nearly ceased for 1-2 s before resuming at a somewhat lower angular velocity. It is hypothesized that this temporary cessation may be related to the brief induction of tumbling in the bacteria as the cells adjust to the stimulus [74]. Between 5-45 s after UV exposure, the biomolecular motors driving the flagella

57
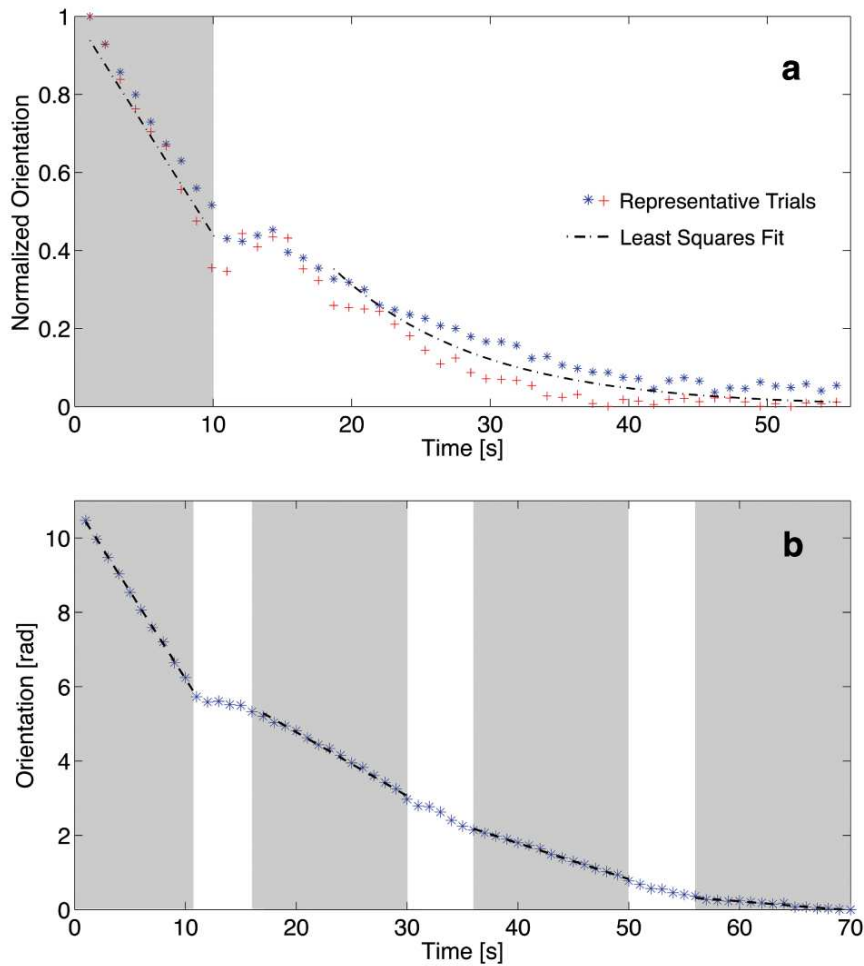
Figure 4.10: Photoexposure characterization. (a) Shown is a representative selection of results from several trials of exposure of MBRs to UV light, as well as a trend lines before and after UV exposure. White regions represent UV exposure. The results of the angular orientation (position) were normalized and averaged to reveal characteristic trends. The final, motionless orientation of the MBRs were normalized as zero radians. Angular rotation is constant before exposure, varies near zero during the few seconds immediately after exposure, and decreases exponentially afterward. (b) When exposing repeatedly, angular speed may be adjusted lower, as reflected by slope of the curve. Angular velocity remains constant when there is no UV exposure, even after several repetitions.

gradually de-energized and the magnitude of the angular velocity of the MBRs decreased exponentially (Figure 4.10). This characterization was used to adjust angular orientation of MBRs for experiments.

Using this initial characterization, MBRs were repeatedly exposed to UV wavelengths to test on/off repeatability (Figure 4.10(b)). Results consistently showed that the cessation of rotation is a phenomenon that occurs during the initial few seconds of the first exposure. Subsequent 5 s exposures after 15 s intervals show a decrease in angular velocity without complete cessation [68].

To determine if photoexposure affects the electrokinetic response of MBRs, we repeated our characterization procedure by applying electric fields (ranging from 1-10 V/cm) to MBRs after deactivating them using UV light. The MBRs demonstrated the same electrophoretic movement as before the exposure, and as expected, the movement due to self-coordination of the bacterial carpet was completely missing. In terms of modeling, the effect of the application of UV light can be simulated by removing the self-actuation portion without changing the electrophoretic forces.

4.8   Discussion

Most of the movement arises from the applied electric field so the motivation for having living cells may seem unclear. As an alternative approach, we coated the surface of SU8 microstructures with a silane that is positively charged due to the linked carboxly groups. However, the microstructures stopped moving as if they lost their charges soon after we started applying electric fields. This could be due to the changes caused by ionic exchange inside the fluidic chamber, which should be investigated further. On the other hand, the bacteria cells preserve their charge throughout the experiment at different electric field strengths, an essential property needed to model and control their motion. Another advan-

tage is that bacteria can be used as on-board biosensors. This option will be explored in the next chapter. Here we showed that our techniques can be used to fabricate, calibrate and transport MBRs in microfluidic channels in a controllable fashion. In the following chapter, we demonstrate micromanipulation and microassembly tasks using our MBRs. We also address the integration of biosensing and bio-actuation onto MBRs.

One shortcoming of the model that may explain the slight deviation in terms of linear velocities between predictions and experiments is our implicit assumption of symmetry when calculating the drag force. Our drag coefficients k_T and k_R are independent of the orientation of the MBR. We are currently developing a detailed analytical model of the drag force acting on a square plate moving parallel to a surface in a low Reynolds number regime and this may yield an even better match with the data. We also do not rigorously control pH, temperature, and impurities in our control chamber and this makes it impossible to measure electrophoretic mobilities precisely. Yet, the estimated value of β_4 is good enough to predict the average effect of electric fields on the motion of MBRs. By making an on-line measurement of β_4 for each MBR during the steering experiments, a more accurate model for the electrokinetic actuation could be obtained. The model can be incorporated into the control algorithm as a predictive tool to improve the overall accuracy.

Chapter 5

Microscale Manipulation, Transport and Biosensing using MBRs

The work in this chapter was first presented in [67, 68, 76] and was done in collaboration with Edward Steager, Agung Julius, Alex van Oudenaarden, Mark Goulian, Albert Sirya-porn, Dalhyung Kim and Min Jun Kim

In the previous chapters, several important experimental techniques for building *MicroBioRobots* (MBRs) are proposed and a theoretical framework for modeling and control of MBRs is presented. In particular, we proposed a method of controlling MBRs using self actuation and DC electric fields, and developed experimentally validated mathematical model for MBRs.

Here we demonstrate experimentally that vision-based feedback control allows a four-electrode experimental device to steer MBRs along arbitrary paths with micrometer precision. At each time instant, the system identifies the current location of the robot, a control algorithm determines the power supply voltages that will move the charged robot from its current location toward its next desired position, and the necessary electric field is then created. Previously described control techniques are applied to orient and steer bacterial
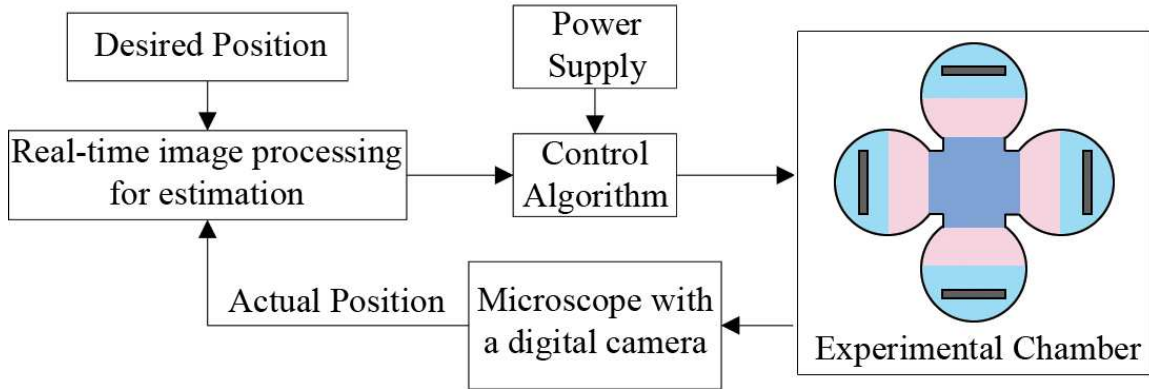
Figure 5.1: Block diagram for vision-based computer control of MBRs. The vision system informs the control algorithm of the current position of the robot. The control algorithm calculates the distance between the current and the desired position and finds the power supply voltages that will create the electric field required to steer the robot towards its next destination.

microbiorobots as well as to transport target loads. Specifically, ultraviolet light is used to control the on/off motion and direct current electric fields are used to control the two-dimensional movement of MBRs.

5.1 Control of MBRs

We employ a vision-based electrokinetic control strategy to steer robots by adjusting the applied voltage at each time step according to where they are and where they should be.

5.1.1 Control Law and Feedback

The basic feedback control steering concept is described in Figure 5.1. Even a simple control algorithm is sufficient to steer our MBRs. The desired goal can be accomplished using one of two approaches.

If the desired trajectory $r^{des}(t)$ is given, then the applied electric field can be adjusted with a simple proportional control law:

$$U = K(r^{des} - r) + \dot{r}^{des} \tag{5.1}$$

where K is a suitable positive constant and $\dot{r}^{des}$ is the feed-forward term. In the presence of *self actuation*, the error $e = r^{des} - r$ cannot be driven to zero. However, the error can be predicted accurately using the mathematical model in (7-11).

We employed an alternative solution in which we fixed the speed of the MBR and only controlled the direction of motion. This time, instead of having the desired trajectory, we define a series of target points. The control law is given by:

$$U = \frac{K(r^{des} - r)}{\|r^{des} - r\|} \tag{5.2}$$

5.1.2   Results

As a demonstration, a star-shaped trajectory was defined by choosing five destination points corresponding to the corners of the star (Figure 5.2). These target locations were fed to the feedback control algorithm that uses the current location of the MBR and the position of the next destination to control the applied voltage. The real-time image processing algorithm processes the captured frames and the control algorithm updates the applied voltages with a frequency of 8 Hz.

The star-shaped trajectory experiment demonstrates a number of capabilities of the MBR system. Firstly, the experiment demonstrates the ability to locate the centroid of the MBR to single pixel resolution (0.5 μm). Additionally, the experiment demonstrates the ability to quickly switch directions and to follow arbitrary slopes with only four electrodes and two amplifiers.

The overall trajectory followed by a a 20×22 μm rectangular MBR is given in Figure 5.2. MBR successfully passed through all the predetermined destination points. The
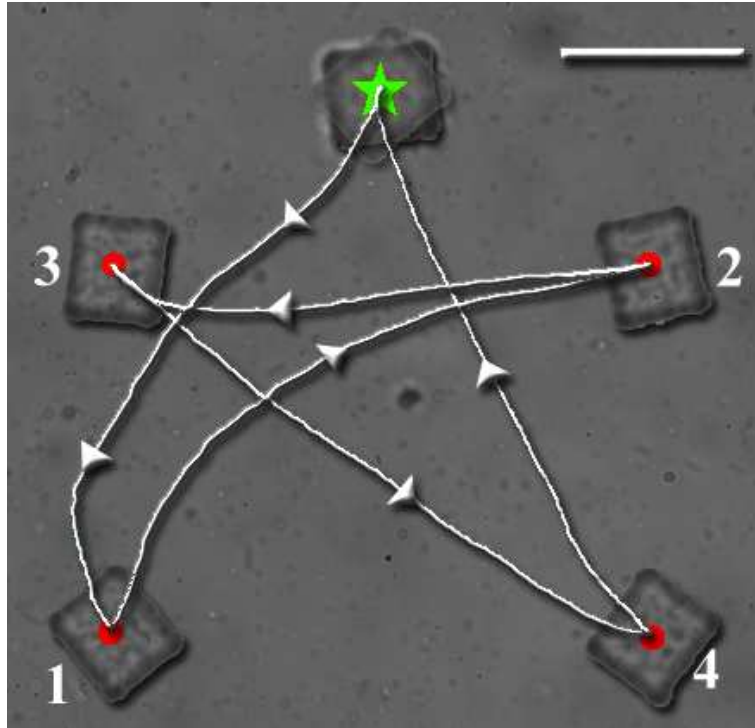
Figure 5.2: Steering of a 20×22 μm rectangular MBR along a star-shaped path. The MBR passes through destinations 1-4 before stopping at its initial position.The scale bar represents $50\mu m$

robot immediately responded to the changes in the applied voltage thanks to the absence of inertia at low Reynolds number and its velocity followed a similar trend with the applied voltage as expected (Figure 5.3).

Before running the control algorithm, $\beta_{1,2,3}$ were estimated as described in Section IV. The values of the parameters were found as $\beta_1 = -0.2\ \mu m/s/pN$, $\beta_2 = 0.65\ \mu m/s/pN$, $\beta_3 = -0.28\ rad/s/pN$, and $\beta_4 = 0.56\ \mu m/s/V/cm$. We imported the voltage input applied during the experiment (see Figure 5.3) to the mathematical model and simulated the response of the MBR described by the estimated parameters. The comparison of the experimental observations with theoretical predictions is shown in Figure 5.4. Even though the control input changes continuously, the predicted trajectory closely resembles the observed one with an average deviation less than 20 μm.

By increasing the number of destinations points, we could be able to decrease the tracking error. A 20×22 μm rectangular MBR successfully followed first a circular and then a diamond shaped trajectory (Figure 5.5).

5.2   Microassembly and Micromanipulation

As a demonstration of the ability to steer MBRs, microscale C-shaped parts that we call goals were fabricated using standard lithography and SU8 photoresist. The goals were released in the control chamber along with square-shaped MBRs measuring 40 μm on each side. By varying the direction of the electric field, the MBRs were easily steered through the entrance of the goals even while continually rotating (Figure 5.6).

It is important to note that the thickness of the C-shaped goal is an important parameter in these experiments. If the structure is much thicker than the MBR, electric field lines will diverge around the goal. The consequence of this divergence is that MBRs in the immediate vicinity of the goal will lose controllability.

65
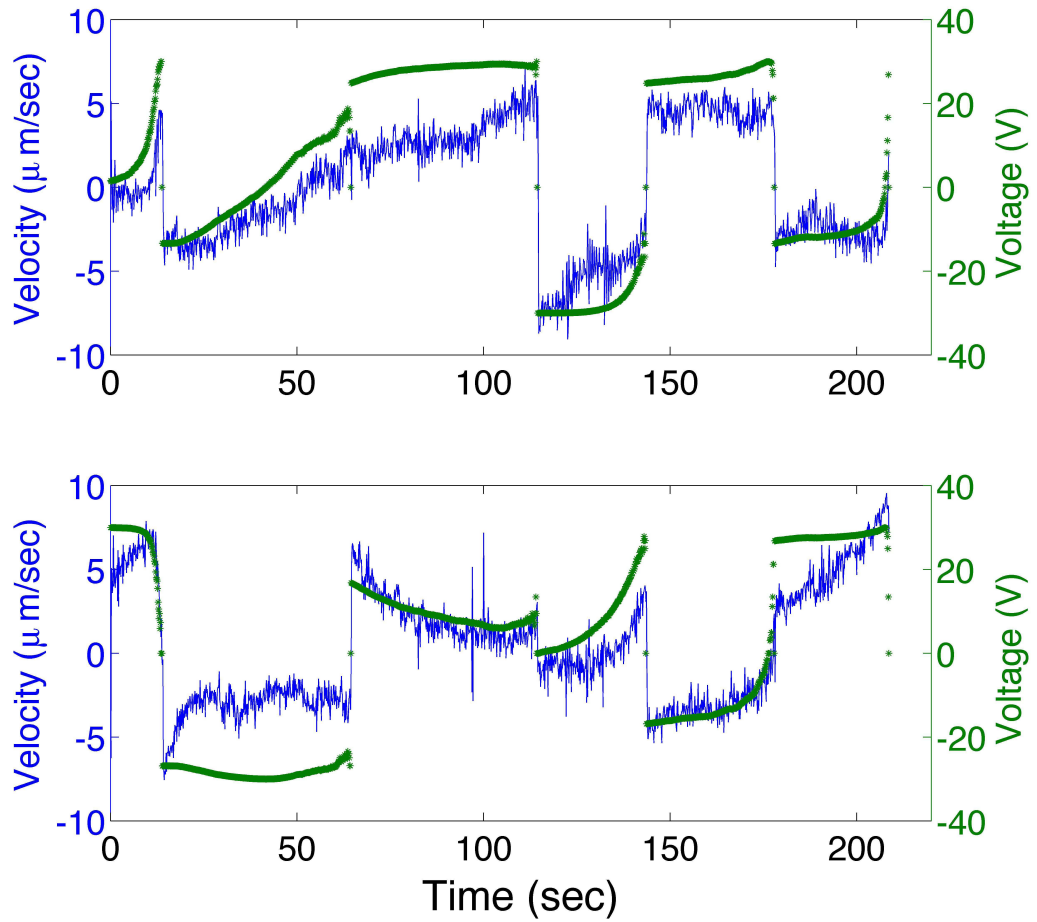
Figure 5.3: The voltage applied to the system and the corresponding velocity of the MBR in x (top) and y (bottom) direction during the experiment. The robot responds to the changes in voltage immediately as expected.
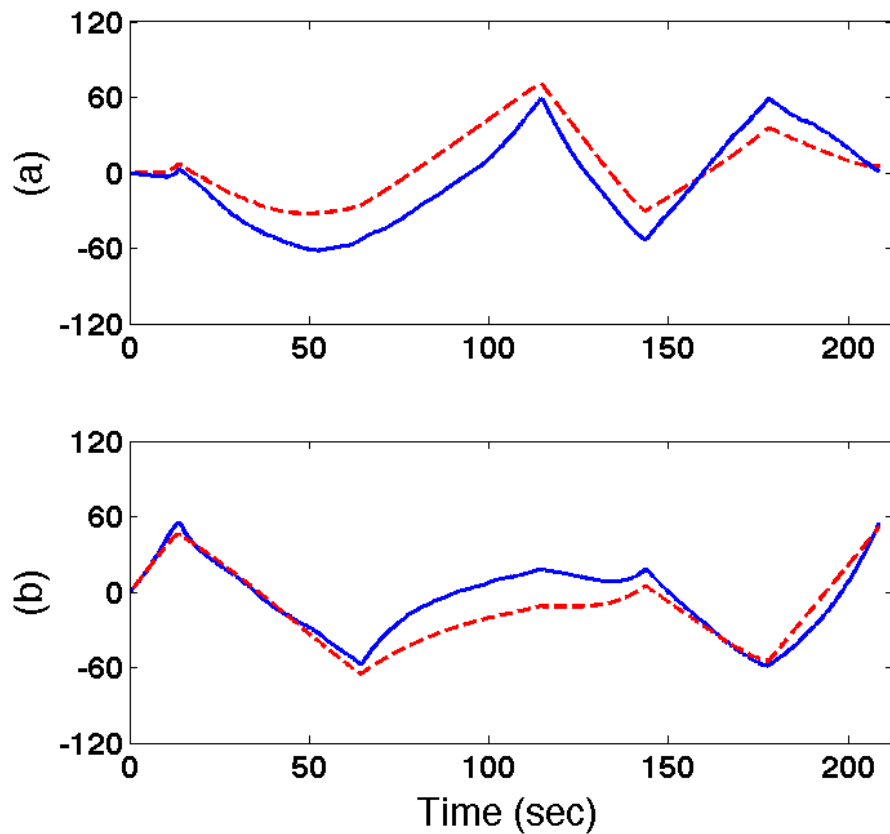
Figure 5.4: The comparison between the experimental data (blue line) and the model prediction (red line) for the star experiment. (a) x in μm, (b) y in μm
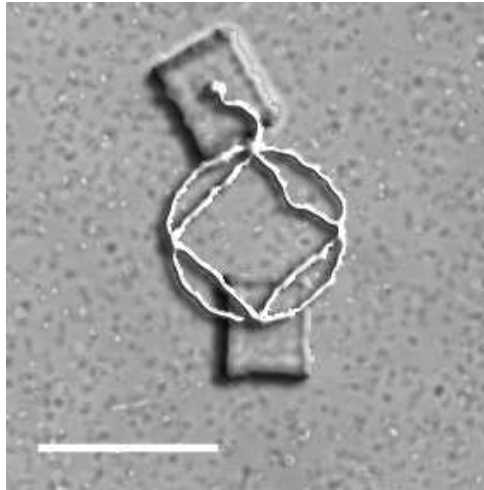
Figure 5.5: Steering of a 20×22 μm rectangular MBR along a circular and a diamond shaped path. The MBR passes through destinations and returns to its original position. The scale bar represents $50\mu m$.
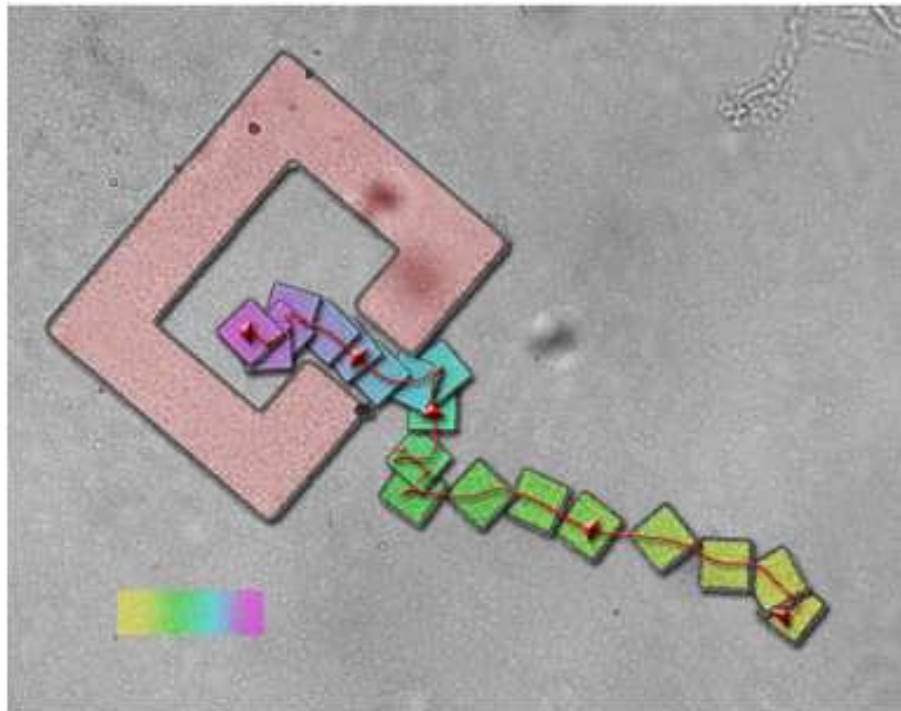
Figure 5.6: An MBR is directed through the entrance of a C-shaped microfabricated goal using tele-operation. Scale bar represents time (2 min) as well as length (100 μm).

Coupling the light and electric field mechanisms together enables control over the angular orientation as well as two-dimensional positioning of the MBR. To demonstrate the combination of control techniques (UV light and EFs), MBRs were used to engage and transport a 10μm cube composed of SU8 epoxy, referred to here as the target. Based on the water-soluble sacrificial release method, several targets were released into the experimental cell. MBR transporters were also released and actively moving in the experimental cell due to self actuation.

An MBR/target pair was selected and a path was planned for the translational and rotational motion. First, the transporter was moved to the vicinity of the target by adjusting the electric field along the two major axes (Figure 5.7). The field employed was roughly 10 V/cm. When the transporter was within 100 μm of the target cube, a dose of UV light was applied to stop the rotational motion of the structure. When the target was engaged, changes in orientation were caused not by propulsion from the flagellar motors, but from reaction forces between the transporter and the target.

Targets were moved several hundred microns by further applying electric fields. Despite the fact that the flagellar motors of the bacteria were disabled, the electric field still moves the transporter and in turn, the target.

Another task was assigned of transporting a cube-shaped target load measuring 10 μm on each side using a U-shaped MBR referred to as a transporter, which was positioned and oriented using a combination of bacterial self actuation, electrokinetics, and phototaxis. A self-rotating transporter was first positioned near the object by varying the direction of the electric field. Next, the transporter was stopped at an appropriate orientation to engage the target using localized UV light exposure. Once the rotational motion was stopped, the transporter was positioned to engage and move the load. The transporter was disengaged and reengaged by switching the polarity of the electric field (Figure 5.8).

These results suggest several potential applications for biological robotic systems. As
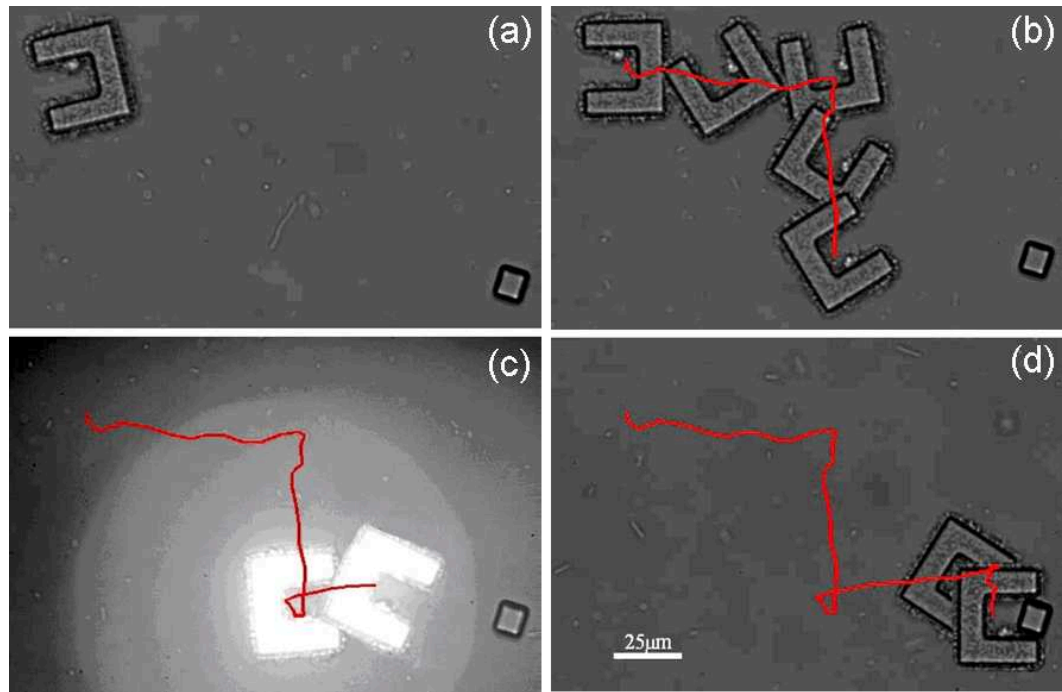
Figure 5.7: Micromanipulation experiment (a) Initial position of U-shaped MBR transporter and target. (b) Transporter is moved to the right and down while rotation continues. (c) Rotation is stopped in proper orientation upon exposure to UV light. (d) Transporter engages the target object.
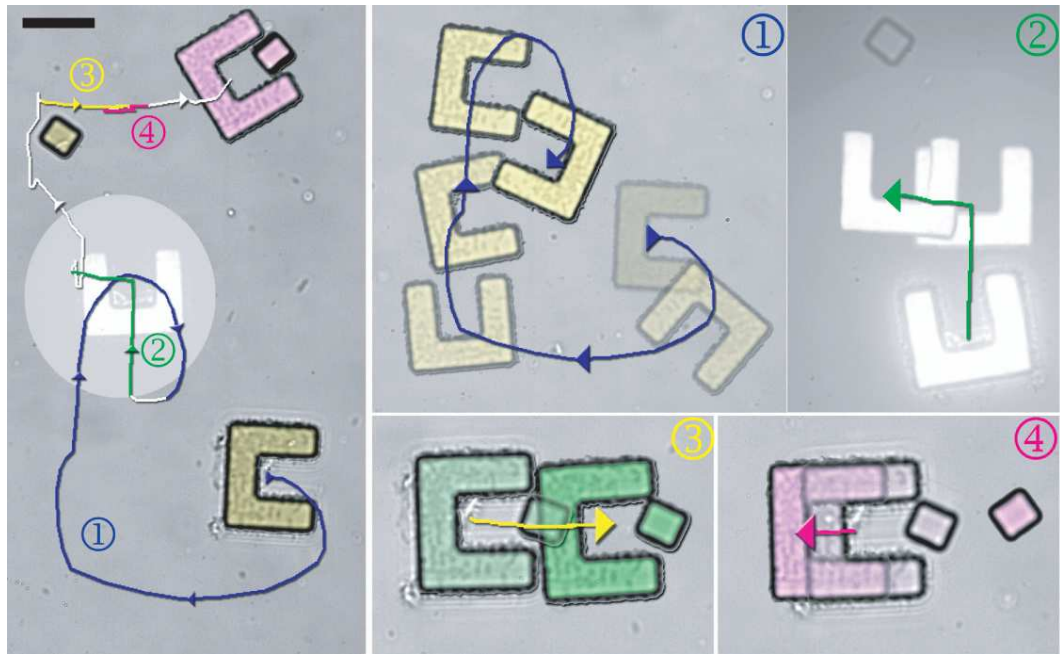
Figure 5.8: At left is shown a summary of the complete path of an MBR transporter moving a target load described in detail in parts A-D. Total time is 2 min, and scale bar is 25 μm. (A) The transporter initially rotates clockwise due to the self-coordination of the bacterial carpet. Electric fields are applied to move the transporter to the left, then up. (B) With the application of UV light, the transporter stops rotating in 6 s. As rotation is stopped, electric fields are applied to position the transporter close to the target. (C) The target is engaged and transported to the right. (D) The target is disengaged/reengaged by switching field polarity.

demonstrated here, transport of microscale or even nanoscale objects is one application area. The dimensions of objects transported in these experiments are similar in scale to many types of living cells. These systems could also be employed for assembly of small microparts.

5.3 Biosensing

Beyond purely mechanical tasks, MBRs may also be employed as mobile biosensors. Autonomous smart microdevices with sensing and information processing capabilities that act as swarms of intelligent sensors have great potential use in drug delivery and single cell analysis. Recent developments in microfabrication techniques and surface chemistry have provided various ways to interface biological and synthetic components and develop a wide variety of biologically integrated engineering systems. The ability to monitor the behavior of these systems in response to biologically relevant chemicals is an important requirement for further development. To take advantage of integrated live cells, they can be genetically modified and employed as sensing elements.

We employed two different approaches for biosensing: motility-based sensing and fluorescent-based sensing. The first method is based on harnessing bacterial power and monitoring their collective motion, and in the second method we use genetically engineered bacteria. Bacteria are easy to culture, relatively insensitive to the details of their environment and can be genetically engineered in order to produce specific marker proteins upon recognition of the target chemicals.

5.3.1 Motility-based sensing

In this approach, we project the 3-dimensional random motility of bacteria into a predictable planar motion of microdevices. We monitor the changes in the motion of the
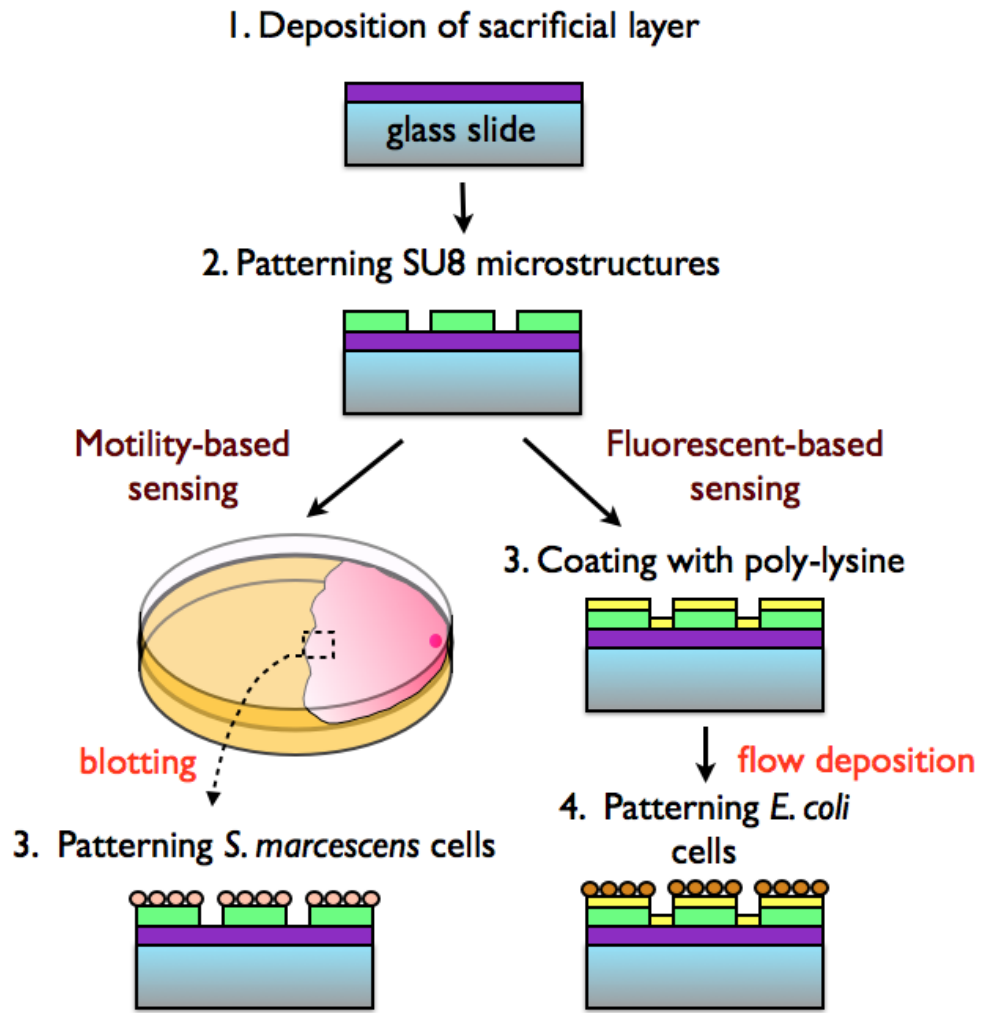
Figure 5.9: Fabrication process of the microdevices for motility-based and fluorescence-based sensing.

devices to detect the presence of target chemicals. In the previous chapters, we blotted plate-like SU8 microstructures with swarmer cells of *Serratia marcescens* and studied their motion. We demonstrated the control of their motion using DC electric fields, and developed a computer control algorithm to steer the microstructures to any position in a planar micro channel using visual feedback from an inverted microscope. In this chapter, we build on these previously developed techniques and demonstrate how changes in motility of bacteria-powered microstructures in the presence of analytes can be used for biosensing using copper ions as an example. It has been shown that copper ions paralyze *S.marcescens* temporarily and in a reversible fashion [64]. Heavy metal ions directly bond to the rotor of the flagellar motor and impair its motion instantaneously. Adding chelating agents eliminates this effect as they form chemical bonds with metal ions.

The synthetic component of the device is fabricated out of SU8, which is biocompatible, patternable in a wide range of shapes and thicknesses, and is only slightly denser than the working fluid. The microfabrication and development procedure is compatible with a technique of release using a water-soluble sacrificial dextran layer. Traditional techniques for release of structures using a sacrificial layer have required toxic chemicals. Using dextran for the release layer, the motility medium in which the studies are performed acted as an agent of release. The fabrication sequence is shown in Figure 5.9.

The bacteria *Serratia marcescens* were cultured using a swarm plate technique (Luria-Bertani medium (Sigma) containing 0.6% Difco Bacto-agar (Sigma) and 5 g/l glucose). Cells were attached by blotting microstructures directly along the active swarm edge, generally covering more than 90% of the surface. The swarmer cells of S. marcescens stick to the surface of the microstructures naturally. Thanks to the water-soluble sacrificial dextran layer, hundreds of sensors were released into the observation chamber filled with motility buffer (0.067 M sodium chloride, 10^{-4} M ethylenediaminetetraacetic acid (EDTA), and 0.002% Tween-20, pH 7.0) without causing any structural damage. The sensors were free

to move inside the fluid, and their movement due to bacterial actuation was immediately observed.

We ran several experiments where we added different concentrations of $CuSO_4$ into the solution and the lowest copper ion concentration that our devices can detect was found as 10 μM. The steady-state angular velocity of the devices decreases as the concentration of copper ions is increased from 10 μM to 100 μM. For concentration values higher than 100 μM, all the devices stop rotating. The sensors stopped moving immediately as expected[9] and they started moving again with the addition of the chelating agent. For the given concentration levels, exposure to copper does not damage the bacteria and the process can be repeated multiple times. As the sensors stay on the same focal plane throughout the experiment, their motion can be recorded at all times.

Next, to demonstrate the ability to sense chemicals while scanning the whole observation chamber with the devices, we designed a simple setup where we apply electric fields in one dimension using a copper and a platinum electrode (Fig. 2a). We previously showed that[12] the expected velocity of the sensor is given by

$$Ev_x = \beta_1\bar{p} + \beta_4 U_x \tag{5.3}$$

$$Ev_y = \beta_2\bar{p} + \beta_4 U_y \tag{5.4}$$

$$E\omega = \beta_3\bar{p} \tag{5.5}$$

where $E(\cdot)$ denotes expectation, v_x and v_y are the components of the translational velocities, ω is the angular velocity, $\bar{p}$ is the expected value of the force applied by each bacterium and U is the electric field with components U_x and U_y. The parameters $\beta_{1,2,3}$ summarize the distribution of the bacteria on the sensor, and $\beta4$ is a parameter related to the charge of the bacteria. Because the whole surface of the device is coated with a monolayer of bacteria that is approximately uniformly random, the moments due to the applied

electric field is close to zero (Figure 5.10(a)). The equations (1)-(3) summarize the fundamental physics of the system and show that the motion of the devices is predictable and the angular velocity of the devices is fully dependent on bacterial actuation. As a result, any significant change in the angular velocity will be understood as a change in the motility of attached bacteria, which points to the existence of the inducer.

Positively charged copper ions released from the anode migrated towards the negative electrode while negatively charged sensors were moving in the opposite direction. Anode can be taken as an infinite source of copper for our experiments so charged copper ions are transported by both diffusion and electrophoresis. When sensors encountered the copper ions, their motion due to bacterial actuation stopped immediately as the attached bacteria were paralyzed (Figure 5.10(b)). The angular velocity became almost zero accordingly, as the main source of rotational motion of the sensors is flagellar propulsion (Figure 5.10(c)). The translational motion of the devices was slightly affected from copper. The contribution of the bacterial actuation to the translational velocity of the devices is small compared to their electrokinetic mobility. Starting from the sensor closest to the positive electrode, all the sensors inside the observation chamber stopped rotating one by one. We verified once again that the observed phenomenon was due to the released copper ions, by adding 0.01 M potassium phosphate into the solution. Potassium phosphate precipitates with copper and forms a visible compound. Heavy metal ions directly bond to the flagellar motor without initiating biochemical signals, but the method applied here can be extended to scenarios where chemical agents interact with chemoreceptors. Sensing capabilities of attached bacteria can also be extended by genetically engineering motility as a phenotypic response to other external stimuli.
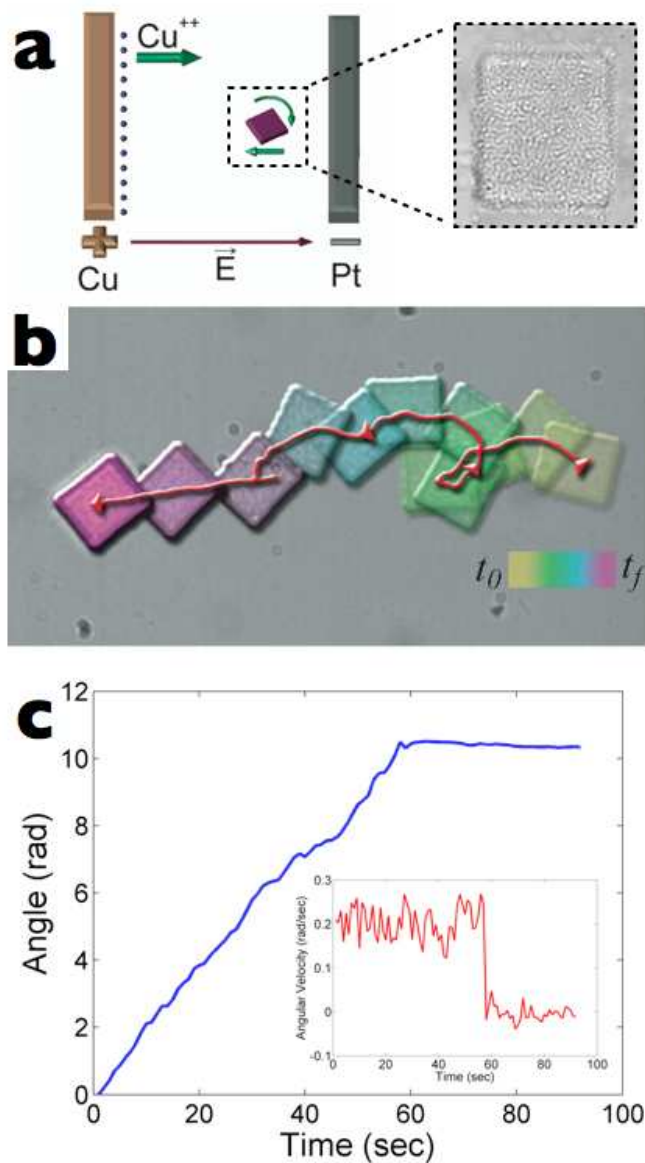
Figure 5.10: Motility-based sensing. (a) Schematic of the setup used for the copper sensing experiment. (b) Sensing of copper ions is observed as a loss of rotation. The translational movement due to applied electric field persists. (c) Angular position and velocity vs time. Fluctuations in angular velocity are caused by the torque applied by the electric field. Scale bar represents time (100 sec) as well as length (50 μm).

5.3.2 Fluorescence-based sensing

Geneticallt engineered strains are kindly supported by Alex van Oudenaarden and Mark Goulian

In this approach, we use a fluorescent reporter system to monitor the state of signaling networks in single cells to infer the presence of analytes like copper. The use of laminar flow of liquids in microfluidic channels to perform patterned cell deposition was described before [77]. We combined this method with our procedure of fabricating microstructures and a surface treatment to pattern genetically engineered *Escherichia coli* cells on SU8 microstructures. The planar geometry and transparentness of the SU8 microstructures make them suitable for fluorescence imaging and bioluminescence measurements.

We chose *E. coli* for our sensor as numerous studies have described genetically modified *E. coli* strains in which an input signal elicits an output response linked to a change in gene expression. Previous work showed that copper induces transcription of cpxP, which is under the control of CpxA/CpxR system18, 19. CpxA/CpxR is a typical two-component signal transduction system that responds to envelope stress. CpxA, the inner-membrane protein, phosphorylates its conserved histidine residue in response to signals and then transphosphorylates the conserved asparate residue in CpxR. Activated CpxR, the phosphorylated form (pCpxR), activates transcription of a set of genes including cpxP. The gene encoding for the fluorescent protein GFP under the control of the cpxP promoter was integrated in the chromosome at the α phage attachment site to produce the strain AFS267.120.

Unlike *S. marcescens*, a special surface treatment is needed order to attach *E. coli* cells to SU8 microstructures. Microstructures were coated with poly-L-lysine by immersion of the glass substrate into a freshly prepared solution containing 5.6 ml DI water, 0.7ml poly-L-lysine (Sigma P-8920, 0.1% solution) and 0.7ml PBS for 1 hour. Microfluidic devices were manufactured in polydimethylsiloxane (PDMS) by using soft lithographic techniques. The microchannel was 5 mm long, 1 mm wide, and 50 μm deep. The fabricated PDMS

mold was brought into conformal contact with a 43×50 mm glass slide on which the microstructures were patterned and the assembly was heated on top of a hot plate at $80\,°C$ for 2 hours to form a reversible bond. Microstructures were fabricated in such a way that they could be trapped inside the microfluidic channel (Figure 5.11(a)). E. coli cells were grown at $37\,°C$ with aeration in LB broth. Bacterial cultures were centrifuged and cells were resuspended in LB medium at a final concentration around 10^{10} cells per mL before they were injected into microfluidic channels.

The channel was filled with a suspension of cells by a passive pumping method [78]. Briefly, a large drop of fluid is placed over the outlet or the reservoir port of the microchannel. A much smaller drop of cell suspension is placed on the inlet or the pumping port. Due to the difference in pressure, the solution flows towards the outlet and fills the channel. In this method, there is no need for expensive or complicated external equipments such as mechanical or electroosmotic pumps. Cells adsorbed nonspecifically to the regions of the surface over which the solutions containing them flowed. Cells that did not adhere strongly were washed away with phosphate buffered saline (PBS). PDMS mold was peeled off and microdevices were transferred to an observation chamber.

To get a measure of background fluorescence for our assembly, fluorescent images of devices were acquired. We could not detect a significant level of induction in the absence of copper compared to the copper-induced state. It has been shown that the transcription of Cpx-regulated genes in E.coli reaches its maximum level under $CuSO_4$ induction at a concentration of 0.5 mM. We added 0.5mM $CuSO_4$ to our observation chamber and waited for 30 min to give enough time for the translation of GFP. Finally, fluorescent microscopy was used to visualize induced E.coli cells (Figure 5.11(b)).
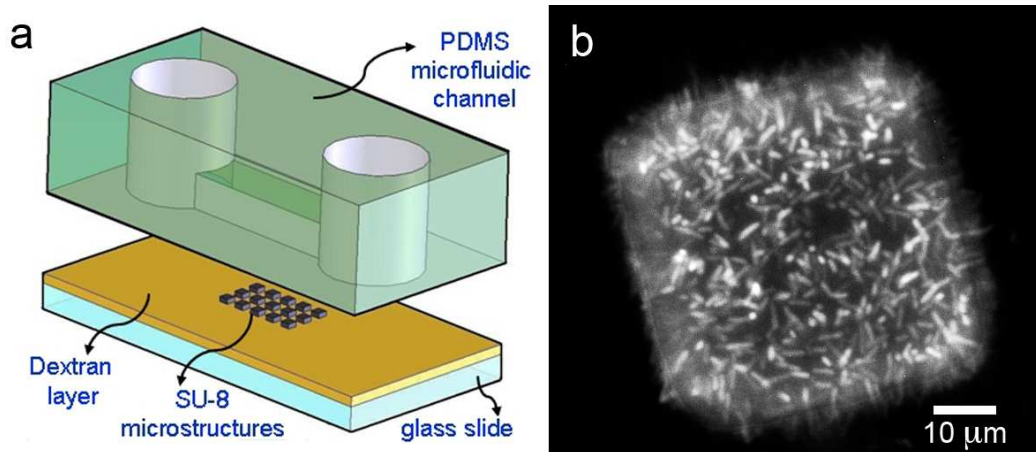
Figure 5.11: Fluorescence-based sensing. (a) Schematic description of the setup. Microstructures were patterned in the center of the glass slide so that they could be trapped inside the PDMS microchannel. (b) Fluorescence image visualizing GFP proteins produced by induced E.coli cells. The scale bar is 100 μm.

5.3.3   Stochastic Modeling of Lactose Sensing with Bacteria

In this section, we describe a novel approach to use "on-board" sensing to steer the MBRs to chemically or biologically relevant goals. In order to do this, we employ two different sets of bacterial cells. The first set of bacteria are *S. marcescens* that control the motion of the MBR as before. The second set of bacteria are genetically engineered *E. coli* that act as biosensors. In other words, we combined motility-based sensing and fluorescent-based sensing by attaching both *S. marcescens* and *E. coli* cells on the same microstructure [76].

Lactose metabolism is controlled by the lac operon, which consists of the lacZ, lacY, and lacA genes encoding b-galactosidase, lactose permease (lacY), and acetyltransferase, respectively (Figure 5.12). Acetyltransferase is involved in sugar metabolism. Permease facilitates the influx of lactose and nonmetabolizable lactose analog TMG from the exterior which results in positive feedback on the permease expression level. The bistability arises from this positive feedback. The lac genes are fully expressed for every cell in a population under high extracellular concentrations of TMG while at moderate inducer concentrations,
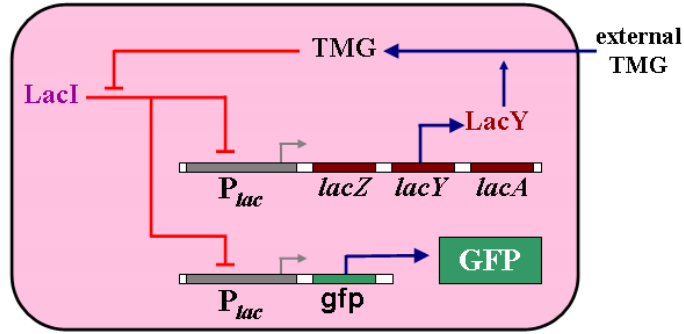
Figure 5.12: Diagram of the lactose utilization network. The fluorescent reporter GFP integrated in the genome is expressed in parallel with LacY under control of the lac promoter and reports the induction level of the cell [1].

the lac genes are highly expressed in only a fraction of a population (Figure 5.13). The population heterogeneity was interpreted by Novick and Weiner as a result of the bistability of the gene expression mechanism of individual cells combined with stochastic fluctuations inherent to biomolecular processes involving few molecules [79]. A recent study showed that a stochastic single-molecule event triggers this phenotype switching [80].

Oudenaarden and his colleagues incorporated a single copy of the green fluorescent protein gene (gfp) under the control of the lac promoter into the chromosome of E. coli (Figure refch5:lac). The details of the construction of this strain is given in [81]. In this study, we employed the same strain as biosensors carried by our MBRs and show that GFP expression can be used as a readout of bacterial activity.

In our previous work, we developed a hybrid stochastic model for the system [57]. The model was based on the idea that the messenger RNA (M) and the β-galactosidase (B) are expressed as molecule counts that evolve following some Poisson processes, while the other substances, internal TMG (T_t) and permease (P), are expressed as chemical concentrations that evolve following deterministic ODE. The reason behind this idea is that a fully stochastic model is computationally expensive, while a hybrid model already demonstrates the stochastic noise that is lacking in the deterministic model.
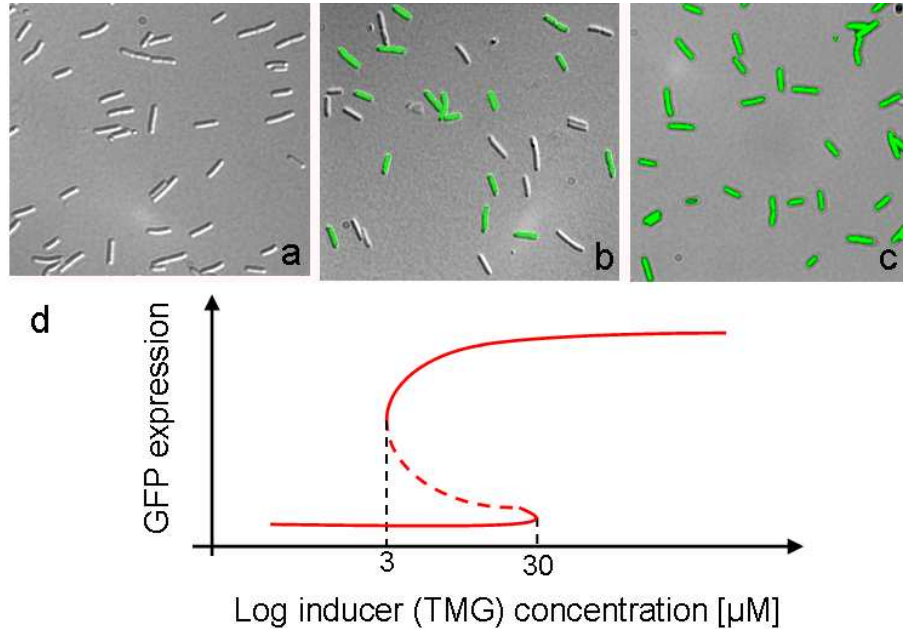
Figure 5.13: Overlayed green fluorescence and inverted phase-contrast images of cells that are initially uninduced for lac expression, then grown for 20 h in a solution with (a) no TMG (b) 10 μM TMG (c) 100 μM TMG (d) Steady-state solutions of the system. The induced state is shown as the upper dark line whereas the uninduced state is shown as the lower dark line. The intermediate unstable steady state is shown as a dashed line.

Here, we describe our fabrication technique and the culturing method that allows us to create monolayers with two different type of bacterial cells on our MBRs.

Bacterial strains, growth conditions and media

The Green Fluorescent Protein (GFP) gene under the control of the wild-type lac promoter was inserted into the chromosome of *E. coli* by van Oudenaarden and co-workers to produce the strain we used in our experiments. The details of the transformation is explained in [81]. *E.coli* cells were grown at 37°C in M9 minimal medium with succinate as the main carbon source. To obtain the fluorescence images of bacteria (Figure 5.13 a-c), cells were grown overnight in the absence of TMG. Afterwards, cells were transferred from this initial culture into media containing specified amounts of TMG (0 μM, 10 μM and 100

82

μM). The microscope slides with agarose pads were prepared using the protocol described in [82]. These pads press the cells against the surface of a cover glass and force the cells onto a single plane. Immobilization ensures that the cells do not move between subsequent measurements of the same group of cells.

The bacteria *Serratia marcescens* are cultured using a swarm plate technique as described in [22]. Cells were transferred into microfluidic channels by pipetting 500 μl of motility buffer (0.01 M potassium phosphate, 0.067 M sodium chloride, 10-4 M ethylenediaminetetraacetic acid, and 0.002% Tween-20, pH 7.0) onto the leading edge of the swarm plate and pipetting back. For the experiments in which electric fields were applied to MBRs, bacteria were attached by blotting microstructures directly along the active swarm edge.

Cell Patterning

The use of laminar flow of liquids in capillary systems to perform patterned cell deposition was described before [77]. We combined their method with our procedure of fabricating microstructures and a surface treatment described elsewhere [83] to pattern two different types of bacteria on SU8 microstructures. These constructs are employed as mobile biosensors.

Microstructures were fabricated in such a way that they could be trapped inside our PDMS microchannel. They were silanized as described in Materials and Methods. After sealing the PDMS mold against the glass slide, the microchannel was initially filled with a suspension of *E.coli* cells for 10 min. Cells adsorbed nonspecifically to the regions of the surface over which the solutions containing them flowed. Cells that did not adhere strongly were washed away with PBS (3-min wash) and the remaining adherent cells were visualized using phase contrast microscopy (Figure 5.14a). The microchannel was then filled with a suspension of *S. marcescens* harvested from the swarm plate (see Materials
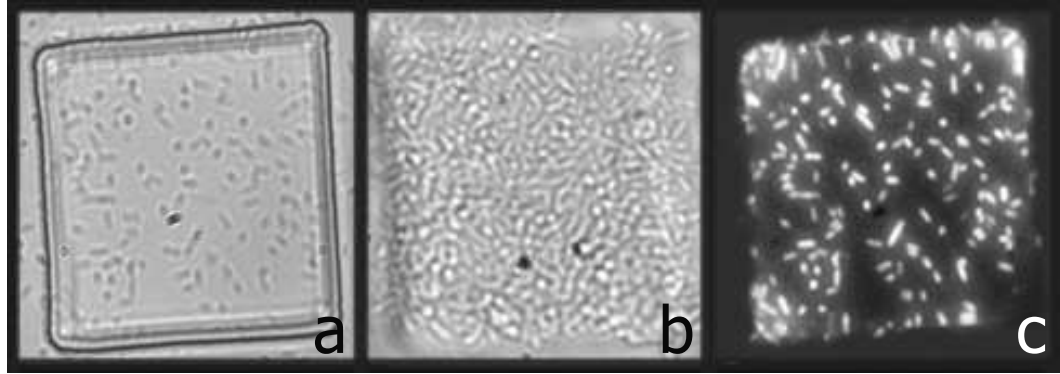
Figure 5.14: (a) Phase contrast image of the microstructure showing the attached *E.coli* cells (b) Phase contrast image of a monolayer of the mixed population. *S. Marcescens* cells fill all the gaps on the microstructure. (c) Fluorescence image visualized only *E.coli* cells as they express GFP while *Serratia* cells do not.

and Methods) for 5 min followed by a 3-min PBS wash. Once again cells were visualized using phase contrast imaging (Figure 5.14b). With the attachment of *S. marcescens*, the microstructures started to move immediately due to self-coordination of bacterial flagella. Finally, fluorescent microscopy is used to visualize induced *E.coli* cells (Figure 5.14c).

In summary, as shown in Figure 5.14, we are able to pattern two distinct monolayers of bacteria. One set of bacteria are responsible for actuation. The other set of bacteria can sense chemicals in the environment and fluorescent microscopy is used to estimate the chemical concentration in the environment. This immediately points to the feasibility of using estimates of GFP activity combined with electrokinetic actuation and ultraviolet radiation to steer MBRs toward biochemical sources.

5.3.4 Discussion

The experimental framework that we develop in this paper is meant as a model system for other biological systems. We can extend our approach to use on-board sensing combined with electrokinetic actuation to steer the MBRs to chemically or biologically relevant goals.

With minimal fluid disturbance, using MBR biosensors in this fashion we can monitor signals in close proximity to target cells. However, the relation between external concentration of analyte and the number of induced cells attached to the MBR should be experimentally quantified. This calibration step is essential to be able to use our biosensor in real-time applications. It is possible to generate spatially and temporally constant gradients extending over millimeters and to maintain their shapes over long periods of time using microfluidics [84].

While monitoring the local environment of target cells, we can simultaneously apply forces with the same microrobots. With appropriate genetic engineering, chemical signals could be generated to influence target cells. This technique may enable MBR-MBR communication by using genetically programmed sender and receiver cells [85].

Chapter 6

Single Cell Manipulation using Magnetic micro transporters and Microgels

The work in this chapter was first presented in [35, 86] and was done in collaboration with Edward Steager, Dalhyung Kim, Min Jun Kim, Sean Kim and Anthony Cowley; see individual sections for the division of work.

6.1   Introduction

As the length scales of robotic systems continue to decrease, one of the clear emerging applications is the manipulation of single biological cells in fluid environments. Single-cell manipulation has traditionally been achieved with pipettes, optical tweezers, or specialized microfluidic channel designs [34]. Recently, a variety of techniques have been explored for the wireless control of microrobots. While some of these methods directly integrate motile microorganisms into the design [30–32], other bioinspired methods rely on controlling applied magnetic forces [7, 87]. Magnetic control of microrobots and microgrippers has also been established as an effective means of microobject manipulation [15, 35–37]. However,

significant challenges remain for applications relating to single cell manipulation mainly due to appropriate scaling of robot size and geometry of existing designs.

To define the appropriate design constraints for robotic single cell manipulation, it is assumed that the most appropriate workspace is on the stage of existing inverted or upright light microscopes. Such microscopes are ubiquitous in life science research laboratories, and include essential capabilities such as phase contrast and fluorescence microscopy. Therefore, the integration of the full design necessarily includes not only an appropriate robot design, but also a compact controller that is compatible with the stage of existing microscopes. By integrating the design into existing microscopes, imaging capture capabilities of the microscopes may also be harnessed.

One of the most important length scales to consider for the system is the workspace for the robot. When working with single cells, fine details of individual cells must be resolved. It is essential to have microstructures with sizes in the same order of target cells in order to transport and position them with some precision. The mammalian cell is an entity with typical dimensions of tens of microns. This requires a magnification of at least 40X. The workspace is then 150 μm $\times$ 150 μm. Based on this, it becomes clear that the robot must not only be small relative to the workspace, but also that precise control of movement is much more important than high speed. In fact, rapid movements may cause significant disturbances to the microenvironment.

Biocompatibility is another essential consideration for the design of a microrobotic cell manipulator. For experiments with living cells, the idea of biocompatibility must be extended from the basic concept of not causing injury to cells to not influencing the behavior of cells due to the chemical composition of the robot. Furthermore, the biocompatibility of the overall design should include any chemicals released in the process of introducing the robot to the cellular microenvironment.

Robotic manipulators on the scale of cells themselves offers significant potential ben-

efits beyond simply moving cells. Wirelessly controlled (*i.e.* untethered) cell-sized robots are highly noninvasive. At this length scale, where viscous fluid forces dominate inertial forces, motile microrobots cause very little mixing or agitation of the surrounding environment. This is a significant advantage over suction pipetting for life scientists, since pipettes cause relatively large fluid disturbances. Traditionally, the focus of robotic manipulators has been centered on applying mechanical forces. However, on the scale of individual cells, the understanding of the word manipulation itself must be expanded to include chemical manipulation of local microenvironments. To a great extent, research in single cell life sciences is concerned with biochemistry. Due to this, a system for the delivery of chemicals in the microenvironment would also greatly enhance the potential of a microrobotic system.

In this work, we develop a microrobot using microfabrication technologies using electromagnetic actuation with visual feedback to meet these challenges. The robot, which is only slightly larger than the rat hippocampal neurons which we are interested in manipulating, has been designed to work on a scale appropriate for the working space of a standard optical microscope. It is aligned by magnetic fields and pulled by field gradients. An oscillating out-of-plane magnetic field induces a stick/slip mechanism that enhances control of the robot [38]. This is useful not only for adjusting the velocity of the robot [35], but also for traversing irregular microscale topographies such as surfaces densely patterned with adherent cells. Composed of iron oxide nanoparticles embedded in a polymer, the robot is fully biocompatible and is patterned using a single-mask photolithographic process. The robot is similar in density to the working fluid. Thus, very small magnetic forces are required for movement. Furthermore, due to the sub-micron resolution of the photolithographic micromachining process, the robot's shape can be tailored to and scaled appropriately for geometric compatibility with different cell types. Release in the microenvironment is enabled by a biocompatible, water-soluble etch process.

A five-coiled magnetic controller was designed for rapid integration with existing mi-

Figure 6.1: Electromagnetic coils mounted on an optical microscope to actuate the micro transporters.

croscopes. This is essential due to the fact that many features of single cells are nearly indistinguishable without the aid of phase contrast or fluorescence microscopy. Visual servoing was incorporated for either teleoperation or fully automated manipulation, and was demonstrated using latex microbeads and rat hippocampal neurons.

Finally, we present results on the integration of microscale hydrogels designed for the localized delivery of chemicals using the microrobot. Hydrogels have been established as an effective means of encapsulating and delivering drugs, and their design may be specifically tailored for customized time-based release [39] or even release in response to environmental triggers such as pH and temperature [40]. The gels are capable of creating localized complex gradients and transporting drugs or chemicals to specific positions of target cells.

6.2 Experimental Setup and Fabrication of Magnetic micro transporters

The experimental setup consists of four identical in-plane electromagnetic coils with diameter 3.5 cm placed 3.5 cm away from each other and one out-of-plane electromagnetic coil with diameter 8 cm. The coils are integrated with an aluminum frame that allows experimentation with both inverted and upright microscopes. The coils are independently driven with H-bridge motor drivers and current control electronics. Imaging is performed on a Nikon inverted microscope using phase contrast. Videos are captured using a ccd camera. Fluorescent images of microgels were taken under a Zeiss microscope supported with a 100 W mercury lamp and filter sets.

In our previous work, we developed a single step fabrication process for biocompatible magnetic micro transporters that did not require subsequent lithography or etching processes [35]. We fabricated the microstructures on glass slides using a ferromagnetic photoresist. The composite photoresist was prepared by mixing iron oxide powder (spherical, 50 nm in diameter, Alfa Aesar, IL, USA) with SU8-10 photoresist (MicroChem, MA, USA) in a glass Petri dish until it yielded a homogenous suspension. Although magnetite nanoparticles are opaque, standard lithography still works as reflection, scattering and diffraction of light from the particles assist in the proper exposure of the photoresist [88].

In this work, we build on our previous work [35] making several improvements. First, we describe changes to the fabrication process that enables a reduction in the size of the microrobots. Second, we are able to increase throughput of the microfabrication process. Third, our process enables robots that are free of excess iron oxide particles that can be seen in the micrographs in [35]. The fabrication sequence is shown in Figure 6.2. The first spin-coating procedure is used to prepare the non-toxic water-soluble sacrificial dextran layer [89]. We need this layer to release microstructures into the fluidic chamber without causing
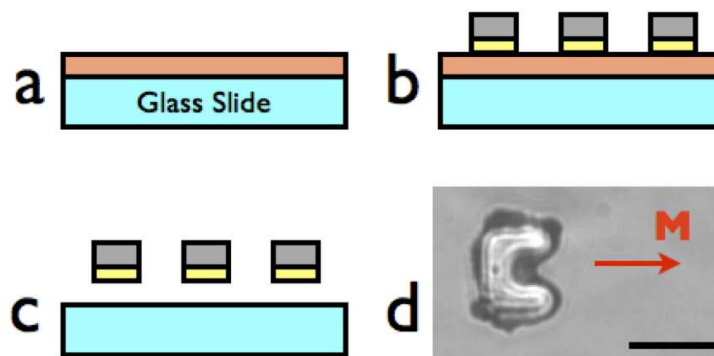
Figure 6.2: Single step microfabrication of large numbers of biocompatible microrobots. (a) The glass slide is fcoated with Dextran. (b) First pure SU8 layer and then ferromagnetic composite SU8 layer are spin coated onto the sacrificial dextran layer. Microrotransporters are magnetized with a permanent magnet. (c) Photoresist is developed and micro transporters are released into experimental chamber. (d) Phase-contrast image of $30 \times 30 \times 10$ μm^3 U-shaped micro transporters. Scale bar is 30 μm

any structural damage. Compared to our previous protocol, we increase the concentration of dextran 50-70 kDa from 5% (w/v) to 10% (w/v) and decrease the spin coating speed from 2000 rpm to 1000 rpm to obtain a thicker and more resistant sacrificial layer. Next, a thin layer (2 μm) of pure SU8-2 is spin coated. This extra layer ensures better release of micro transporters and helps to obtain a more uniform coating of composite polymer in the following step. Finally, the composite ferromagnetic photoresist is spin coated and the exposed substrate is post-baked and developed in Propylene Glycol Monomethyl Ether Acetate (PGMEA). We optimize our fabrication procedure for a specific weight ratio (5% by weight) and photoresist thickness (10 μm) and fabricate $30 \times 30 \times 10$ μm^3 U-shaped micro transporters.

We magnetize our microtransorters using a rectangular neodymium-iron-boron (Nd-FeB) magnet with a surface field of 6450 Gauss (K&J Magnetics, Jamison, PA) in the direction of the opening of the U shape so that the magnetization vector points towards that direction.They are released on a glass slide by bringing the chip with patterned microstruc-
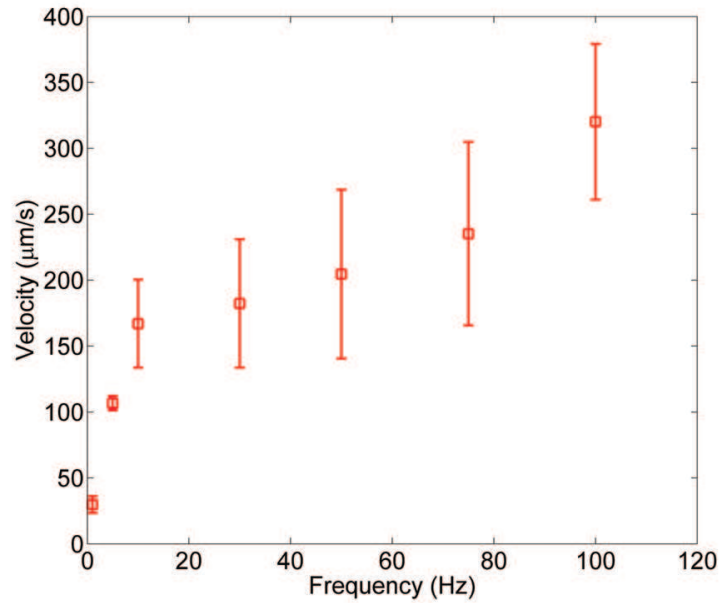
Figure 6.3: Micro transporter velocity as a function of pulsing frequency. Each data point represents five measurements and error bars indicate one standard error.

tures into contact with DI water. They can also be trapped under a closed microfluidic channel and released by filling the channel with water [76].

6.3 Motion Control and Visual Tracking

6.3.1 Motion Control

The robot motion is a stick-slip motion similar to the phenomenon reported in [13]. By applying a time-varying magnetic field using electromagnetic coils we can control the stick-slip motion. An in-plane field is applied to orient the micro transporters but the force exerted is not high enough to overcome the frictional forces to translate them. A sinusoidal out-of-plane field with an amplitude of 1 mT is applied using the electromagnetic coil placed above the surface which induces a rocking motion. The main difference

with [13] lies in the scale of the robots and their magnetization. In contrast to this previous work which relies on hard magnets, our robots are based on ferromagnetic particles which are magnetized as needed. More importantly our robots are at same scale with the target mammalian cells in contrast to the robots in [13].

We first characterize the velocity of the transporters with respect to the pulsing frequency. Several trials were performed by varying the pulsing frequency (1-100 Hz). The velocity increases monotonically with increasing frequency (see Figure 6.3).

We then fix the pulsing frequency at 30 Hz and adjust the in-plane magnetic field strength to control the velocity of the transporters. We performed several trials with different microrobots by varying the current passing through the in-plane coils. Velocity increases linearly with increasing magnetic field strength (see Figure 6.4). If we assume that the robots have uniform magnetization M, the magnetic force exerted on the robots is given by

$$F = V(M \cdot \nabla)B \tag{6.1}$$

where V is the volume of the micro transporter and B is the applied magnetic field. According to this equation, a linear trend between velocity and magnetic field strength is expected. Furthermore, the small values of the velocity can be explained by the size of the robots as exerted force is a function of size.

6.3.2 Visual Tracking

Anthony Cowley developed the material in this section.

The visual tracking system developed fuses several individually unreliable detectors and estimators to establish a stable estimate of microtransporter pose. In order to alleviate the burden on experimental procedure, very few constraints are placed on expected image
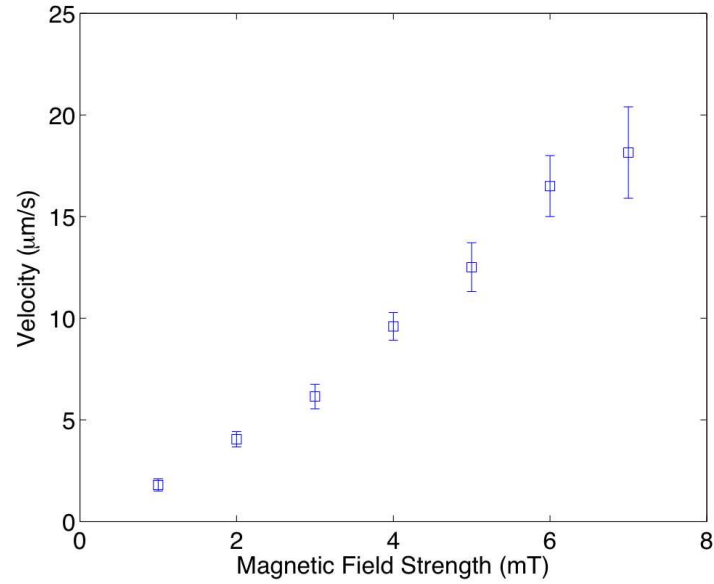
Figure 6.4: Micro transporter velocity as a function of magnetic field strength. Error bars indicate one standard error.
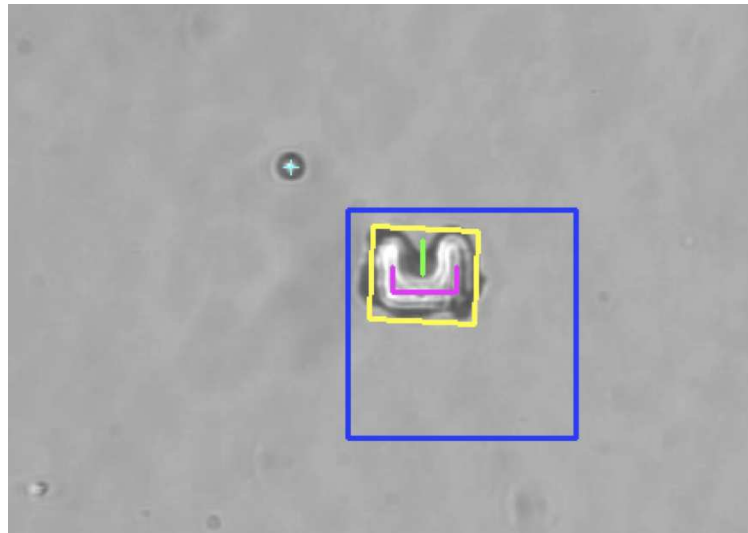
Figure 6.5: Microtransporter visual tracking output. The tracker estimates the position and orientation of the manipulator in 2D, as well as the positions of polystyrene beads. Several stages of processing are used to refine the estimate, resulting in a tracker capable of providing stable pose estimates at 30Hz. *Figure by Anthony Cowley.*

backgrounds or absolute image characteristics. Instead, relative measures are preferred wherever possible, while each processing stage refines the region of interest fed into subsequent stages. The output of the entire tracking scheme running at 30Hz is highlighted in Figure 6.5.

The first winnowing of the field of view is a block matching optical flow estimation that tends to disregard smaller, out of focus moving particles present in the field of view. The centroid of the largest region of moving blocks is used to identify the center of interest for subsequent processing stages, and is shown as a blue rectangle in Figure 6.5.

The image of the manipulator is primarily characterized by a dark outline, a light interior, and a cup-like (⊔) shape. None of these features can be treated too literally however, as the outlines of the manipulators used in different experiments will be corrupted by particles in the environment adhering to the manipulator itself, while the lighter interior of the image is often broken up by particles sticking to the top of the manipulator. Rather than attempt to extract a closed contour for the manipulator's perimeter, we find an oriented rectangular structure by considering projections of dark pixels. Locally dark pixels are projected into a histogram associated with each orientation, and the pair of histograms associated with orthogonal projections with the lowest entropy bimodal distributions along the axes of projection are used to identify an orientation, localization, and scale of the likely outline of the manipulator. The resulting rectangle is shown in yellow in Figure 6.5.

The identified rectangle is used to guide a procedure that fits a model of the manipulator structure with the light interior region of the manipulator image. To this end, a fixed range flood fill is initiated at the brightest component inside the estimated perimeter. The topological skeleton of the resulting connected component is then fed into a shape detector that searches for a minimal entropy bimodal projection perpendicular to a unimodal projection. These projections correspond to the parallel uprights and the base of the idealized cup shape, respectively, and are shown in violet in Figure 6.5. The manipulator can rotate

95

instantaneously, but tends to translate at a more measured pace. A motion model consistent with this observation is used to guide a particle filter on the structure's pose, shown by the green line segment in the figure.

Finally, beads are tracked by feeding the output of a Hough transform-based circle detector into a simple particle filter. An example bead detection is show by a cyan + symbol in Figure 6.5.

6.4 Fabrication of Microgels

By engineering the size, shape, and network density of the hydrogel particles, the release kinetics of the encapsulated molecules can be controlled. As the sizes of target cells varies depending on biomedical application, having control over the size of the gel is essential. For these reasons, and also to be able to integrate microgels with our magnetic micro transporters, we fabricate gels using photolithography and replica molding [90]. Photolithographic techniques were previously used to produce monodisperse hydrogel microstructures of controlled shape and size. Similar protocols were followed to prepare collagen [91] and alginate hydrogels [92].

A schematic of the complete fabrication process is given in Figure 6.6. SU8 master posts are fabricated on a silicon wafer using photolithography. We form poly(dimethyl siloxane) (PDMS) molds to serve as templates for microgel structures using replica molding. To prepare the PDMS molds for treatment with the gel, we oxidize them in air plasma to render their surfaces hydrophilic. They can also be placed in jars filled with water and degassed under house vacuum to remove air bubbles as suggested in [91] to increase throughput.

Agarose gel is prepared by mixing 6% agarose with DI water and heating the mixture in a microwave oven until the agar is completely dissolved. Molten solution is immediately
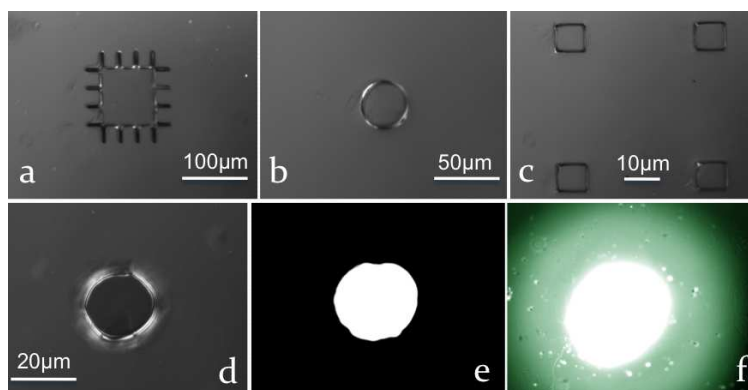
Figure 6.6: (a)-(c) Microfabricated hydrogels in different shape and sizes. (d) Phase-contrast and (e) fluorescent images of a fluorescein doped microgel. (f) Diffusion of fluorescein molecules from the microgel in water.)

poured onto the PDMS mold while it is hot and excess solution is scraped off the surface of the mold with a clean razor blade. Microgels are then removed from the mold and transferred to the experimental chamber by agitating gels with tweezers.

Hundreds of microgels can be conveniently formed at one time in one mold. Both the PDMS molds and the master posts can be reused at least dozens of times. Microgels can be stored for months in a refrigerator. We fabricate microgels in different shapes and with sizes ranging from 10 to 100 μm (see Figure 6a-c). In order demonstrate the ability to deliver chemicals with microgels, we visualize the diffusion profile around the gel using ultraviolet fluorescence. Microgels are doped with fluorescein by mixing the molten agarose solution with 0.1% fluorescein powder throughly before filling the PDMS molds. Figure 6d displays phase contrast images of one of the fabricated microgels. With the addition of fluid, fluorescein molecules start to diffuse and fluorescent microscopy is used to visualize the diffusion (Figure 6e-f). Figure 6f shows a snapshot of the concentration profile forming around the microgel after one minute.

6.5 Results

In all experiments, an in-plane constant field of 3 mT and a sinusoidal out-of-plane field with amplitude of 1 mT at 30 Hz is applied to actuate micro transporters that have a characteristic length of 30μm. Supporting online video shows the micro transporter performing the tasks presented in this section.

6.5.1 Automated transport of Latex Microbeads

A demonstration of automated transport of a latex microbead is performed using the pose estimate from the tracking algorithm (see Figure 7). The tracking algorithm identifies the position and orientation of the robot as well as a target microbead. A two-step trajectory is planned with movement confined along major axes. The robot is first adjusted along the vertical axis at a speed of 6 μm/s until aligned with the microbead. Once aligned horizontally with the microbead, the robot is reoriented for engagement. The bead moves approximately 40 μm in the direction of motion of the robot before contact, as would be expected due to strong fluid coupling. It should be noted that the moment of contact is approximate due to the refraction of light by the bead and robot. The bead is released by reversing the direction of motion of the robot while keeping the orientation constant. Again, the bead follows the motion of the robot due to viscous coupling and surface adhesion before coming to rest at a position approximately 40 μm from its location at the moment of robot reversal.

6.5.2 Transport of Agarose Microbeads

The size and shape of the target object determines the drag coefficient and changes the overall velocity of transport. To characterize the effect of size and estimate the force applied by our micro transporters, we move several different agarose microbeads with sizes
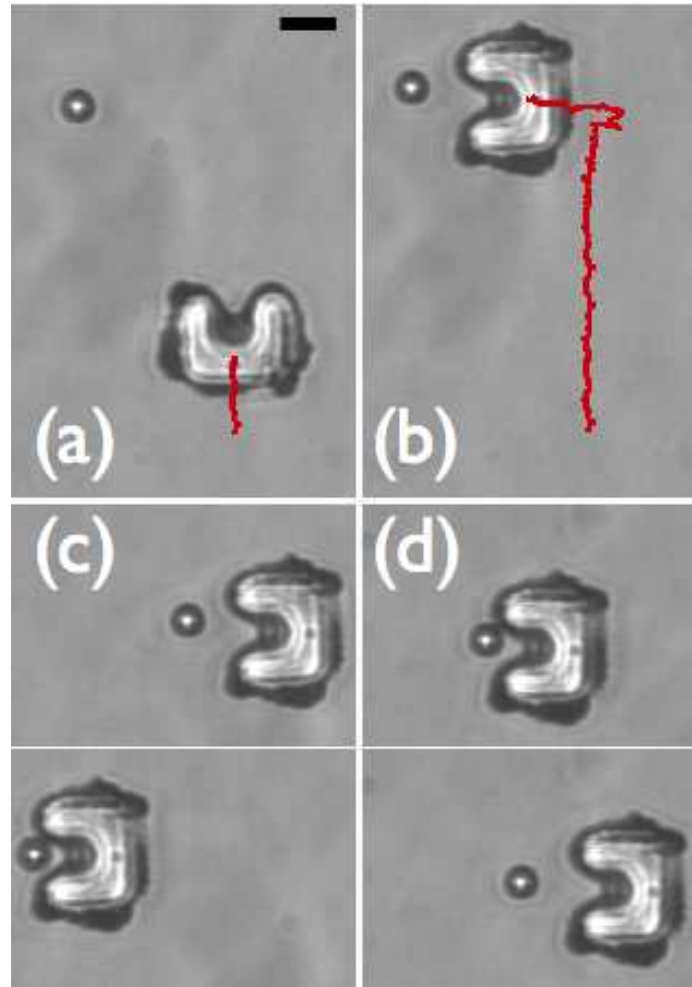
Figure 6.7: Automated transport of a 10μm latex microbead. (a) The position of target bead and the micro transporter is detected and used to plan a two-step trajectory. (b) The transporter successfully follows the pre-planned path and engages the target. (c) When the transporter approaches the target, non-contact manipulation is observed. The target bead moves slower than the transport until the transporters comes into contact. (d) The bead is released by moving the transporter back in the same orientation. Again, target moves with the transporter for a while due to fluid coupling. Scale bar is 20 μm.
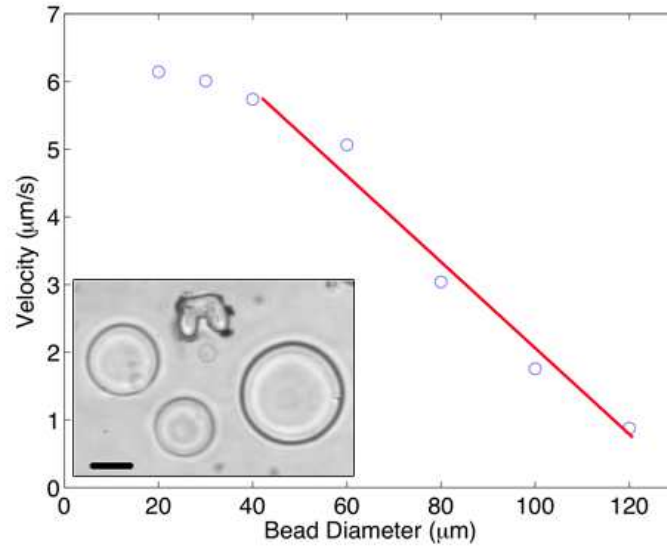
Figure 6.8: The velocity of the transporter plus microbead as a function of the size of the microbead. Agorose microbeads in different size and the microrobot are shown in the inset figure. Scale bar is 30 μm

changing from 10μm to 120μm (see Figure 6.8). We are able to transport beads four times larger and three times smaller in characteristic length than the size of the transporter which shows the scalability of our approach.

The viscous drag force of the fluid acting on a microbead at low Reynolds number regime is given by

$$F_{drag} = 6\pi\mu RV \tag{6.2}$$

where μ is the viscosity of the fluid, R is the radius and V is the velocity of the microbead. As the size of the transported bead increases, the drag force acting on the bead becomes the dominant viscous force for the transporter/microbead pair as the transporter is shadowed by the bead. For beads larger than the size of the transporter (30 μm) the velocity is expected to decrease linearly with increasing bead size. Experimental results showed that this is indeed the case (Figure 6.8). From equation (1), the force applied by the transporter

can be estimated. Microbeads with a radius of 60 μm are moved with an average velocity of 1 μm/s which gives a force around 1 pN in water at room temperature. We are capable of applying forces in the order of pico Newtons which makes our system safe for manipulation tasks. Mammalian cells can be transported at this force rating without causing any structural damage.

6.5.3 Manipulation of *Tetrahymena* cells

The experiments in this section are conducted with Dalhyung Kim.

Manipulating cells is fundamental to much of biology and biotechnology. Integral to these assays is the need to manipulate the physical location of cells, either to separate them from phenotypically different cells or to organize them in vitro. Owing to the small size and typically large numbers of cells, we need surrogate hands to provide efficient physical access to cells that our fingers cannot grasp. As a demonstration of the ability to seperate single cells, we separated dead *T. pyriformis* cells from living ones using the micro transporters. *T. pyriformis* is a protozoon that swims using cilia, a common locomotive appendage in eukaryotes. It is frequently used as a model cell in biochemistry and cell biology due to its complex genetic and structural makeup [93].

Cells are cultured using standard medium containing 0.1% yeast extract and 1% tryptone (Difco, Michigan, USA) solved in distilled water [94]. The cells were deciliated with a local anesthetic called dibucaine resulting in a suspension of non-motile cells that do not adhere to the surface [95]. Exposing the cells to the anesthetic for 3-5 min is long enough to completely detach cilia without killing them. We extended this period in order to have a heterogeneous population of deciliated dead and live *T. pyriformis* cells. Cultures to be deciliated (cell density 10^5 cells ml^{-1}) were suspended in 1.8 ml of standard medium and 0.2 ml 0.5 mM dibucaine HCl (Sigma-Aldrich, USA). After 6 min of exposure, the cells were transferred to the standard medium. We verified that all cell motility was lost using
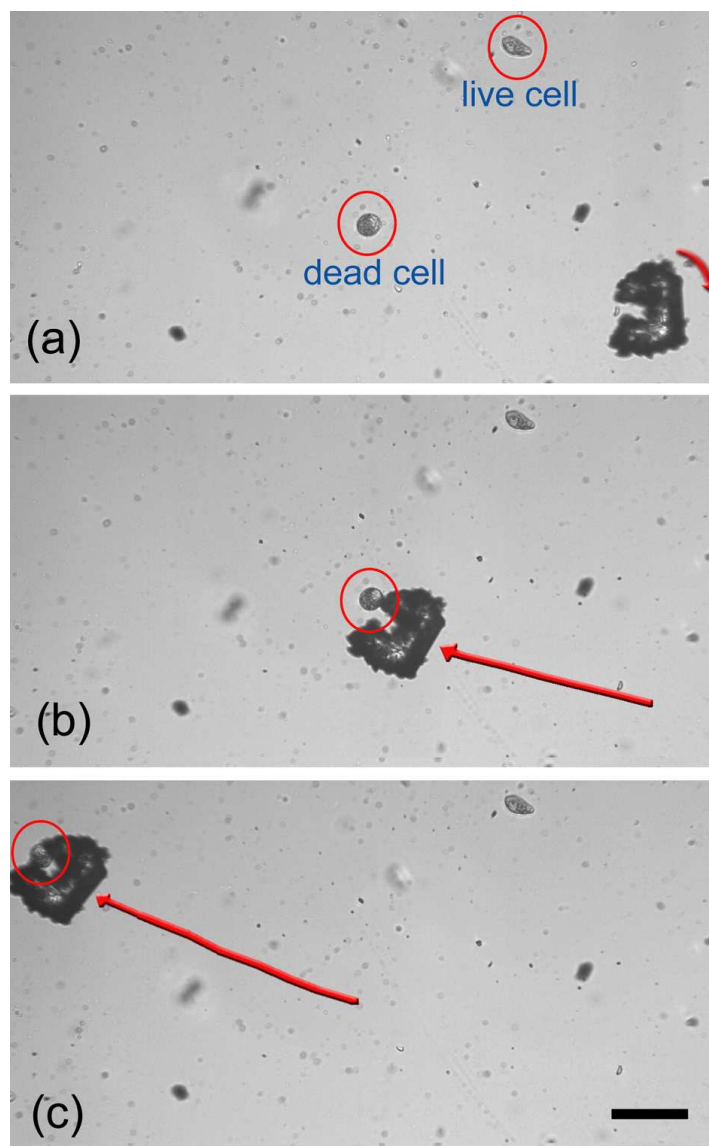
Figure 6.9: Transport of target cells. (a) The orientation of the transporter is adjusted according to the position of the target cell. (b) With the application of an out-of-plane time-varying magnetic field, the transporter starts translating towards the target. The pulsing frequency is 100 Hz. (c) The target is engaged and transported out of the field of view. The average velocity of the transporter is 350 μm/s. The scale bar is 100 μm.

phase-contrast microscopy.

Cells and micro transporters were released into the same open channel. First, a micro transporters/target pair was selected and the center of mass of the target dead cell was calculated using our tracking algorithm. These cells can easily be detected due to their distinct morphological appearance. They have a spherical shape while live cells look like ellipsoids. Next, the orientation of the transporter was adjusted according to the position of the target cell (Figure 6.9(a)). In the absence of an out-of-plane magnetic field, the transporter was kept in position while the orientation was changed. By applying a time-varying field with a pulsing frequency of 100 Hz, we were able to induce a smooth motion and translate the transporter towards the target cell and accomplish the engagement (Figure 6.9(b)). Finally, the cell was cleared out of the field of view (Figure 6.9(c)). In our experiments, while the manipulation of target cells was performed, the position of other cells kept unchanged unless they were in close proximity (less than 100 μm). This is expected since the flow in the far field falls of inversely with the square of the distance in the low Reynolds regime. We were able to release transported cells and use the same micro transporter multiple times. However, this result cannot be generalized for other cell types.

For applications in which target cells look physically similar to the rest of the cells, fluorescence microscopy can be employed. Target cells can be labeled using fluorescent dyes, fluorescent proteins (i.e. GFP) or quantum dots.

6.5.4   Manipulation of Hippocampal Neurons

The experiments in this section are conducted with Sean Kim.

We perform two different experiments with rat hippocampal neurons. In the first experiment, we demonstrate that cells can be transported and released with micron precision. Positioning cells in open and closed microchannels is an important step toward studying cell-cell communication and cell differentiation. In the second experiment, we show the
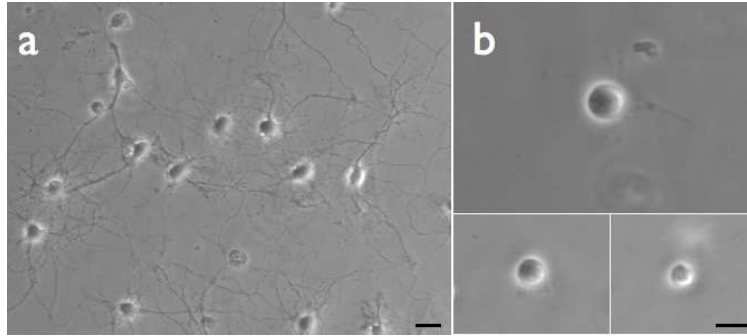
Figure 6.10: Phase-contrast images of rat hippocampal neurons. (a) After 10 days in culture, an extensive, intertwined network of neurons develops on glass slides. (b) Trypsinized neurons. Scale bars, 25 μm

feasibility of delivering drugs to immobilized cells by placing microgels close to neurons patterned on glass slides.

Neuron-enriched primary rat hippocampal cultures are plated at 100,000 per ml in Neurobasal medium (Invitrogen) with B-27 supplement (Sigma) on poly-L-lysine coated 12-mm round coverslips [96]. Upon attachment to the substrate, a continuous lamella extends around the cell body. This is followed by the emergence of axon. The axon extends for many hundreds of micrometers. After two days, the dendrites begin to grow and with time the dendrites become more highly branched [97]. After a week, an extensive, intertwined network of axons and dendrites is observed (see Figure 6.10a).

Transport of cells

We detach cultured neurons from the surface by trypsinizing them in a solution (CMF-HBSS containing 0.5 mM EDTA and 0.05 % trypsin) for 10 min at room temperature. Trypsin cleaves axons and dendrites and harvested cells change their morphology by taking a ball shape as shown in Figure 6.10b. Their dimensions vary from 10μm to 30μm . Cells are transferred onto another cover slip using a micropipette and micro transporters are released into the same fluid.
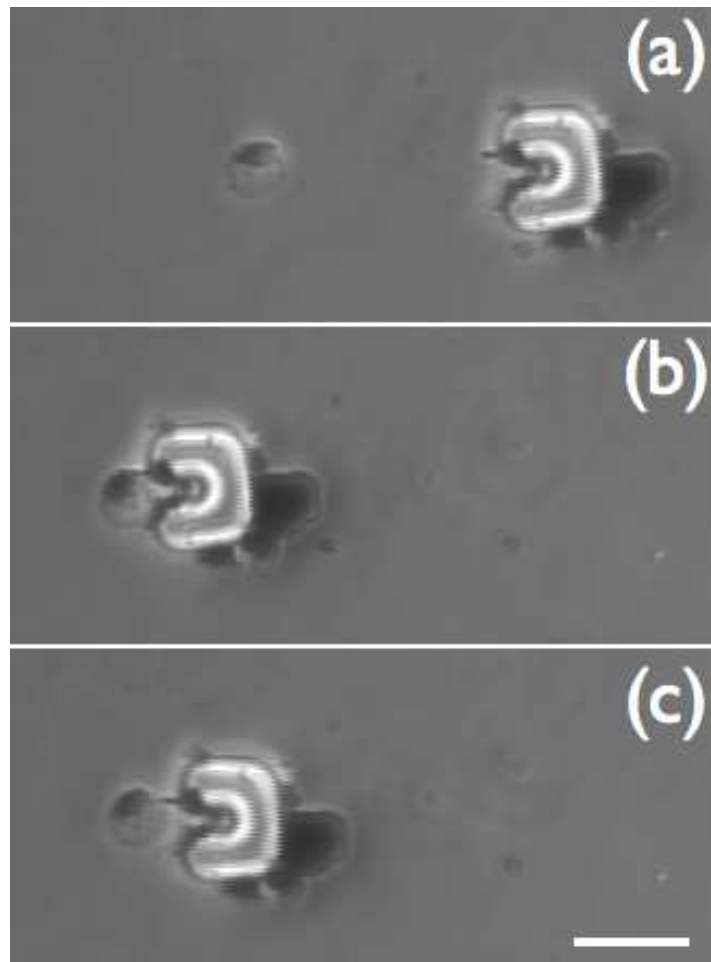
Figure 6.11: Transport of trypsinized neurons. (a) A cell is detected and targeted for manipulation. (b) The target is engaged and transported. (c) Transported cell is released by moving the micro transporter to the left with the same orientation. The scale bar is 30μm.

A micro transporter/target cell pair is selected and a path is planned for the manipulation task (Figure 6.11a). When the transporter is in close proximity, the cell starts to move due to fluidic effects (Figure 6.11b). We successfully release the target cell by moving the transporter in the opposite direction without changing its orientation (Figure 6.11c). Adhesion between cells and transporters is observer but this doesn't prevent release due to the shape of the robot and surface properties of trypsinized neurons.

Delivering microgels to patterned cells

Bioassays using cultured cells have been conventionally carried out for drug screening. Cellular assays have focused on the activity of individual cells as well as the function of cellcell networks in interconnected systems. These are both important measures for drug analysis [98]. A bioassay based on cellular networks would benefit from the techniques of the precise patterning of cells and the local dosing to the cellular patterns.

Here, a non-invasive technique for delivering small doses of chemicals locally to a specific area of the patterned rat hippocampal neurons is introduced by using microgels and micro transporters together. Unlike microfluidic solutions, we do not disturb the local chemical environment. Only the individual target cell is manipulated by the presence of gels and robots. micro transporters can be actuated on rough surfaces such as glass slides patterned with neurons thanks to its low density and induced rocking motion. Microfabricated 8μm circular microgels and micro transporters are released on 10-day old cultured neurons. Microgels are successfully transported, positioned and released on predetermined spots (Figure 6.12).
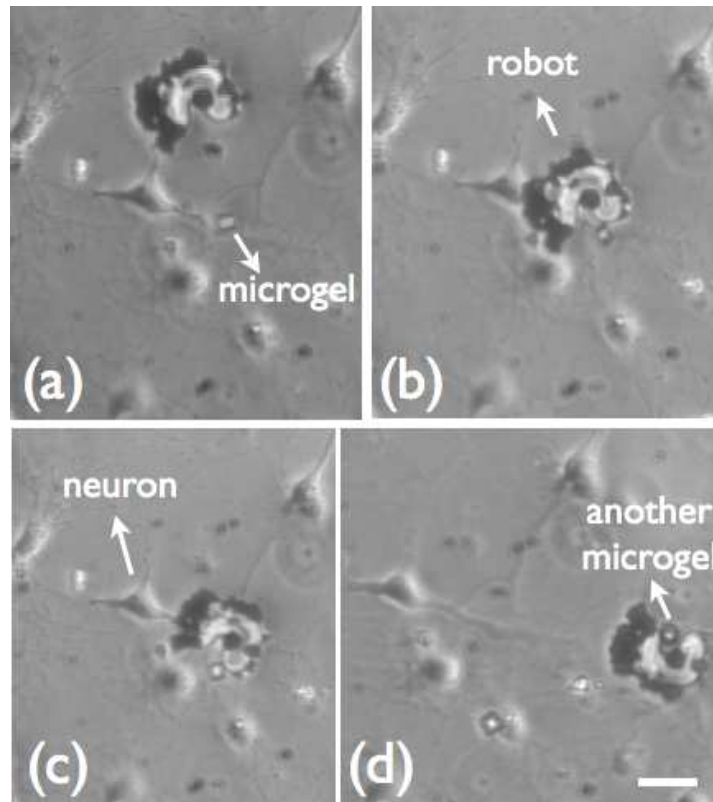
Figure 6.12: Delivery of microgels to the hippocampal cultures. (a)-(c) A microgel is transported from its initial position to its target location. micro transporters can be teleoperated on the neuron-coated surface without causing structural damage to cells. (d) After releasing the microgel, another target is detected and transported. The scale bar is 30μm.

6.6 Discussion

The effect of fluid, physical forces and the concentration of chemicals on cell behavior must be taken into account when designing microenvironments [99]. Our approach is non-invasive and requires minimum fluidic disturbance to accomplish manipulation tasks. By integrating microfabricated microgels with magnetic micro transporters, we showed the feasibility of delivering chemicals locally and engineering more *in vivo*-like microenvironments *in vitro*. The effect of multiple growth factors and therapeutic agents on cells can be analyzed by combining mechanical and chemical manipulation *in vitro*.

We are currently developing an experimentally validated mathematical model describing the dynamics of the system. The behavior of the micro transporters depends on their shape, the weight ratio of the suspended magnetite particles, the strength of the applied magnetic fields and the excitation waveform driving the electromagnets. The effect of each factor needs to be characterized to optimize the overall performance. The microfabrication process can also be improved by measuring the optical properties of the ferromagnetic photoresist and accordingly optimizing the exposure time.

The current size of the robots is ideal for the manipulation of mammalian cells. However, we are planning to use micro transporters with yeast cells for aging studies which requires further reduction in size. In addition, the shape of the robot is optimized for transport tasks. However, for performing other tasks such as separation, injection, dissection of living cells and applying forces to cultured neurons and fibroblasts, we would like to employ robots with different shapes. In our future studies, we will expand our work and apply these criteria in our designs.

The diffusion kinetics of the delivered chemical needs to be tuned. Drugs should be delivered at pre-determined times and with specific doses. These factors can be adjusted by changing the shape and the size of the microgels and our fabrication technique allows

such changes. The amount of agarose is another important factor determining the diffusion rate. The size of the pores inside the microgel decreases as the concentration of agarose is increased. Our future work will address the characterization of the temporal and spatial dynamics of diffusion of chemicals from microgels.

Chapter 7

Conclusions

7.1   Summary of Contributions

In the first part, we first investigate and characterize the fundamental phenomena for controlling rotation and translation of engineered microscale structures using bacteria stimulated by UV light and electric fields. Several important experimental techniques for building *MicroBioRobots* (MBRs) are proposed and a theoretical framework for modeling and control of MBRs is presented. In particular, we propose a method of controlling MBRs using self actuation and DC electric fields, and develop experimentally validated mathematical model for MBRs.The electrokinetic phenomena are found to be primarily electrophoretic, with the primary of component of MBR velocity related directly to the strength of the electric field. A custom-designed chamber is created to apply direct current electric fields in two-dimensions, while also enabling continuous tracking and application of UV light. The photoresponsiveness of the cells is used to temporarily halt rotation of MBRs, downwardly adjust angular velocity, or permanently stop rotational motion, which was vital for the positioning of U-shaped microtransporters. A stochastic model of the dynamic motion is additionally developed to understand and predict the motion of microstructures

propelled by large populations of cells.

We demonstrate experimentally that vision-based feedback control allows a four- electrode experimental device to steer MBRs along arbitrary paths with micrometer precision. At each time instant, the system identifies the current location of the robot, a control algorithm determines the power supply voltages that will move the charged robot from its current location toward its next desired position, and the necessary electric field is then created. Examples of microscale transport and assembly as well as computer-based control of MBRs are presented. We also describe the development of biosensors for the MBRs by combining synthetic biology with microrobotics research.

In the second part, we describe the construction and operation of truly micron-sized, biocompatible ferromagnetic micro transporters driven by external magnetic fields. Our five-coiled, compact actuation system is designed for rapid integration with existing microscopes. We use a real-time visual tracking algorithm for tracking transporters and target objects. This information is used to implement fully automated manipulation of latex microbeads. We also demonstrate the transport of rat hippocampal neurons and fabricated microgels with teleoperation. Microgels are positioned at target locations on cell-patterned surfaces as a first step for delivering drugs to cultured neurons.

7.2   Future Work

MBRs can be used as building blocks for more sophisticated functional microdevices. Furthermore, the paradigm introduced here can be integrated with other microelectromechanical systems (MEMS) technologies. Our techniques can be used to fabricate, calibrate and transport MBRs in microfluidic channels in a controllable fashion. Our future work will also address the integration of biosensing and bio-actuation onboard the MBR.

We envision that, in near future, magnetic micro transporter systems can be employed

as standard tools for single cell studies in bioengineering laboratories. Currently, micromanipulators and Fluorescence Activated Cell Sorting (FACS) devices are used for separating fluorescently-labeled cells. However, mammalian cells such as neurons like to grow in close proximity with other cells and analysis of such cells in isolation for extended period of times results in necrosis. Using micropipettes and aspiration limits the number of cells that can be analyzed simultaneously. Microrobots can solve these problems by introducing the capability of automated non-invasive transport and positioning of single cells as well as localized delivery of drugs. In our future work, we will explore lipid and photo transfection of rat hippocampal neurons and fibroblasts using magnetic micro transporters and microsources (drug-loaded microgels and mircobeads).

Bibliography

[1] J. T. Mettetal, D. Muzzey, J. M. Pedraza, E. M. Ozbudak, and A. van Oudenaarden, "Predicting stochastic gene expression dynamics in single cells," *Proceedings of the National Academy of Sciences*, vol. 103, pp. 7304–7309, 2006.

[2] J. J. Abbott, Z. Nagy, F. Beyeler, and B. J. Nelson, "Robotics in the small, part i: Microbotics," *Robotics and Automation Magazine, IEEE*, vol. 14, pp. 92–103, 2007.

[3] E. M. Purcell, "Life at low reynolds number," *American Journal of Physics*, vol. 45, pp. 3–11, 1976.

[4] B. R. Donald, C. G. Levey, and I. Paprotny, "Planar microassembly by parallel actuation of mems microrobots," *Journal of Microelectromechanical Systems*, vol. 17, pp. 789–808, 2008.

[5] R. Dreyfus, M. L. Roper, H. A. Stone, and J. Bibette, "Microscopic artificial swimmers," *Nature*, vol. 437, pp. 862–865, 2005.

[6] L. Zhang, K. E. Peyer, and B. J. Nelson, "Artificial bacterial flagella for micromanipulation," *Lab on a Chip*, vol. 10, pp. 2203–2215, 2010.

[7] A. Ghosh and P. Fischer, "Controlled propulsion of artificial magnetic nanostructured propellers," *Nano Letters*, vol. 9, pp. 2243–2245, 2009.

[8] P. Garstecki, P. Tierno, D. B. Weibel, F. Sagues, and G. M. Whitesides, "Propulsion of flexible polymer structures in a rotating magnetic field," *Journal of Physics..:Condensed Matter*, vol. 21, 2009.

[9] F. Fahrni, M. W. J. Prins, and L. J. v. IJzendoorn, "Microfluidic actuation using magnetic artificial cilia," *Lab on a Chip*, vol. 9, pp. 3413–3421, 2009.

[10] O. Ergeneman, G. Dogangil, M. P. Kummer, J. J. Abbott, M. K. Nazeeruddin, and B. J. Nelson, "A magnetically controlled wireless optical oxygen sensor for intraocular measurements," *IEEE Sensors Journal*, vol. 8, pp. 29–37, 2008.

[11] J. J. Abbott, K. E. Peyer, M. C. Lagomarsino, L. Zhang, L. Dong, I. K. Kaliakatsos, and B. J. Nelson, "How should microrobots swim?" *International Journal of Robotics Research*, vol. 28, pp. 1434–1447, 2009.

[12] M. Dauge, M. Gauthier, and E. Piat, "Modelling of a planar magnetic micropusher for biological cell manipulations," *Sensors and Actuators A*, vol. 138, pp. 239–247, 2007.

[13] C. Pawashe, S. Floyd, and M. Sitti, "Modeling and experimental characterization of an untethered magnetic micro-robot," *International Journal of Robotics Research*, vol. 28, pp. 1077–1094, 2009.

[14] K. Vollmers, D. R. Frutiger, B. E. Kratochvil, and B. J. Nelson, "Wireless resonant magnetic microactuator for untethered mobile microrobots," *Applied Physics Letters*, vol. 92, p. 144103, 2008.

[15] D. R. Frutiger, K. Vollmers, B. E. Kratochvil, and B. J. Nelson, "Small, fast, and under control: wireless resonant magnetic micro-agents," *International Journal of Robotics Research*, vol. 29, pp. 613–636, 2010.

[16] R. S. et al., "Powering an inorganic nanodevice with a biomolecular motor," *Science*, vol. 290, pp. 1555–1558, 2000.

[17] M. G. L. van den Heuvel and C. Dekker, "Motor proteins at work for nanotechnology," *Science*, vol. 317, pp. 333–336, 2007.

[18] A. W. Feinberg, A. Feigel, S. S. Shevkoplyas, S. Sheehy, G. M. Whitesides, and K. K. Parker, "Muscular thin films for building actuators and powering devices," *Science*, vol. 317, pp. 1366–1370, 2007.

[19] J. Xi, J. J. Schmidt, and C. D. Montemagno, "Sel-assembled microdevices driven by muscle," *Nature Materials*, vol. 4, no. 180-190, 2005.

[20] Y. Akiyama, K. Iwabuchi, Y. Furukawa, and K. Morishima, "Long-term and room tempreature operable bioactuator powered by insect dorsal vessel tissue," *Lab on a Chip*, vol. 9, pp. 140–145, 2009.

[21] Y. Hiratsuka, M. Miyata, T. Tada, and T. Uyeda, "A microrotary motor powered by bacteria," *Proceedings of the National Academy of Sciences*, vol. 103, pp. 13 618–13 623, 2006.

[22] N. Darnton, L. Turner, K. Breuer, and H. C. Berg, "Moving fluid with bacterial carpets," *Biophysical Journal*, vol. 86, pp. 1863–1870, 2004.

[23] D. B. Weibel, P. Garstecki, D. Ryan, W. R. DiLuzio, M. Mayer, J. E. Seto, and G. M. Whitesides, "Microoxen: Microorganisms to move microscale loads," *Proceedings of the National Academy of Sciences*, vol. 102, pp. 11 963–11 967, 2005.

[24] M. Nagai, S. Ryu, T. Thorsen, P. Matsudaira, and H. Fujita, "Chemical control of vorticella bioactuator using microfluidics," *Lab on a Chip*, vol. 10, pp. 1574–1578, 2010.

[25] N. Ogawa, H. Oku, K. Hashimoto, and M. Ishikawa, "Dynamics model of paramecium galvanotaxis for microrobotic application." Barcelona, Spain: IEEE Conference on Robotics and Automation, 2005.

[26] D. H. Kim, D. Casale, L. Kohidai, and M. J. Kim, "Galvanotactic and phototactic control of tetrahymena pyriformis as a microfluidic workhorse," *Applied Physics Letters*, vol. 94, 2009.

[27] M. J. Kim and K. S. Breuer, "Controlled mixing in microfluidic systems using bacterial chemotaxis," *Analytical Chemistry*, vol. 79, pp. 955–959, 2007.

[28] A. Sokolov, M. M. Apodaca, B. A. Grzybowski, and I. S. Aranson, "Swimming bacteria power microscopic gears," *Proceedings of the National Academy of Sciences*, vol. 107, pp. 969–974, 2010.

[29] R. D. Leonardo, L. Angelani, D. Dell'Arciprete, G. Ruocco, V. Lebba, S. Schippa, M. P. Conte, F. Mecarini, F. D. Angelis, and E. D. Fabrizio, "Bacterial ratchet motors," *Proceedings of the National Academy of Sciences*, vol. 107, pp. 9541–9545, 2010.

[30] S. Martel, C. Tremblay, S. Ngakeng, and G. Langlois, "Controlled manipulation and actuation of micro-objects with magnetotactic bacteria," *Applied Physics Letters*, vol. 89, 2006.

[31] B. Behkam and M. Sitti, "Bacterial flagella-based propulsion and on/off motion control of microscale objects," *Applied Physics Letters*, vol. 90, 2007.

[32] E. Steager, C.-B. Kim, C. Naik, J. Patel, S. Bith, L. Reber, and M. J. Kim, "Control of microfabricated structures powered by flagellated bacteria using phototaxis," *Applied Physics Letters*, vol. 90, 2007.

[33] W. R. DiLuzio, L. Turner, M. Mayer, P. Garstecki, D. B. Weibel, H. C. Berg, and G. M. Whitesides, "Escherichia coli swim on the right-hand side," *Nature*, vol. 435, pp. 1271–1274, 2005.

[34] J. P. Desai, A. Pillarisetti, and A. D. Brooks, "Engineering approaches to biomanipulation," *Annual Review of Biomedical Engineering*, vol. 9, pp. 35–53, 2007.

[35] M. S. Sakar, E. B. Steager, D. H. Kim, M. J. Kim, G. J. Pappas, and V. Kumar, "Single cell manipulation using ferromagnetic composite microtransporters," *Applied Physics Letters*, vol. 96, p. 043705, 2010.

[36] T. G. Leong, C. L. Randall, B. R. Benson, N. Bassik, G. M. Stern, and D. H. Gracias, "Thetherless thermobiochemically actuated microgrippers," *Proceedings of the National Academy of Sciences*, vol. 106, no. 3, pp. 703–708, 2009.

[37] S. Floyd, C. Pawashe, and M. Sitti, "Two-dimensional contact and noncontact micromanipulation in liquid using an untethered mobile magnetic microrobot," *IEEE Transactions on Robotics*, vol. 25, pp. 1332–1342, 2009.

[38] C. Pawashe, S. Floyd, and M. Sitti, "Multiple magnetic microrobot control using electrostatic anchoring," *Applied Physics Letters*, vol. 94, p. 164108, 2009.

[39] B. G. D. Geest, S. D. Koher, J. Demeester, S. C. D. Smedt, and W. E. Hennink, "Self-exploding capsules," *Polymer Chemistry*, vol. 1, pp. 137–148, 2010.

[40] N. A. Peppas, J. Z. Hilt, A. Khademhosseini, and R. Langer, "Hydrogels in biology and medicine: from molecular principles to bionanotechnology," *Advanced Materials*, vol. 18, pp. 1345–1360, 2006.

[41] E. Lauga and T. R. Powers, "The hydrodynamics of swimming microorganisms," *Reports on Progress in Physics*, vol. 72, p. 096601, 2009.

[42] L. Turner, W. S. Ryu, and H. C. Berg, "Real-time imaging of fluorescent flagellar filaments," *Journal of Bacteriology*, vol. 182, pp. 2793–2801, 2000.

[43] H. C. Berg, "Motile behavior of bacteria," *Physics Today*, vol. 53, no. 1, pp. 24–29, 2000.

[44] M.-J. Kim, J. C. Bird, A. J. V. Parys, K. S. Breuer, and T. R. Powers, "A macroscopic scale model of bacterial flagellar bundling," *Proceedings of the National Academy of Sciences*, vol. 100, pp. 15 481–15 485, 2003.

[45] M.-J. Kim, M.-J. Kim, J. C. Bird, J. Park, T. R. Powers, and K. S. Breuer, "Particle image velocimetry experiments on a macro-scale model for bacterial flagellar bundling," *Experiments in Fluids*, vol. 37, pp. 782–788, 2004.

[46] I. R. Gibbons, "Cilia and flagella of eukaryotes," *Journal of Cell Biology*, vol. 91, pp. 107–124, 1981.

[47] M. Polin, I. Tuval, K. Drescher, J. P. Gollup, and R. E. Goldstein, "Chlamydomonas swims with two "gears" in a eukaryotic version of run-and-tumble locomotion," *Science*, vol. 325, pp. 487–490, 2009.

[48] R. M. Macnab, *Escherichia coli and Salmonella: Cellular and Molecular Biology*. Am. Soc. Microbiol. Washington, DC, 1996.

[49] R. P. Blakemore, "Magnetotactic bacteria," *Science*, vol. 190, pp. 377–379, 1975.

[50] M. Khammash and H. El-Samed, "Systems biology: From physiology to gene regulation," *IEEE Control Systems Magazine*, pp. 62–76, August 2004.

[51] E. L. Berg, E. J. Kunkel, and E. Hytopoulos, "Biological complexity and drug discovery: a practical systems biology approach," *Syst. Biol.*, vol. 152, no. 4, pp. 201–206, December 2005.

[52] A. Raj and A. van Oudenaarden, "Nature, nurture, or chance: stochastic gene expression and its consequences," *Cell*, vol. 135, pp. 216–226, 2008.

[53] N. Q. Balaban, J. Merrin, R. Chait, L. Kowalik, and S. Leibler, "Bacterial persistence as a phenotypic switch," *Science*, vol. 305, pp. 1622–1625, 2004.

[54] E. Kussell and S. Leibler, "Phenotypic diversity, population growth, and information in fluctuating environments," *Science*, vol. 309, p. 2075, 2005.

[55] S. V. Avery, "Microbial cell individuality and the underlying sources of heterogeneity," *Nature Reviews Microbiology*, vol. 4, pp. 577–587, 2006.

[56] M. Sitti, "Miniature devices: Voyage of the microrobots," *Nature*, vol. 458, pp. 1121–1122, 2009.

[57] A. A. Julius, A. Halasz, M. S. Sakar, H. Rubin, V. Kumar, and G. J. Pappas, "Stochastic modeling and control of biological systems: the lactose regulation system of *Escherichia coli*," *IEEE Transactions on Automatic Control*, vol. 53, pp. 51–65, 2008.

[58] J. Ueda, L. Odhner, and H. Asada, "Broadcast feedback of stochastic cellular actuators inspired by biological muscle control," *International Journal of Robotics Research*, vol. 26, no. 11, pp. 1251–1266, 2007.

[59] J. Halloy, G. Sempo, G. Gaprari, M. Asadpour, F. Tache, I. Said, V. Durier, S. Canonge, J. M. Ame, C. Detrain, N. Correll, A. Martinoli, F. Mondada, R. Siegwart, and J. L. Deneubourg, "Social integration of robots into groups of cockroaches to control self-organized choices," *Science*, vol. 318, pp. 1155–1159, 2007.

[60] A. A. Julius, M. S. Sakar, E. B. Steager, U. K. Cheang, M. J. Kim, V. Kumar, and G. J. Pappas, "Harnessing bacterial power in microscale actuation," in *IEEE International Conference on Robotics and Automation*, Kobe, Japan, 2009, pp. 1004–1009.

[61] H. C. Berg and D. A. Brown, "Chemotaxis in *Escherichia coli* analysed by three-dimensional tracking," *Nature*, vol. 239, pp. 500–504, 1972.

[62] H. C. Berg, *E. coli in motion*. New York: Springer-Verlag, 2004.

[63] H. C. Berg and R. A. Anderson, "Bacteria swim by rotating their flagellar filaments," *Nature*, vol. 245, pp. 380–382, 1973.

[64] B. Behkam and M. Sitti, "Effect of quantity and configuration of attached bacteria on bacterial propulsion of microbeads," *Applied Physics Letters*, vol. 93, 2008.

[65] C. G. Cassandras and S. Lafortune, *Introduction to Discrete Event Systems*. Kluwer, 1999.

[66] N. C. Darnton, L. Turner, S. Rojevsky, and H. C. Berg, "On torque and tumbling in swimming Escherichia coli," *Journal of Bacteriology*, vol. 189, pp. 1756–1764, 2007.

[67] M. S. Sakar, E. B. Steager, D. H. Kim, A. A. Julius, M. J. Kim, V. Kumar, and G. J. Pappas, "Modeling, control and experimental characterization of microbiorobots," *International Journal of Robotics Research*, accepted (invited paper).

[68] E. B. Steager, M. S. Sakar, D. H. Kim, V. Kumar, G. J. Pappas, and M. J. Kim, "Electrokinetic and optical control of bacterial microrobots," *Journal of Micromechanics and Microengineering*, (in review).

[69] N. Tandon, C. Cannizzaro, P.-H. G. Chao, R. Maidhof, A. Marsano, H. T. H. Au, M. Radisic, and G. Vunjak-Nocakovic, "Electrical stimulation systems for cardiac tissue engineering," *Nature Protocols*, vol. 4, pp. 155–173, 2009.

[70] B. Song, Y. Gu, J. Pu, B. Reid, Z. Zhoa, and M. Zhao, "Application of direct current electric fields to cells and tissues in vitro and modulation of wound electric field in vivo," *Nature Protocols*, vol. 2, pp. 1479–1489, 2007.

[71] W. Shi, B. A. D. Stocker, and J. Adler, "Effect of surface composition of motile e.coli and motile salmonella on the direction of galvanotaxis," *Journal of Bacteriology*, vol. 178, pp. 1113–1119, 1996.

[72] K. Atsuta, H. Noji, and S. Takeuchi, "Micro patterning of active proteins with perforated pdms sheets (pdms sieve)," *Lab on a Chip*, vol. 4, pp. 333–336, 2004.

[73] M. J. Kim and K. S. Breuer, "Microfluidic pump powered by self-organizing bacteria," *Small*, vol. 4, pp. 111–118, 2008.

[74] B. L. Taylor and D. E. Koshland, "Intrinsic and extrinsic light responses of salmonella typhimurium and escherischia coli," *Journal of Bacteriology*, vol. 123, pp. 557–569, 1975.

[75] D. H. Kim, E. B. Steager, U. K. Cheang, D. Byun, and M. J. Kim, "A comparison of vision-based tracking schemes for control of microbiorobots," *Journal of Micromechanics and Microengineering*, vol. 20, 2010.

[76] M. S. Sakar, E. B. Steager, D. H. Kim, A. A. Julius, M. J. Kim, V. Kumar, and G. J. Pappas, "Biosensing and actuation for microbiorobots," *IEEE International Conference on Robotics and Automation*, 2010.

[77] S. Takayama, J. C. McDonald, E. Ostuni, M. N. Liang, P. J. A. Kenis, R. F. Ismagilov, and G. M. Whitesides, "Patterning cells and their environments using multiple laminar fluid flows in capillary networks," *Proceedings of the National Academy of Sciences*, vol. 96, pp. 5545–5548, 1999.

[78] G. M. Walker and D. J. Beebe, "A passive pumping method for microfluidic devices," *Lab on a Chip*, vol. 2, pp. 131–134, 2002.

[79] A. Novick and M. Weiner, "Enzyme induction as an all-or-none phenomenon," *Proceedings of the National Academy of Sciences*, vol. 43, pp. 553–566, 1957.

[80] P. J. Choi, L. Cai, K. Frieda, and X. S. Xie, "A stochastic single-molecule event triggers phenotype switching of a bacterial cell," *Science*, vol. 322, p. 442, 2008.

[81] E. M. Ozbudak, M. Thattai, H. N. Lim, B. I. Shraiman, and A. V. Oudenaarden, "Multistability in the lactose utilization network of Escherichia coli," *Nature*, vol. 427, pp. 737–740, 2004.

[82] T. Miyashiro and M. Goulian, "Single cell analysis of gene expression by fluorescence microscopy," *Methods in Enzimology*, vol. 423, pp. 458–475, 2007.

[83] A. Cerf, J.-C. Cau, C. Vieu, and E. Dague, "Nanomechanical properties of dead and alive single-patterned bacteria," *Langmuir*, vol. 25, pp. 5731–5736, 2009.

[84] S. K. W. Dertinger, D. T. Chiu, N. L. Jeon, and G. M. Whitesides, "Generation of gradients having complex shapes usign microfluidic networks," *Analytical Chemistry*, vol. 73, pp. 1240–1246, 2001.

[85] C. H. C. F. H. A. S. Basu, Y. Gerchman and R. Weiss, "A synthetic multicellular system for programmed pattern formation," *Nature*, vol. 434, pp. 1130–1134, 2005.

[86] M. S. Sakar, E. B. Steager, A. Cowley, V. Kumar, and G. J. Pappas, "Wireless manipulation of single cells using magentic microtransporters," in *submitted to IEEE International Conference on Robotics and Automation*, 2011.

[87] L. Zhang, J. J. Abbott, L. Dong, B. E. Kratochvil, D. Bell, and B. J. Nelson, "Artificial bacterial flagella: Fabrication and magnetic control," *Applied Physics Letters*, vol. 94, p. 064107, 2009.

[88] N. Damean, B. A. Parviz, J. N. Lee, T. Odom, and G. M. Whitesides, "Composite ferromagnetic photoresist for the fabrication of microelectromechanical systems," *Journal of Micromechanics and Microengineering*, vol. 15, pp. 29–34, 2005.

[89] V. Linder, B. D. Gates, D. Ryan, B. A. Parviz, and G. M. Whitesides, "Water-soluble sacrificial layers for surface micromachining," *Small*, vol. 7, pp. 730–736, 2005.

[90] D. Qin, Y. Xia, and G. M. Whitesides, "Soft lithography for micro- and nanoscale patterning," *Nature Protocols*, vol. 5, pp. 491–502, 2010.

[91] A. P. McGuigan, D. A. Bruzewicz, A. Glavan, M. Butte, and G. M. Whitesides, "Cell encapsulation in sub-mm sized gel modules using replica molding," *PLOS one*, vol. 3, p. e2258, 2008.

[92] G. T. Franzesi, B. Ni, Y. Ling, and A. Khademhosseini, "A controlled-release strategy for the generation of cross-linked hydrogel microstructures," *Journal of American Chemical Society*, vol. 128, pp. 15 064–15 065, 2006.

[93] G. Csaba, "The unicellular tetrahymena as a model cell for receptor research," *International Review of Cytology*, vol. 95, pp. 327–377, 1985.

[94] L. Kohidai and G. Csaba, "Effects of the mammalian vasoconstrcitor peptide, endothelin-1, on *Tetrahymena pyriformis* gl, and the immunocytological detection of endogenous endothelin-like activity," *Comparative Biochemistry and Physiology Part C: Pharmacology, Toxicology, and Endocrinology*, vol. 111, pp. 311–316, 1995.

[95] G. A. Thompson, L. C. Baugh, and L. F. Walker, "Nonlethal deciliation of *Tetrahymena* by a local anesthetic and its utility as a tool for studying cilia regeneration," *Journal of Cell Biology*, vol. 61, pp. 253–257, 1974.

[96] L. E. Barrett, J.-Y. Sul, H. Takano, E. J. V. Bockstaele, and P. G. Haydon, "Region-directed phototransfection reveals the functional significance of a dentrically synthe-sized transcription factor," *Nature Methods*, vol. 3, pp. 455–460, 2006.

[97] S. Kaech and G. Banker, "Culturing hippocampal neurons," *Nature Protocols*, vol. 1, pp. 2406–2415, 2006.

[98] H. Kaji, M. Nishizawa, and T. Matsue, "Localized chemical stimulation to micropat-terned cells using multiple laminar flows," *Lab on a Chip*, vol. 3, pp. 208–211, 2003.

[99] G. M. Walker, H. C. Zeringue, and D. J. Beebe, "Microenvironment design consider-ations for cellular scale studies," *Lab on a Chip*, vol. 4, pp. 91–97, 2004.